PHYSICAL LAYER DESIGN AND IMPLEMENTATION OF DISTRIBUTED ARRAYS IN PACKET NETWORKS

A Dissertation
Presented to
The Academic Faculty

By

Qiongjie Lin

In Partial Fulfillment
of the Requirements for the Degree
Doctor of Philosophy in the
School of Fiction

Georgia Institute of Technology

December 2017

PHYSICAL LAYER DESIGN AND IMPLEMENTATION OF DISTRIBUTED ARRAYS IN PACKET NETWORKS

Approved by:

Dr. Mary Ann Weitnauer, Advisor
School of ECE
Georgia Institute of Technology

Dr. John R. Barry
School of ECE
Georgia Institute of Technology

Dr. Doug Blough
School of ECE
Georgia Institute of Technology

Dr. Raghupathy Sivakumar
School of ECE
Georgia Institute of Technology

Dr. Yang Wang
School of Civil and Environmental Engineering
Georgia Institute of Technology

Date Approved: November 10, 2017

To my parents and husband.

ACKNOWLEDGEMENTS

Pursuing Ph.D at Georgia Tech for the past five years is such a wonderful journey full of great memories, that I will always cherish and be proud of in my life. There are so many people I want to thank, without them I could never make through this process.

Above all, I would like to express my deepest gratitude to my advisor, Prof. Mary Ann Weitnauer, for her constantly inspiration, encouragement and guidance. With her passion, immense knowledge, and insightful coaching, I have truly gained a lot of precious experience and skills that I shall benefit for the rest of my career and life. I am deeply indebted to her not only for the tremendous technical advices during my doctoral study but also her thoughtfulness, trust and unlimited support in spite of all my weaknesses. She is my role model that I will always look up to.

My special thanks go to Prof. John Barry, Prof. Douglas Blough, Prof. Raghupathy Sivakumar and Prof. Yang Wang for serving on my dissertation committee. Their valuable suggestions and comments have greatly improved my research and the quality of this dissertation.

I thank my awesome friends and colleagues at the Smart Antenna Research Lab, Dr. Yongjun Chang, Dr. Haejoon Jung, Dr. Jian Lin, Dr. Alper Akanser, Dr. Abdul Javaid, Dr. Van Nguyen, Feng Wang, Sajith Mohan Chakkedath, Edith Ghunney, Venkatasivaram Bhamidipati, Anurag Sethi, Daniel Schmaiz, for their everlasting friendship and the help along the way. I also thank the visiting scholars, Prof. Syed Ali Hassan, Prof. Hongxian tian, Dr. Wei Feng, Zhenzhe (Stephen) Sun, Jinyao Liang, Jiakang Xu, for enjoying the life together at Atlanta. Further, I thank many other friends I made at ECE, including Dr. Qingsong Wen, Mohammad Mohammadpour Salut, Yubing Jian, Mengyao Ge, Yiming Kong, Qiang Hu, for the valuable discussions and good times I had whe we did the research or course projects together.

Finally, I wish to thank my beloved husband and parents for their perpetual love and

support. I met my husband, Xin, on the last course we took at Georgia Tech. I feel so lucky to find such a good man who respects and tolerates me in all aspects. Lastly, I want to dedicate this work to my dear parents. They have sacrificed many things so that I can pursue my dream. The success in my education and career, that I had, and will have, is impossible without them.

Table of Contents

List of Tables

List of Figures

SUMMARY

In this dissertation, we develop novel physical layer techniques for the purpose of increased range and increased data rates in modern wireless networks. All of these techniques utilize at least one distributed or virtual array, which is a collection of distinct radios or devices that collaborate in the physical layer or waveform domain in terms of synchronization and modulation. In some cases, there is a distributed array at one or both ends of a multi-input-multi-output (MIMO) link, thereby forming a distributed MIMO link. All techniques are demonstrated using software defined radio (SDR). We consider both orthogonal frequency-division multiplexing (OFDM)-based wideband transmission and minimum shift keying (MSK) narrowband modulation. The targeted wireless applications include local area networks, sensor networks, low power wide area (LPWA) networks, and ad-hoc networks.

The main contributions of this dissertation are as follows. Novel synchronization strategies that provide diversity gain and robustness against interference in range extension scenarios have been created for the distributed MIMO system. Additionally, novel methods of time division cooperative transmission (TDCT) with diversity gain and multi-user MIMO with amplify-and-forward (AF) relaying for array gain are implemented and demonstrated on SDRs for the purpose of range extension. Moreover, "capture and successive interference cancellation" (C&S) and "network MIMO" (NMIMO) are combined to create a novel on-demand form of NMIMO, which can lower cost in LPWA applications, and the corresponding functionalities are tested on SDRs. Lastly, a hybrid method of selective application of nonlinear precoding (NLP) on top of interference alignment (IA) beams over multi-user, multi-access point MIMO networks has been proposed for the purpose of more efficient interference cancellation. We modify the conventional MMSE IA algorithm by minimizing the interference among selected paths but ignore the interference among the other paths, leading to faster convergence. Then, we apply the Tomlinson-Harashima

precoding (THP) on top of selected IA beams with the purpose of handling the ignored interference. In addition, we repeat the modified IA with random initializations in order to maximize the sum capacity and reduce the BER performance difference among users. Sum capacity appears to converge with number of repetitions. The Tomlinson-Harashima NLP scheme is implemented on SDR to demonstrate real-time packet decoding performance.

CHAPTER 1
INTRODUCTION

Multi-input multi-output (MIMO) is well known to improve the throughput and reliability of wireless links [1], and has thus become an essential element for wireless communication standards, such as IEEE 802.11(Wi-Fi) [2], Long Term Evolution (4G) [3], and WiMAX [4]. However, the conventional MIMO techniques have scalability challenges as networks become more dense. The proliferation of both devices and access points (APs) leads to a high level of co-channel interference in dense deployments [5, 6].

The densification problem is also present in the low power wide area (LPWA) applications, including product/customer/asset tracking and monitoring of pollution, traffic, parking availability, livestock, wildlife, pest traps, refuse volume, and growing conditions in agriculture, as well as early warning indicators of geological disasters, hazardous chemicals, and flooding [7, 8, 9]. These sensor based wireless applications require a significant high-coverage, low-bandwidth, low-cost per connection, and years-long battery life, but these applications are not supported by the existing energy hungry and expensive wireless networks, such as cellular, WiFi, or Zigbee networks.

We contend that the distributed array is an effective solution to overcome physical limitations while exploiting conventional spatial diversity through cooperative communications. The distributed array is a collection of distinct radios or devices that collaborate in the physical layer or waveform domain in terms of synchronization and modulation. In some cases, there is a distributed array at one or both ends of a MIMO link, thereby forming a distributed MIMO link.

The objective of this dissertation is to develop the physical layer distributed array approaches by taking advantage of the cooperation of communications across multiple devices and the availability of software defined radio (SDR) technologies for both OFDM-

based wideband transmission and minimum shift keying (MSK) low data rate transmission.

1.1 Organization and Main Contributions

In Chapter 2, the origin and history of the problem are presented in great detail. We review the related works in the literature and industry, and make common definitions and assumptions. In addition, the challenges and issues for the existing methods are discussed.

According to the topology of the wireless system we have studied, the proposed techniques are concisely divided into four chapters in this dissertation.

In Chapters 3 and 4, we study the distributed array schemes for the ad-hoc network, where there is no pre-existing infrastructure and all radios are equipped with single antenna. We exploit distributed array and diversity gains for both reliability and data rate to support OFDM based wideband transmission. In Chapter 3, we focus on Time Division Cooperative Transmission (TDCT) to increase the reliability between a source and destination through the help of relay cluster in the middle that cooperates in orthogonal time slots. In Chapter 4, we study a two-hop multi-user multiple-input-multiple-output (MU-MIMO) system with amplify-and-forward (AF) relays. The corresponding contributions are: 1) a novel method of time and frequency synchronization for OFDM-based TDCT that achieves diversity gain for range extension application; 2) a novel packet design for MU-MIMO with AF; and 3) a demonstration of the packet error rate (PER) performance for both TDCT and MU-MIMO and in a realistic indoor environment with a commercial software radio platform, using OFDM.

In Chapter 5, we provide a physical (PHY) layer solution considering the coordination among gateways in the wireless sensor network to support low data rate Internet of Things (IoT) applications. The corresponding contributions are: 1) an on-demand network MIMO scheme to achieve dynamic packet decoding from transmit-only sensors; 2) a data-aided (DA) synchronization algorithm for minimum-shift keying (MSK) transmission which is interference insensitive; 3) an analysis of the practical residual error of interference cancel-

lation (IC) for MSK packets, considering realistic synchronization. The analysis is verified through the measurement on the SDR testbed.

In Chapter 6, we address the application of distributed arrays to boost the capacity for the downlink transmission of multi-user, multi-access point MIMO networks. The corresponding contributions are: 1) a hybrid method combining nonlinear precoding (NLP) and interference alignment (IA), which selectively applies NLP on top of IA beams to achieve lower computation complexity and better BER performance compared with the IA-only scheme. 2) demonstrate the NLP in a realistic indoor environment.

The SDR testbed we use is described in Appendix A.

CHAPTER 2

ORIGIN AND HISTORY OF THE PROBLEM

In this chapter, we review the related works in the literature and industry, and make common definitions and assumptions. In Section 2.1, we summarize the different performance gains of classic arrays. In Section 2.2, popular distributed array (DA) schemes that consider the coordinations among distinct radios for a variety wireless networks are reviewed. According to the objectives of exploiting the distributed spatial gains, we review the existing DA schemes in two categories: DA for reliability and DA for data rate. In addition, the existing works about interference suppression that support co-channel packets transmission to maximize network capacity has been reviewed in Section 2.3. Lastly, in Section 2.4, we overview the state-of-the-art of packet synchronization algorithms for OFDM based wideband transmission and MSK based narrowband transmission. Meanwhile, the challenges of the synchronization problem for distributed arrays are stated.

2.1 Classic Arrays

The classic array in which multiple antennas are co-located in a single device, has been widely adopted in a variety of wireless communication systems, such as IEEE 802.11(Wi-Fi) [2], Long Term Evolution (4G) [3], and WiMAX [4], to improve the spectral efficiency and the reliability.

(a) Transmit/Receive array (b) Point-to-point MIMO

Figure 2.1: Different categories of Classic arrays.

In terms of the physical location of the array, classic arrays can be broadly classified into three categories as illustrated in Fig.2.1. When only the transmitter is equipped with multiple antennas, it is also known as multiple input and single output (MISO). For this category, with the channel state information available at TX side (CSIT); the antenna array can be used to perform coherent beamforming; otherwise a spatial time block coding (STBC) scheme can be used to achieve transmit diversity [10]. Similarly, when the antenna array is located only at the RX side, the link is called single input and multiple output (SIMO). Algorithms, such as maximal ratio combining (MRC) or minimum mean squared error (MMSE), are widely considered to achieve the receive diversity. Lastly, when both TX and RX are equipped with multiple antennas, it is the well-known point-to-point MIMO, which exploits both spatial diversity and spatial multiplexing gains through the MIMO link.

2.1.1 Spatial gains

The performance improvement resulting from classic arrays generally falls into three categories: spatial multiplexing (SM) gain, diversity gain, and array gain [11].

SM gain. SM gain is the *factor* increase in achievable data rate, relative to a link with single-antenna radios, equal to min(N, M), where N and M are the numbers of transmit and receive antennas, respectively, in a MIMO link [12]. Unlike spreading or higher-order modulations, SM gain comes with no net increase in power or bandwidth at the transmitters. The main challenge to achieving spatial multiplexing gain is data separation, that is extracting the parallel data streams which occupy the same time and frequency resources. Data separation can be classified based on where the processing is done. When it is done on the receiver side, we refer to it as interference cancellation or suppression. A receiver spatial filter, commonly referred to as a beamformer, computed from channel state information (CSI). The minimum mean squared error (MMSE) beamformer [13] or the zero-forcing (ZF) beamformer [14], is applied on the received signal vector to cancel out the co-channel interference. It is well known that zero-forcing beamforming enhances the noise power and

hence has poor power efficiency. This disadvantage can be overcome by some nonlinear schemes, such as spatial decision-feedback equalization (DFE) [15]. However, DFE suffers from error propagation.

Instead of separating the components of the transmitted vector at the receiver side, the data separation also can be done at the transmitter side by the means of precoding, given the channel state information (CSI) is available [16, 17] through feedback. Unfortunately, linear precoding tends to require a high peak-to-average ratio (PAR) and the saturation limits of practical power amplifiers require a backoff. This backoff is equal to a power loss which is the loss in the average transmit power with respect to (w.r.t) the case without precoding; Non-linear MIMO precoding can cause less power loss [18, 19] at the transmitter side. The most popular one is *Tomlinson-Harashima Precoding* (THP) [20]. THP eliminates the interference by sequentially pre-subtracting the interfering symbols at the transmitter. It is well known that THP incurs a small SNR penalty relative to a SISO link. This happens because the modulo operation in the transmitter expands the constellation slightly and because the receive constellation before the modulo operation has many more points than the original transmit constellation (before modulo), thereby creating more opportunities for symbol detection error. Several modifications to THP have been proposed in the literature to address the power loss issue [21, 22, 23].

Diversity gain. Diversity gain denotes the improvement in link reliability by receiving replicas of the source signal through multiple independent single-input single-output (SISO) fading channels. With an increasing number of independently fading copies, the probability that at least one of the signals is not experiencing a deep fade increases, thereby improving the quality of reception. Packets with diversity gain may not need forward error correction (FEC). With at least two antennas, a reduction of 10 dB or more in the extra transmit power, or fade margin, is possible compared with single-antenna receiver.

Among all transmit diversity gain schemes, the most prominent are space-time codes (STC) [24, 25], in which the individual signal streams from each transmit antenna are

jointly encoded.

Array gain. Array gain is the improvement in link quality measured by the increase in average signal-to-noise ratio (SNR) for a single source stream. Array gain results when the desired signal parts in each receive array element are combined coherently but the noise and interference are not. Array gain can be had in non-fading or fading environments, where as diversity gain is available only in fading environments. The receive array with M antennas can provide an array gain of $10logM$.

2.2 Distributed Arrays (DAs)

When a collection of distinct radios or devices collaborate in the physical layer or waveform domain in terms of synchronization and modulation, we classify it as a distributed array (DA) or virtual array approach. DAs can provide similar gains to classic arrays, at the cost of network overhead to organize and provide various levels of synchronization. However, DAs provide network flexibility and lower per device hardware cost. An example of flexibility is radios can be recruited as needed to achieve a network goal, such as balancing energy use, overcoming partitions, or extend transmission range [26]. We review the existing DA schemes in two categories: DA for reliability and DA for data rate.

2.2.1 DA for reliability

As the simplest DA approach, **Cooperative transmission (CT)** has been extensively studied in the past decades to compensate limited resources in ad-hoc networks [27]. For CT, the single-antenna radios assist each other to relay a single message, thereby forming a distributed multi-input and single-output (DMISO) link or a virtual array [28]. The classic 3-node CT is illustrated in Fig.2.2, where the destination gets a signal-to-noise ratio (SNR) advantage provided through the DMISO. The diversity gain of the virtual transmit array can be used to reduce the TX power, extend the range of the transmissions and overcome network partitions [29], or to reduce the bit error rate (BER) of the received signal.

Meanwhile, the SM strategies also can be extended into distributed manner with CT [30].

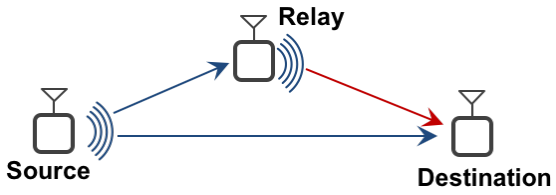

Figure 2.2: Classic 3-node cooperative transmission.

There are three types of *relaying strategies* [31]. The first is *amplify-and-forward (AF)* relaying, where the relay node simply amplifies the received signal from the source and forwards it to the destination. The second is *decode-and-forward (DF)* relaying, also known as regenerative relaying, where the relay node decodes (perhaps incorrectly) and re-encodes each symbol before retransmission. The final type is *compress-and-forward (CF)* relaying, which allows the relay node to compress the received signal from the source and digitally forward it to the destination without decoding the signal.

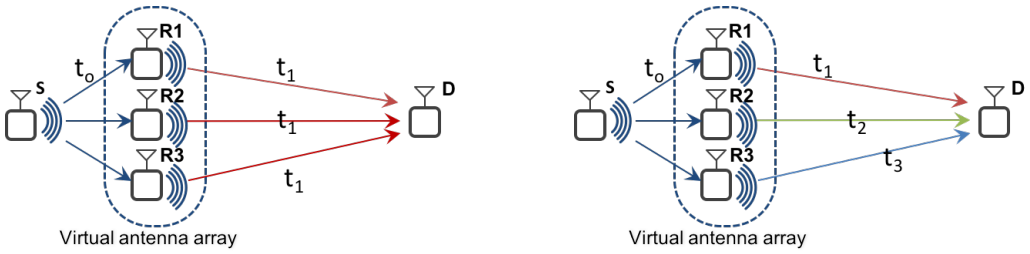

(a) CCT model. (b) TDCT model.

Figure 2.3: Illustration of CT models.

CT can be performed simultaneously or in different time slots as illustrated in Fig.2.3, referred to as concurrent cooperative transmission (CCT) and time division cooperative transmission (TDCT), respectively. One focus of this dissertation is TDCT with the objective of extending transmission range. In the context of range-extension, TDCT has some advantages over CCT. Neither transmitter-side channel state information nor phase coherency across cooperating transmitters is required by TDCT; conversely, they are re-

quired in the coherent form of CCT, also known as coherent beamforming [30]. All the cooperators must be recruited prior to a CCT transmission, whereas for TDCT, they can be recruited incrementally, as needed [32]. To achieve range extension, transmitters should use the same transmit power as in the conventional single-input-and-single-output (SISO) case. This leads to another advantage of TDCT: its interference range is the same as SISO interference, whereas CCT interference range is larger due to the high power resulting from concurrent transmission.

2.2.2 DA for date rate

Multi-user MIMO (MU-MIMO). MU-MIMO is a popular and spectrally efficient approach in current cellular standards (e.g., LTE and 802.16m), wherein a multi-antenna base station (BS) serves several users simultaneously in the same wireless channel [33]. As shown in Fig.2.4, a base station (BST) with large array size serves the concurrent uplink transmission among multiple end-users, which are each equipped with one or more antennas. Considering limited radio spectrum resources and the proliferation of both users and access points, significant efforts have been made to boost the system capacity through MU-MIMO in wireless networks, especially for cellular networks [6].

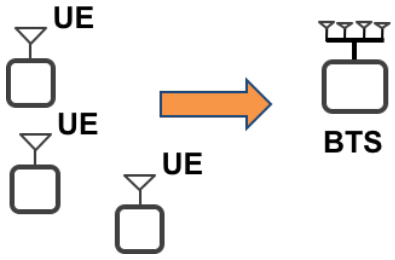

Figure 2.4: Concept of multi-user MIMO.

Coordinated Multi-Point (CoMP). CoMP is a DA type facility being developed for LTE Advanced [34]. As illustrated in Fig.2.5, multiple evolved NodeBs (eNB) dynamically coordinate through the backhual connection to provide joint scheduling and transmissions as well as providing joint processing of the received signals. In this way, a UE at the edge

of a cell is served by two or more eNBs to improve signal reception and transmission and increase throughput. By tightly coordinating the transmission and reception of signals, CoMP transcends the limits on spectral efficiency due to intercell interference.

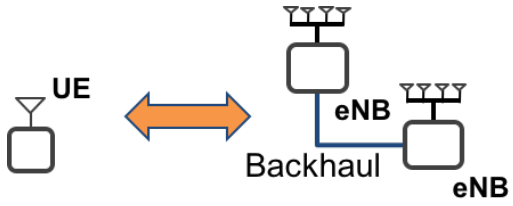

Figure 2.5: Concept of LTE Advanced CoMP.

C-RAN. C-RAN stands for Centralized, Collaborative, Cloud and Clean Radio Access Network, is an architecture for cellular networks, proposed by China Mobile in 2009 to save both capital and operating costs [35]. In C-RAN, a large array of remote radio heads (RRHs) are geographically distributed as shown in Fig.2.6. The antennas are connected to a data center or pool of baseband processing units (BBUs) by "fronthaul" links. The date transmitted through the "fronthaul" links are digitized soft samples of the received waveforms without processing to decode the source bits. In contrast, "backhaul" usually refers to connections between conventional base stations and the central office, which carry no soft samples of signals.

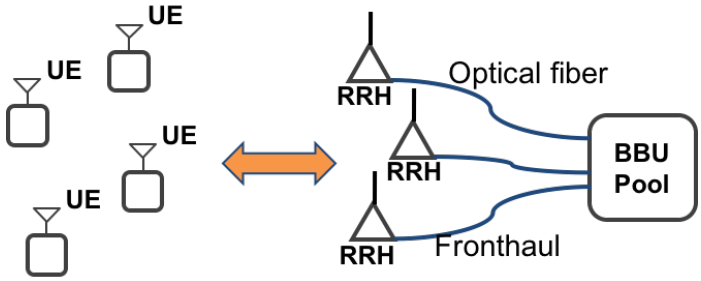

Figure 2.6: Concept of C-RAN.

In a C-RAN, the baseband unit (BBU), which performs the physical layer encoding and decoding and is traditionally housed at the foot of the base station (BS) tower, is moved to a centralized pool or data center, where the baseband processing is done by a virtual BS

running on general purpose platform servers [36]. The BSs are replaced by RRHs, which digitize the uplink signal from the antenna without decoding the signal, and then transmit the bits through optical fiber to the data center; the downlink is the reverse process. Because only the radio front ends are hardware defined, any generation of mobile communications (3G, 4G, etc.) can in theory be implementd in C-RAN.

Network MIMO is a form of MU-MIMO that uses the RRHs as elements in a distributed array, and which coordinates and synchronizes their co-channel receptions and transmissions to increase network throughput. Fronthaul capacity, delay, and jitters have been identified as the major issues of network MIMO [37]. Because the signals received on different antennas can be correlated, joint source coding and decoding techniques, such as the robust distributed compression schemes [38], are effective at reducing fronthaul load. The more recent works emphasize compression of RRH signals before they are modulated onto the fronthaul link [39, 40].

In Chapter V, we propose a novel On-demand form of network MIMO that makes network MIMO affordable for wireless sensor networks and consumer-grade Internet connections.

2.3 Interference Suppression Schemes

2.3.1 Interference cancellation (IC)

Interference cancellation (IC) dates back to the 1990s [41], [42], [43]. IC is attractive because it allows multiple co-channel packets occurring at the same time to be decoded by a single-antenna receiver, resulting in significantly improved reliability and throughput.

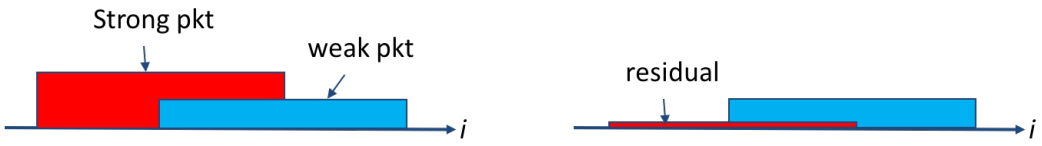

(a) Before IC (b) After IC of strong packet

Figure 2.7: Concept of IC for two overlapped packets.

As shown in Fig.2.7, the effects of a decoded strong packet are subtracted from stored samples of the received signal, thereby making possible the capture of weaker packets. IC has been shown to improve bandwidth utilization in cellular networks [44], which have centralized control and synchronized clocks among wireless devices, and where the towers determine the best transmit power, coding rate and/or spreading codes to enable the disambiguation of different up-link transmissions. However, because of imperfect synchronization and channel estimation, the substraction leaves a residual error, which causes interference on the weaker packets. In the networking literature, some recent works ignore this interference [45, 46] or they model its power very simply as a fixed percentage of the power of the packet being canceled [47, 48]. We refer to the latter case as the "conventional model". However, through theory and experiment, we find that other parameters are very important, particularly the signal-to-interference-plus-noise ratio (SINR) on the preamble of the strong packet. These observations have led to one major contribution of this dissertation: a new physical layer statistical model for IC residual error in constant envelope modulation packet networks.

2.3.2 Interference alignment (IA)

IA is widely studied to boost the system capacity by effectively mitigating interferences among users in the multiuser MIMO interfering broadcast channel (IBC) [49].

The key idea of interference alignment is applying the optimal transmit and receiver spatial filters, i.e., beamforming vectors or linear precoders, so as to align all the undesired

signals at each receiver in the same subspace of suitable dimension, as illustrated in Fig.2.8. Alignment allows each receiver to suppress more interfering streams than it could otherwise cancel. In other words, aligning the streams at the transmitter allows each receiver to cancel more streams than the number of "spare antennas" at its disposal (number of antennas minus the number of desire streams).

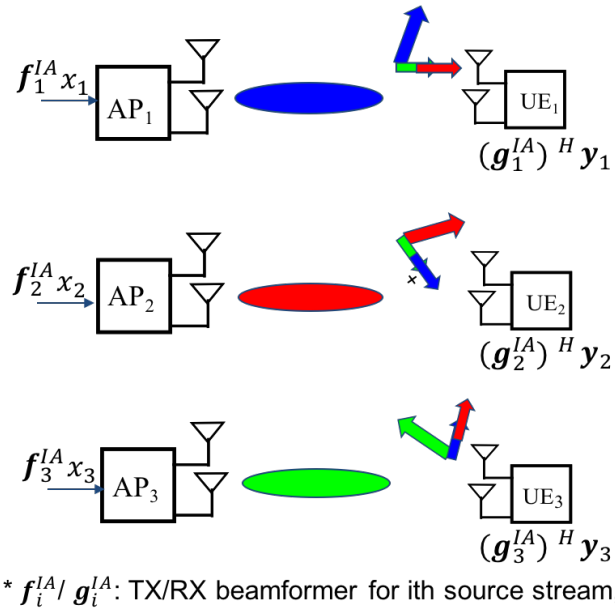

Figure 2.8: Concept of interference alignment (IA).

However, most existing IA solutions are iterative, alternating between calculating the optimal transmit beamformers assuming the updated receive beamformers, and calculating the optimal receive beamformers assuming the updated transmit beamformers [50, 51, 52]. Unfortunately, the iterations cause computational complexity. From an optimization perspective, determining the optimal transmitter/receiver filters that maximize the sum capacity, which depends on the achievable rate over all users, is non-convex and NP-hard even in the single-antenna case [53]. Most existing works focus on finding a high quality suboptimal solution efficiently, while an optimal solution for MIMO IBC at finite SNR remains elusive.

In Chapter VI, we propose a hybrid precoding scheme, which combines IA and THP to

provide improved convergence speed and interference suppression.

2.4 Packet Synchronization

Because of random clock drift and hardware difference of local oscillators among wireless devices, the physical layer packet synchronization at a receiver includes detecting the coming packets and estimating the synchronization parameters, which includes timing and carrier frequency offsets.

Compared with the classic arrays, the synchronization problem is much more challenging in DAs as each array element no longer has access to the same local oscillator and clock. Therefore, network overhead is required to achieve useful synchronization between the distributed array elements.

2.4.1 Synchronization of OFDM based wideband transmission

Orthogonal Frequency Division Multiplexing (OFDM) techniques have been employed intensively for wideband transmission because of their robustness and high spectral efficiency in the frequency selective fading channel. Synchronization is a big issue for any OFDM based wide-band system for it is widely known that symbol timing offsets larger than the cyclic prefix (CP) will introduce inter-symbol-interference (ISI), and carrier frequency offsets (CFOs) will introduce inter-carrier-interference (ICI).

The conventional SISO OFDM synchronization schemes are preamble-based [54], [55], [56], [57]. The method proposed by Schmidl and Cox [54] is the most popular preamble-based scheme.The timing and fractional CFO estimations are done based on the autocorrelation between the two identical halves of the first OFDM symbol in the time domain, while the integer CFO is computed in frequency domain based on the correlation of the second OFDM symbol. However, because of the CP, the timing metric has a plateau which makes the timing synchronization fallible. To eliminate the plateau, Park et al. [55] designed a new repeated-conjugated-symmetric sequence, which makes the timing metric have a sharp

peak. However, because of the special structure of the preamble sequence, the timing metric has side lobes which can still disturb the timing synchronization. In addition, recent works propose to use more complicated sequences, such as CAZAC (Constant Amplitude Zero Auto Correlation) sequence, to perform more accurate offset estimations [56, 58, 57].

The synchronization issue becomes more demanding for CT, as some degree of pre-synchronization, which is synchronization in a transmitter, is neccessary [31]. In pre-synchronization, the transmissions from each cooperator are aligned in time and frequency within a required tolerance at a receiver. Several studies on OFDM-based receiver synchronization for concurrent CT have been reported. In [59, 60], multiple offset estimates are based on the combined preamble, which is problematic in a time division cooperative transmission (TDCT) system, because the timing for each operating link is not known a priori. In Chapter III, we propose a novel method of time and frequency synchronization for OFDM-based TDCT that achieves diversity gain for range extension applications.

2.4.2 Synchronization of MSK based narrow-band transmission

In addition to high spectral efficiency, energy efficiency or equivalently battery duration is another important requirement of most wireless communication systems. For instance, the lower power wide area (LPWA) application, energy efficiency is more crucial to achieve high-coverage, low-cost per connection, and years-long battery life [61, 62]. Constant envelope modulations (CEMs), such as FSK, GFSK, MSK, GMSK, are widely used in low power RF transceivers [63, 64, 65] to enhance and improve the energy efficiency of wireless communication networks from the perspective of signal design. These modulations allow the power amplifiers (PA) in the transmitter to operate at or close to the saturation level to maximize energy efficiency. On the other hand, the more advanced modulations, such as QAM, contain amplitude modulation (AM) components, which require from 3 to 6 dB of back off (from saturation) in the power amplifier to avoid signal distortion [66].

In this dissertation, we consider minimum-shift keying (MSK)-type modulation for

narrow-band transmission for low-power, long-range radio applications. MSK can be viewed as continuous-phase frequency-shift keying (CPFSK) with a frequency deviation of $\frac{1}{4T_s}$, where T_s is the a symbol period. and a modulation index of 0.5 [66]. MSK is attractive because the phase continuity yields higher spectral efficiency than non-phase continuous BFSK, and the constant envelope yields excellent power efficiency. The primary drawback of MSK is the high implementation complexity for an optimal receiver by the fact that the initial phase of each symbol is determined by the accumulated total phase of all previous transmitted symbols. However, the maximal likelihood sequence estimator based on the Viterbi algorithm is affordable on the uplink [67].

The majority of works on synchronization of continous phase modulation (CPM) transmissions use non-data-aided algorithms based on feed-forward algorithms [68]. In addition to their limited application, these methods do not perform as well as data-aided algorithms, which use a preamble of known sequence appended to the beginning of each packet [69]. The data-aided joint phase and timing estimation algorithm proposed in [70] is based on the minimum mean-square error (MMSE) and implemented as a Kalman filter. However, this method is implemented in a closed-loop manner that requires multiple initialization steps. Hosseini and Perrins [71] propose a complete data-aid type scheme including all synchronization parameters estimation. However, it relies on an optimized preamble with a specific phase trajectory, and hence tends to fail when there is distortion on the preamble caused by interference. In Chapter V, we propose a data-aided synchronization method suitable for LPWA applications and which is robust to interference.

CHAPTER 3

TIME DIVISION COOPERATIVE TRANSMISSION (TDCT) WITH SYNCHRONIZATION DIVERSITY GAIN

3.1 Overview

An energy efficient synchronization method is presented for an OFDM-based Time Division Cooperative Transmission (TDCT) system for the purpose of range extension. The proposed algorithm operates on a novel preamble consisting of two OFDM symbols. In TDCT, copies of the packet are transmitted through different time slots. Exploiting dependence between the synchronization parameters of the different TDCT copies, the approach achieves diversity gain in all estimated synchronization parameters. Since the design and algorithm pertain only to the preamble, the method can be applied to decode-and-forward as well as amplify-and-forward TDCT schemes. This algorithm also offers a significant performance improvement to the single-input-and-single-out (SISO) communication system. Through computer simulation, we show that our novel TDCT approach achieves synchronization in the context of range extension, avoiding the need for more preamble energy.

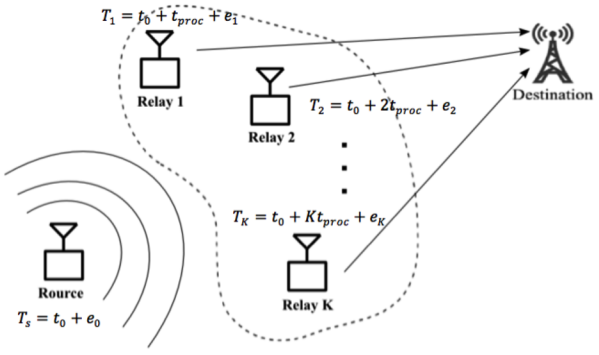

Figure 3.1: Illustration of two-hop TDCT system.

As illustrated in Fig.3.1, we consider a half-duplex time-division cooperative commu-

nication system with one source node, $\mathbf{S}$, a relay cluster of K cooperating relay nodes $\{R_1, R_2, ..., R_K\}$, and a destination node, $\mathbf{D}$. We assume direct communication between the source and the destination is not available. There are two phases of transmission to achieve the communication between source and destination. In the first phase, the source, $\mathbf{S}$, broadcasts the message to potential relay nodes. Some or all the relay nodes that correctly decode the packet from the source node will participate in the second phase, keeping the same synchronization offsets for transmission that they learned in reception. We note that preservation of the frequency offset for transmission is not done in conventional packet radio but is a key to range extension.

Pre-synchronization. In this work, we focus on the synchronization at the destination receiver during the second phase, assuming pre-synchronization was done within the relay cluster before retransmission.With timing pre-synchronization [72], the kth relay is scheduled to transmit in the kth time slot as $T_k = T_0 + kt_{proc} + e_k$, where T_0 is the transmitting time of the source node, and also the time that the source packet arrives at the antennas of the relay nodes. t_{proc} is a period of time designed so that the transmit first-in-first-out buffer will be full when the transmission starts; in other words, t_{proc} is long enough to ensure the processing and on-band signal transfers are complete by the time the node is supposed to transmit. The timing pre-sychronization error, e_k, is modeled as a zero mean Gaussian random variable with variance δ_e^2, denoted as $e_k \sim \mathcal{N}(0, \delta_e^2)$.

For pre-synchronization of frequency [73], each relay node estimates the CFO relative to the source node, and compensates it to any data it plans to transmit during the second phase. Therefore, after pre-synchronization, the CFO between kth relay node, R_k, and destination, $\mathbf{D}$, f_{kd}, is modeled as $f_{kd} = f_{sd} + e_\epsilon$, where f_{sd} represents the CFO between source and destination and $e_\epsilon \sim \mathcal{N}(0, \delta_\epsilon^2)$ is the frequency pre-synchronization error.

Consider a normalized time offset ε_k with respect to sampling period T_s and the normalized frequency offset ω_k with respect to subcarrier spacing, f_s. Then, $\omega_k = \frac{f_{kd}}{f_s} = \mu_k + \nu_k$, where μ_k and ν_k are the fractional CFO and integer CFO, respectively, of the kth relay node

relative to the destination. Therefore, the received signal at the destination during the kth time slot can be expressed as $r^k(n) = e^{j2\pi\omega_k \frac{n}{N}} \sum_{g=0}^{G} h^k(g)s^k(n-g-\varepsilon_k) + z^k(n)$, where $s^k(n)$ is the source signal; $\mathbf{h}^k = [h^k(0), \ldots, h^k(G-1)]^T$ and $z^k(n)$ are channel impulse responses with G as the number of resolvable paths and additional white Gaussian noise (AWGN) with variance σ_N^2, respectively.

3.2 Synchronization Algorithm

The proposed preamble structure in both time and frequency domains is illustrated in Fig.3.2. The two OFDM symbols are constructed based on a CAZAC sequence $\{C(i)\}$ with length L. According to [74], the CAZAC sequence can be chosen as: $C(i) = e^{j\pi pi^2/L}$, where p is the positive integer and relative-prime to L; we choose p=L-1. The good properties of CAZAC sequences are $\|C(i)\| = 1$ and :

$$\sum_{i=0}^{L-1} C(i)C^*(i+k) = L, \ k = 0 \tag{3.1}$$

$$\sum_{i=0}^{L-1} C(i)C^*(i+k) = 0, \ o.w. \tag{3.2}$$

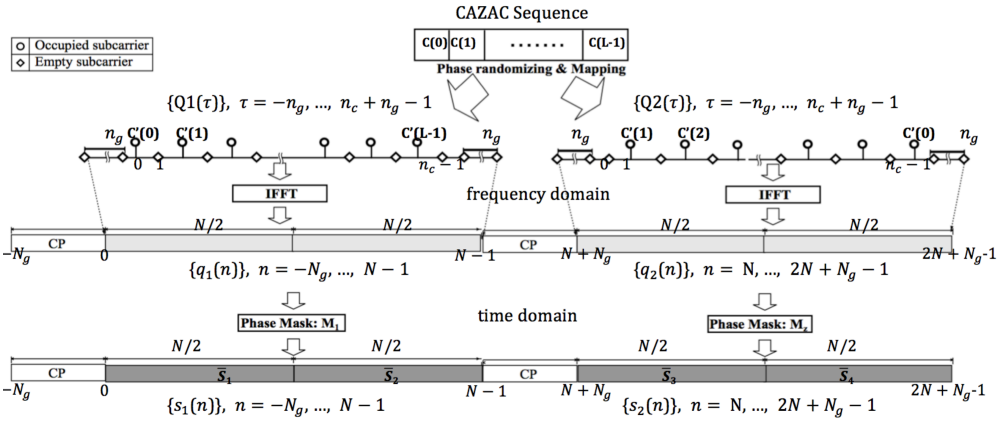

Figure 3.2: Illustration of proposed preamble structure for TDCT.

3.2.1 Preamble design

To construct the preamble in the frequency domain, we first randomize the phase of the CAZAC sequence to get the intermediate sequence $C'(i) = C(i)e^{j2\pi r_i}, i = 0, \ldots, L-1$, where $r_i \sim U[0,1]$ is uniformly distributed over the interval [0,1]. The purpose of randomizing the phase is to enlarge the difference of the target metric for integer CFO estimation between correct estimation and false estimation, which will be discussed in detail in the section below.

For the sake of convenience, we assume that the subcarrier index starts at $-n_g$, where n_g is the length of a guard interval of null tones reserved on both sides of an OFDM symbol in case of preamble aliasing due to integer CFO [54]. The n_c subcarriers in the middle part are used for preamble design. Therefore, the subcarrier index in frequency domain is then indicated by $\tau \in \{-n_g, \ldots, n_c + n_g - 1\}$, and the total length of the OFDM symbol in the frequency domain is $n_c + 2n_g$, as shown in Fig.3.2. To construct the preamble in the frequency domain, the sequence $\{C'(i)\}$ is mapped to all even subcarriers on the first OFDM symbol, and is mapped to all odd subcarriers on the second OFDM symbol after a left circular shift of D steps ($1 \leq D \leq L-1$ $D = 1$ in Fig.3.2). Therefore, the preamble in the frequency domain, consisting of two OFDM symbols, $Q_1(\tau)$ $Q_2(\tau)$ for $\tau = 0, \ldots, n_c - 1$, are

$$
\begin{aligned}
Q_1(\tau) &= \begin{cases} C'(\frac{\tau}{2}), & modulo(\tau, 2) = 0 \\ 0, & modulo(\tau, 2) = 1 \end{cases}, \\
Q_2(\tau) &= \begin{cases} C'(\frac{\tau-1}{2} + D), & modulo(\tau, 2) = 1 \\ 0, & modulo(\tau, 2) = 0 \end{cases}.
\end{aligned}
\tag{3.3}
$$

The two OFDM symbols of the preamble in the frequency domain are designed with the relationship as $Q_1(\tau)$ is the result of right circular shift of $Q_2(\tau)$ by 2D-1 steps, which provides the ideal structure in the time domain for timing synchronization, as we will see in a later section.

The preamble in the time domain is constructed in two steps. First, the constructed preamble in the frequency domain is converted into the time domain signal through the inverse discrete Fourier transform (IDFT) and a cyclic prefix with length N_g is attached in front to avoid ISI. For the sake of convenience, we assume that the time domain preamble starts at discrete index zero and the attached cyclic prefix has negative time indices as shown in Fig.3.2. So the length of the OFDM symbol in the time domain is $N + N_g$. N is the IDFT/DFT length, which equals $n_c + 2n_g$. The two OFDM preamble symbols are denoted as $\{q_1(n)\},\ n = -N_g, \ldots, N-1$, and $\{q_2(n)\}, n = N, \ldots, 2N + N_g - 1$, respectively.

Because of the special structure of the preamble in the frequency domain, $\{q_1(n)\}, \{q_2(n)\}$ have a repetition property,

$$\begin{cases} q_1(n) = q_1(n + \frac{N}{2}), & n = 0, \ldots, \frac{N}{2} - 1, \\ q_2(n) = -q_2(n + \frac{N}{2}), & n = N + N_g, \ldots, N + N_g + \frac{N}{2} - 1. \end{cases} \tag{3.4}$$

In addition, the two preamble sequences also satisfy $q_1(n) = q_2(n)e^{-j2\pi(n-1)\frac{2D-1}{N}}$.

In the second stage, to avoid the timing ambiguity caused by the cyclic prefix, we use two phase masks $M_j, j = 1, 2$, which are constructed as $M_j(n) = e^{j2\pi m_n^j},\ for\ n = 0, \ldots, N-1$, where, $m_n^j \sim U[0, 1]$ are uniformly distributed random variables over the interval $[0, 1]$. The phase masks M_j are constructed with a similar repetition property as: $M_j(n) = M_j(n + \frac{N}{2}), for\ n = 0, \ldots, \frac{N}{2} - 1, j = 1, 2$.

We then modulate the two preamble sequences $\{q_1(n)\}$ and $\{q_2(n)\}$ with the two phase masks M_1 and M_2, respectively. The two time domain preambles become

$$\begin{cases} s_1(n) = q_1(n)M_1(n), n = 0, \ldots, N-1 \\ s_1(n - N_g) = q_1(n - N_g), n = 0, \ldots, N_g - 1 \\ s_2(n + N + N_g) = q_2(n + N + N_g)M_2(n), n = 0, \ldots, N-1 \\ s_2(n + N) = q_2(n + N), n = 0, \ldots, N_g - 1. \end{cases} \tag{3.5}$$

As we can see from Eq.(3.5), the phase mask operates on only N out of $N+N_g$ samples, to avoid a plateau in the timing metric [54], [55].

Because of the repetition property of the phase masks, the time domain preamble still keeps the same repetition property shown in Eq.(3.4). For TDCT relaying, all relay nodes use the same preamble structure; the preamble for kth relay node is denoted as:

$$s^k(n) = \{s_1(n), s_2(n)\}. \tag{3.6}$$

3.2.2 Symbol timing estimation

The goal of symbol timing estimation is to estimate the normalized time offset ε_k for each relay and destination link k, so that the start of the packet (SOP) of each relay is identified.

The symbol timing estimation in the proposed method is obtained through two steps: (1)coarse timing estimation with the goal of detecting the packet and estimating the coarse SOP, and (2)fine timing estimation with the goal of estimating the SOP with high accuracy.

Coarse timing estimation. Because of the repetition property of the preamble, we keep processing the received signal, $r^k(n)$, as four segments, each with length $\frac{N}{2}$. The four segments for the kth relay link received at the receiver are defined as: $\bar{s}_1^k(i) = r^k(n+i), \bar{s}_2^k(i) = r^k(\frac{N}{2}+n+i), \bar{s}_3^k(i) = r^k(N+N_g+n+i), \bar{s}_4^k(i) = r^k(N+N_g+\frac{N}{2}+n+i), for\ i = 0, \ldots, N/2$. We compute six correlation metrics among the four segments as

$$\begin{aligned} &P_j^k(n) =< (\hat{\mathbf{s}}_x^k(n))^\dagger, \hat{\mathbf{s}}_y^k(n) >, j = 1, .., 6, \\ &with\ x \in \{1,2,3,4\}, y \in \{2,3,4\}, \end{aligned} \tag{3.7}$$

where, $x = 1, y = 2, 3, 4; x = 2, y = 3, 4; x = 3, y = 4$ corresponds to j=1,..,6, respectively. $\hat{\mathbf{s}}_1^k(n) =< \bar{\mathbf{M}}_1^\dagger, \bar{\mathbf{s}}_1^k(n) >, \hat{\mathbf{s}}_2^k(n) =< \bar{\mathbf{M}}_1^\dagger, \bar{\mathbf{s}}_2^k(n) >, \hat{\mathbf{s}}_3^k(n) =< \bar{\mathbf{M}}_2^\dagger, \bar{\mathbf{s}}_3^k(n) >, \hat{\mathbf{s}}_4^k(n) = - < \bar{\mathbf{M}}_2^\dagger, \bar{\mathbf{s}}_4^k(n) >$, are the received four preamble segments with phase masks removed, as $\bar{\mathbf{M}}_1 = [M_1(0), \ldots, M_1(\frac{N}{2}-1)]$ is the first half of the phase mask M_1, and $\bar{\mathbf{M}}_2 = [M_2(0)e^{j2\pi\frac{2D-1}{N}0}, \ldots, M_2(\frac{N}{2}-1)e^{j2\pi\frac{2D-1}{N}(\frac{N}{2}-1)}]$, is the first half of the phase mask

M_2 with phase rotation of $e^{j2\pi\frac{2D-1}{N}i}$ on the ith element. The purpose of the rotation on the phase in Segments 3 and 4 is to cancel the difference relative to Segments 1 and 2, so that all the six correlation metrics in Eq.(3.7) reach the maximal value at the SOP point.

For simplicity in description of the scheme, we derive the correlation metrics assuming only one resolvable path for each relay link (our simulation uses multiple paths). The jth correlation metric for the kth relay link at the SOP can be expressed as

$$\begin{aligned} P_j^k(\varepsilon_k) = \sum_{i=0}^{N/2-1} \Big\{ & \left|h^k\right|^2 e^{j2\pi\omega_k\frac{N}{2}} \left|s^k(i)\right|^2 \\ & + (z^k(\varepsilon_k+i))^\dagger (h^k e^{j2\pi\omega_k\frac{i+N/2}{N}} s^k(i+\tfrac{N}{2})) \\ & + (h^k e^{j2\pi\omega_k\frac{i}{N}} s^k(i))^\dagger (z^k(\varepsilon_k+i+\tfrac{N}{2})) \\ & + (z^k(\varepsilon_k+i))^\dagger z(\varepsilon_k+i+\tfrac{N}{2}) \Big\}, for\ j=1,\ldots,6. \end{aligned} \tag{3.8}$$

Except for the first term, all the other terms in Eq.(3.8) have expectation of zero, therefore, the expectation of the correlation metric conditioned on h^k is

$$\begin{aligned} E\{P_j^k(\varepsilon_k)\} &= \left|h^k\right|^2 e^{j\pi\omega_k\frac{N}{2}} \sum_{i=0}^{N/2-1} \left\{ \left|s^k(i)\right|^2 \right\} \\ &= \left|h^k\right|^2 e^{j\pi\omega_k\frac{N}{2}} E_0, \end{aligned} \tag{3.9}$$

where $E_0 = \sum_{i=0}^{N/2-1} \left\{ \left|s^k(i)\right|^2 \right\}$ is half the energy of one preamble sequence, which, as shown in Eq.(3.6), is the same for all links.

To normalize the correlation metric, we define a normalizing factor as

$$\hat{V}^k(n) = \frac{1}{4} \sum_{i=0}^{N/2-1} \left(|r^k(n)|^2 + |r^k(n+\frac{N}{2})|^2 + |r^k(n+N+N_g)|^2 + |r^k(n+N+N_g+\frac{N}{2})|^2 \right). \tag{3.10}$$

Similar to [54], we can compute six normalized timing metrics as $M_j^k(n) = \frac{P_j^k(n)}{\hat{R}^k(n)}, for\ j = 1, ..., 6$.

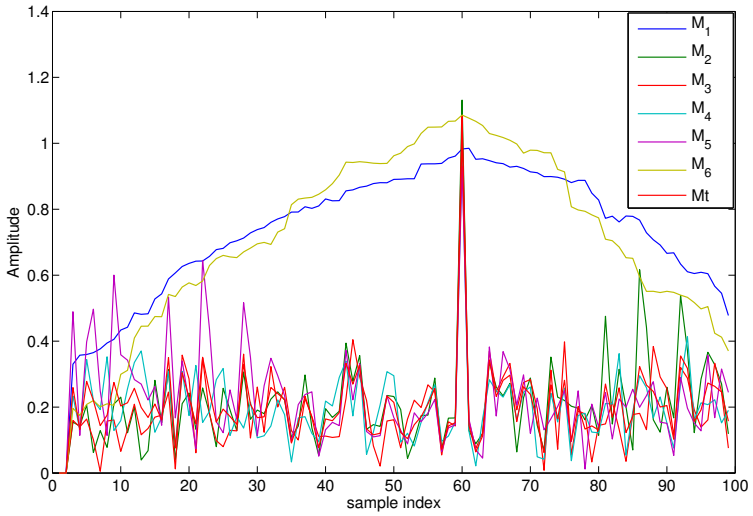

Figure 3.3: The six coarse timing metric in Eq.(3.11) under multipath fading channel with SNR=10dB and SOP=60.

It is obvious that the timing metric $M_j^k \in (0, 1]$ and achieves the maximum value 1 for the ideal channel at the SOP. As shown in Fig.3.3, because of the phase masks and symmetric property of the proposed preamble structure, all the timing metrics have peak value at the SOP point except for M_1^k and M_6^k, which have plateaus because of the phase masks being removed automatically during the CP period.

We then propose the coarse timing metric for kth relay link based on four timing metrics as

$$C^k(n) = \frac{\hat{P}^k(n)}{V^k(n)}, \tag{3.11}$$

where, $\hat{P}^k(n) = \frac{1}{4}\sum_{j=2}^{5} \left|P_j^k(n)\right|$. As shown in Fig.3.3, the coarse timing metric has a sharp peak value at SOP.

Once the coarse timing metric $C^k(n)$ exceeds a pre-defined threshold $T_c \in (0, 1)$, the coarse timing for kth relay link during the kth time slot can be estimated at the destination by searching $\tilde{\varepsilon}_k = \arg\max_{n\in\mathcal{N}} \{C^k(n)\}$, where $\mathcal{N}$ is a set of adjacent sample points that exceed the threshold T_c. T_c is a system parameter which determines the packet detection

rate (PDR). The higher T_c is, the lower PDR is achieved.

For TDCT relaying, as long as the destination detects at least one of the relayed packets, we say the destination receiver detects the packet from the source successfully. We define the packet detection rule for TDCT as

$$\begin{cases} C^{k_{opt}}(\tilde{\varepsilon}_{k_{opt}}) > T_c, & Packet\ detected \\ o.w. & Packet\ missed, \end{cases} \tag{3.12}$$

where, $k_{opt} = \arg\max_k \{\hat{P}^k(\tilde{\varepsilon}_k)\}$.

If the k_{opt} packet is detected, and the receiver can decode the k_{opt} from the header, then assuming the relays transmit consecutively (this is the scheduling aspect); the receiver can find the other copies at time indexes $\bar{\varepsilon}_k = \tilde{\varepsilon}_{k_{opt}} + (k - k_{opt})t_{proc}$, for $k = 1, \ldots, K$. Since both the numerator and denominator of the metric in Eq.(3.11) are weighted by $|h^k|^2$, there is a benefit from diversity, because noise will have the lowest degradation on the strongest channel.

Fine timing estimation. We aim to improve the accuracy of timing estimation in the second stage of timing estimation by exploring the information in both the time and the frequency domains. The fine timing metric $F^k(n)$ for the kth relay link is defined over a searching window centered at the updated coarse timing $\bar{\varepsilon}_k$ as

$$F^k(n) = w_t^k \bar{P_t}^k(n) + w_f^k \bar{P_f}^k(n), n \in [\bar{\varepsilon}_k - W_F, \bar{\varepsilon}_k + W_B],$$

where, W_F and W_B are user-defined parameters of the forward and backward window sizes. We use $W_B = W_F = N_g$ for simulation in Section IV; $\bar{P_t}^k(n) = \frac{\hat{P}^k(n) - min(\hat{P}^k)}{max(\hat{P}^k) - min(\hat{P}^k)}$ is the normalized time correlation metric of $\hat{P}^k(n)$ over the searching window $[\bar{\varepsilon}_k - W_F, \bar{\varepsilon}_k + W_B]$. $\bar{P_f}^k(n) = \frac{U^k(n) - min(U^k)}{max(U^k) - min(U^k)}$ is the normalized frequency metric of $U^k(n)$ over the searching window, which is defined in Subsection D. The w_t^k and w_f^k are the combining weights. Since the peak value indicates the correct timing point, we propose to compute the

weights dynamically based on the instantaneous peak-to-average-ratio (PAR) of sequences $\{\bar{P_t}^k(n)\}$ and $\{\bar{P_f}^k(n)\}$ over the searching window, respectively,

$$w_t^k = \frac{PAR_t^k}{PAR_t^k + PAR_f^k}, w_f^k = \frac{PAR_f^k}{PAR_t^k + PAR_f^k}, \tag{3.13}$$

where

$$PAR_t^k = \frac{\max\{\bar{P_t}^k(n)\}}{\frac{1}{W_B+W_F+1}\sum_{n=\bar{\varepsilon}_k-W_F}^{\bar{\varepsilon}_k+W_B}\bar{P_t}^k(n)}, PAR_f^k = \frac{\max\{\bar{P_f}^k(n)\}}{\frac{1}{W_B+W_F+1}\sum_{n=\bar{\varepsilon}_k-W_F}^{\bar{\varepsilon}_k+W_B}\bar{P_f}^k(n)} \tag{3.14}$$

Eventually, the fine timing for the kth relay link is estimated by finding the maximum value of the fine timing metric as

$$\hat{\varepsilon}_k = \underset{n\in[\bar{\varepsilon}_k-W_F,\bar{\varepsilon}_k+W_B]}{\arg\max}\left\{F^k(n)\right\}. \tag{3.15}$$

To enhance the selection diversity and save receiver energy, we can select the qualified links with good channel condition by pre-defining a fine timing threshold T_f. The destination will process only the signals from relay node k, if $F^k(\hat{\varepsilon}_k) \geq T_f$.

3.2.3 Fractional CFO estimation

According to [54], the fractional CFO can be estimated based on the angle of the correlation metric in the time domain as $\frac{\angle P_j^k(\hat{\varepsilon}_k)}{\pi}$. Because of the special structure of our preamble with phase masks, we propose to use only the first and last correlation metrics P_1^k, and P_6^k for fractional CFO estimation as the phase masks are removed automatically when computing P_1^k, and P_6^k as long as the timing error is less than the length of the CP period.

Instead of estimating the fractional CFO for each relay link separately, we propose a combined fractional CFO estimation scheme to utilize the correlation among all copies to (this is where low CFO pre-synchronization error makes a difference) to achieve diversity

gain. The combined fractional CFO can be written as

$$\hat{\mu}_{comb} = c_1 \frac{\angle P_1^{comb}}{\pi} + c_2 \frac{\angle P_6^{comb}}{\pi}, k = 1, \ldots, K, \tag{3.16}$$

where,

$$P_1^{comb} = \sum_{k \in \mathcal{K}} P_1^k(\hat{\varepsilon}_k), \tag{3.17}$$

$$P_6^{comb} = \sum_{k \in \mathcal{K}} P_6^k(\hat{\varepsilon}_k), \tag{3.18}$$

$$c_1 = \frac{\left|P_1^{comb}\right|}{\left|P_1^{comb}\right| + \left|P_6^{comb}\right|}, \tag{3.19}$$

$$c_2 = \frac{\left|P_6^{comb}\right|}{\left|P_1^{comb}\right| + \left|P_6^{comb}\right|}. \tag{3.20}$$

$\mathcal{K}$ is a set of "qualified" relay links whose fine timing metric $F^k(\hat{\varepsilon}_k)$ exceed the threshold T_f.

Based on the autocorrelation metric in Eq.(3.9) and the fact that all the transmitters use the same preambles, the combined autocorrelation metric has the conditional expectation value

$$\begin{aligned} &E\{P_1^{comb}|h^k\} = E\{P_6^{comb}|h^k\} = \\ &= E\{\sum_{k \in \mathcal{K}} \left|h^k\right|^2 e^{j\pi\omega_k \frac{N}{2}} E_0\} \simeq e^{j\pi\omega_0 \frac{N}{2}} E_0 \sum_{k \in \mathcal{K}} \left|h^k\right|^2, \end{aligned} \tag{3.21}$$

where $\omega_k = \omega_0 + \epsilon_k$ with ω_0 as the normalized fractional CFO between source and destination, and ϵ_k as the frequency pre-synchronization error. For TDCT, when SNR is very low, the pre-synchronization error, which is a function of the SNRs at the relays, is assumed in this paper to be small enough to be ignored [72].

As we can see in Eq.(3.21), the combined fractional CFO estimation metric is weighted by the sum of magnitude squared channel gains, $\left|h^k\right|^2$, which offers the diversity gain

similar to maximum ratio combing (MRC).

3.2.4 Integer CFO estimation

The integer CFO ν_k is estimated based on the preamble in the frequency domain. Given the frequency channel response as:

$$\bar{R}_j^k(\tau) = H^k(\tau)Q_j(\tau - \nu_k), \tau = -n_g, \ldots, n_g + n_c - 1, \tag{3.22}$$

$$\mathbf{H}^k = [H^k(-n_g), \ldots, H^k(n_g + n_c - 1)]^T. \tag{3.23}$$

The received preamble of the two OFDM symbols in the frequency domain for the kth relay link with fractional CFO μ_k compensated can be expressed as

$$R_j^k(\tau) = \bar{R}_j^k * M_j^F + Z_j^k(\tau), j = 1, 2, \tag{3.24}$$

where $Z_j^k(\tau)$ is the AWGN, and M_j^F is the Discrete Fourier Transform (DFT) of the phase mask M_j.

Given the DFT of the conjugated phase masks, $\bar{M}_j^F = DFT(M_j^\dagger)$, the frequency domain preamble without phase masks can be recovered by convolution in the frequency domain,

$$\hat{R}_j^k = R_j^k * \bar{M}_j^F = \bar{R}_j^k(\tau) + \bar{Z}_j^k(\tau) \tag{3.25}$$

where, $\bar{Z}_j^k(\tau) = Z_j^k(\tau) * \bar{M}_j^F$.

Then, the integer CFO estimation is based on the frequency metric $U^k(\tau)$, which is computed as

$$U^k(\tau) = |\sum_{i=0}^{n_c-1} G^k(\tau + i)^\dagger O(i)|, \ for\ \tau \in [-n_g, n_g], \tag{3.26}$$

where, $G^k(\tau+i) = (\hat{R}_1^k(\tau+i))^\dagger \hat{R}_2^k(\tau+i+1), O(i) = Q_1(i)^\dagger Q_2(i+1)$.

When we assume the frequency channel response for adjacent subcarriers is the same ($H^k(i) \cong H^k(i+1)$), the expectation of metric U^k is

$$E\big[U^k(\tau)\big] = \begin{cases} \sum_{i=0}^{n_c-1} \big|H^k(\nu_k+i)\big|^2 \big|Q_1(i)\big|^2 \big|Q_2(i+1)\big|^2, & \tau = \nu_k \\ \delta^2_{\tau-\nu_k} \sum_{i=0}^{n_c-1} \big|H^k(\tau+i)\big|^2, & o.w. \end{cases} \tag{3.27}$$

where,

$$\delta_\Delta = E[\sum_{i=0}^{n_c-1} Q_1(i+\Delta)^\dagger Q_1(i)] = E[\sum_{i=0}^{n_c-1} Q_2(i+\delta)^\dagger Q_2(i)]. \tag{3.28}$$

Since, $\{Q_1(i)\}, \{Q_2(i)\}$ are constructed from the sequence $\{C'(i)\}$ with randomized phase, we expect the δ_Δ to be very small when $\Delta \neq 0$.

The integer CFO for the kth relay node could be estimated by searching the maximum value of the target metric $\hat{\nu}_k = \underset{\tau\in[-n_g,n_g]}{\arg\max}\big\{U^k(\tau)\big\}$. However, instead of doing this, we propose a combined integer CFO estimation metric as

$$\hat{\nu}_{comb} = \underset{\tau\in[-n_g,n_g]}{\arg\max}\big\{U^{comb}(\tau)\big\}, \tag{3.29}$$

where, $U^{comb}(\tau) = \big(\sum_{k\in\mathcal{K}} U^k(\tau)\big)^\dagger O(\tau)$. $\mathcal{K}$ is the set of "qualified" relay links.

The expectation of the combined frequency correlation metric at correct integer CFO, $\nu_k = \nu_0$, is

$$E\Big\{U^{comb}(\nu_0)\Big\} = \sum_{i=0}^{\tau_c-1} \big|(Q_1(i))\big|^2 \big|Q_2(i+D)\big|^2 \Big\{\sum_{k\in\mathcal{K}} \big|H^k(\nu_0+i)\big|^2\Big\}, \tag{3.30}$$

where ν_0 is the integer CFO between source and destination. As shown in Eq.(3.30), we observe that the combined correlation result is weighted by $\sum_{k\in\mathcal{K}} |H(\nu_k+i)|^2$. Therefore,

the combined integer CFO estimation, $\hat{\nu}_{comb}$, based on the combined frequency metric, also achieves diversity gain.

3.3 Simulation Study of MSE of Synchronization Parameters Estimation

Monte Carlo simulations are performed to simulate the proposed synchronization algorithm for both TDCT relaying and conventional SISO relaying. Of 128 subcarriers, 112 are used for preamble design. The CP length normalized to the sampling duration is eight. The CFO is set to be $2.2\times$subcarrier spacing for all relay links, and $t_{proc} = 100T_s$. We evaluate the MSE performance of symbol timing and CFO estimation under the frequency-selective channel with the exponential power delay profile model in [75] with a sampling period of $T_s = 10^{-7}s$ and a RMS delay spread of $50ns$. More than 10,000 trials were simulated. We set the variance of pre-synchronization frequency and timing error to be $\delta_\epsilon^2 = 0.029$ppm and $\delta_e^2 = 50$ppm, respectively. The MSE for offset estimation $x \in (\varepsilon, \mu, \nu)$ is computed as $MSE_x = E\{\frac{1}{|\mathcal{K}|}\sum_{k\in\mathcal{K}}(\hat{x}^k - x^k)^2\}$, where, $|\mathcal{K}|$ is the number of "qualified" relay links used for synchronization and decoding. We considered different fining timing thresholds, $T_f = 0, 0.7, 0.8$ when $K = 8$, and $T_f = 0$ for $K = 1, 2, 4$.

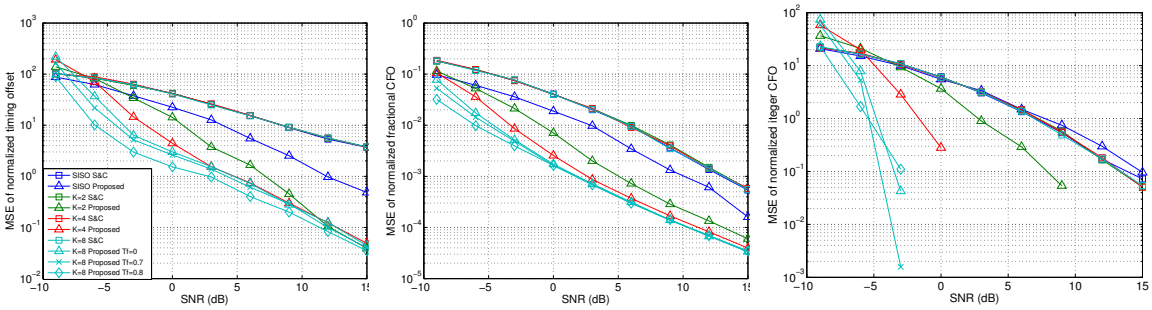

(a) Symbol timing (b) Fractional CFO (c) Integer CFO

Figure 3.4: MSE simulation results of TDCT synchronization algorithms under multipath fading channel.

The MSE performance of both timing and frequency estimation with number of co-operating relays $K \in \{1, 2, 4, 8\}$ is shown in Fig.3.4. As we can see, compared with the

S&C method, for SISO link (K=1), the proposed method has about a 5dB improvement on symbol timing estimation, and has about 3dB improvement on fractional CFO estimation. That's because the timing estimation of S&C suffers from the plateau caused by CP, and the proposed algorithm has timing and fractional CFO estimation averaged over 4 and 2 metrics with phase masks, respectively. Also, when the number of cooperating relays increases, the proposed method achieves diversity gain (as evidenced by slope changes) on symbol timing and fractional CFO at low SNR, and diversity gain on integer CFO estimation for all SNR, while the performance of S&C's method stays the same as SISO relaying. We also observe that we lose the diversity gain for timing estimation and fractional CFO starting from $K = 4$ at relatively high SNR. This happens because, for the simulation, we use only the fine timing threshold, T_f, for $K = 8$. Therefore, when the SNR is large, the timing estimation is determined mostly by the fine timing metric without diversity because of $T_f = 0$. For $K = 8$, as SNR grows, eventually, all copies get selected, then the diversity gain goes away, too.

For fractional CFO estimation, as we mentioned before, the error induced by the second and third terms in Eq.(3.21) is larger than the error induced by noise at high SNR. Therefore, we lose diversity generally. However, what matters for range extension is the diversity performance at low SNR, and as long as the error is small enough it won't affect the decoding diversity performance for TDCT.

We also observe that we are able to keep good synchronization performance while increasing the fine timing threshold for $K = 8$ in Fig.3.4. In this way, we can lower the processing energy at the destination, because the number of "qualified" relay links are decreased when the fine timing threshold increases, as shown in Fig.3.5.

3.4 Implementation on SDRs

We implement the TDCT and the proposed synchronization scheme on SDRs, and then conduct the experiments to verify TDCT benefits in the lab. The system parameters are

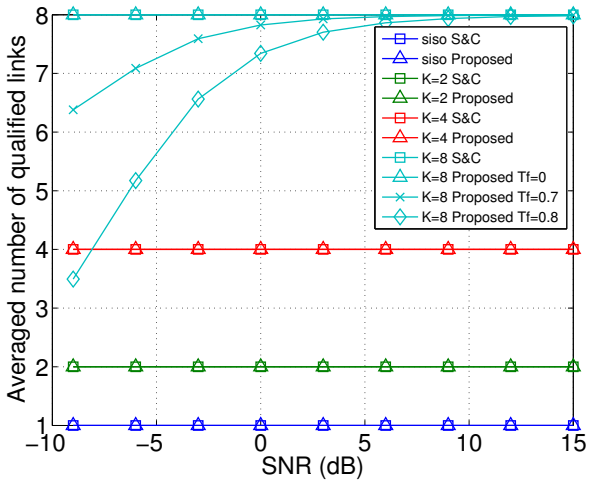

Figure 3.5: Number of qualified links.

expressed in Table 3.1.

Table 3.1: System parameters for TDCT experiments

Bandwidth	1MHz
Carrier frequency, F_c	903MHz/908MHz
Modulation	BPSK
TX power@relays	-7/-10 dBm
TX gain	12.5dB
RX gain	15.75dB
# of relays	4
payload	100 bytes
packet duration	1.9ms
FFT length	128
cp length	8
used tones	96
occupied tones	104
time interval of packets among links	0.1s
time interval between packets within link	2s

Pre-synchronization. As illustrated in Fig.3.6, the retransmission time of relay k is $T_i = t_0 + T_{proc} + (i-1)T_{gap}$, where t_0 is the time when the relay cluster receives the trigger packet from the source node, T_{proc} is the maximum processing time of relay nodes, and $T_{gap} = 0.1s$. For frequency presynchronization, the source node, S, sends out a packet every 2s using $F_c = 903$MHz. All relay nodes receive the source packet at the frequency of

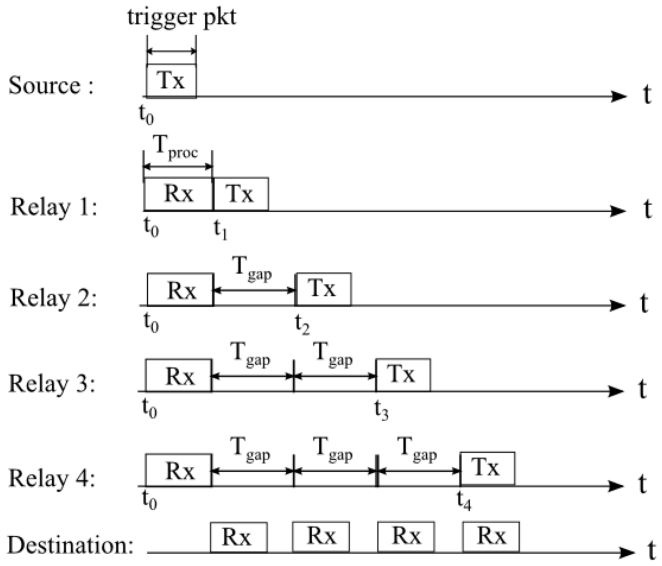

Figure 3.6: Time chart of the packet scheduling for TDCT experiments.

903MHz, and record their corresponding CFOs, $f_{is}, i = 1, 2, 3, 4$ relative to source, S. The actual retransmit carrier frequency, $F_{c,i}$, with pre-synchronization becomes $F_{c,i} = F_c + \hat{f}_{i,s}$, where $F_c = 903$MHz is the target carrier frequency.

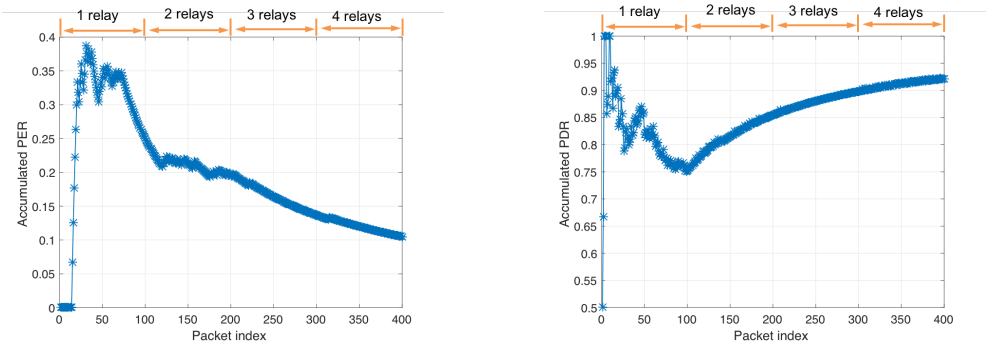

(a) PER (b) PDR

Figure 3.7: Real time decoding performance at destination with relaying power of -7dBm

Experimental Results. For the experiment, we manually control the number of the relay nodes in the system. In Fig. 3.7, the x-axis is the index of received packets at the destination, and the vertical axis is the accumulated packet error rate (PER) and accumulated packet delivery rate (PDR), respectively. During the packet index around 0-100, only relay 1 is working; during packet index around 100-200, relays 1 and 2 are working; during

packet index around 200-300, relays 1, 2, 3 are working; during packet index around 300-400, all 4 relays are working. As we can see, the PDR and PER performance improves as the number of relays increases.

3.5 Summary

In this Chapter, a method for time and frequency synchronization for OFDM-based TDCT that achieves diversity gain is proposed for range extension applications. Based on computer simulation of MSE, all three synchronization parameters show evidence of diversity gain at low SNR. In addition, the proposed synchronization algorithm and a two-hop TDCT with the help of up to 4 relays are implemented on SDR testbed. The corresponding contributions are: 1) a method of time and frequency synchronization for OFDM-based TDCT that achieves diversity gain for range extension applications; 2) a demonstration of the PER and PDR performances for both TDCT in a realistic indoor environment with a commercial software radio platform, using OFDM.

CHAPTER 4

MULTI-USER MIMO WITH AF RELAYING FOR ARRAY GAIN

4.1 Overview

A two-hop multi-user multiple-input-multiple-output (MU-MIMO) system with multiple single-antenna amplify-and-forward (AF) relays is demonstrated for the first time in a realistic indoor environment with a commercial software radio platform, using OFDM. Good trend correspondence is observed between the averaged error rate results of experiment and simulation, when zero forcing (ZF) detection is employed and a simple constraint on the average power per relay is used. The challenges of relaying a regenerated digital header and simply amplified spatially multiplexed payload are discussed. It was proven theoretically by Feng [76] that the effect of the growth of the number of fixed-gain relays is to bring the destination effectively closer to the relays. For the case of variable gain, subject to a per-node average power constraint, the destination is also brought asymptotically closer, but not as close as the fixed-gain. Our contributions are 1) to show that the gap is approximately closed by allowing relays to deactivate if their gain exceeds a threshold, and 2) to demonstrate the effects of adding AF relays using SDRs.

4.2 System Model

We assume the channel is Rayleigh frequency-flat and slow fading. The zero mean complex Gaussian channel gain $h_{i,k}$ between two nodes i and k satisfies $E[|h_{i,k}|^2] = \sigma_0^2 d_{i,k}^{-\beta}$, where σ_0 is constant, β is the path loss exponent (we use $\beta = 3$), and $d_{i,k}$ is the distance between nodes i and k. As illustrated in Fig. 4.1, the MU-MIMO system consists of a source cluster with M single-antenna users, a relay cluster with a set of single-antenna relay nodes $\{R_1, \ldots, R_K\}$, and a BS with N antennas, such that $M \leq N$. The users are assumed to

be co-located and so are the relays, yet all nodes are separated enough to have independent fading. In our case, the relay operates in AF mode in which the source's payload is amplified without any sort of signal regeneration before forwarding to the destination.

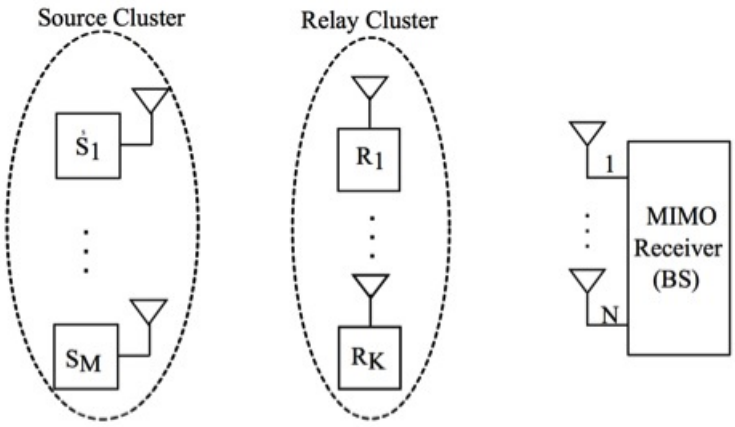

Figure 4.1: MU-MIMO with AF relays

The multiple symbols of data $\mathbf{x_s} = [x_1, x_2, \ldots, x_M]^T$ from different users in the source cluster go through the AF relay cluster , which produces at the BS:

$$\mathbf{y_D} = \mathbf{H_2 G H_1 x_s} + \mathbf{H_2 G n_R} + \mathbf{n_D}, \tag{4.1}$$

which can be re-written in terms of the compound channel matrix $\boldsymbol{\mathcal{H}}$ between the source cluster and BS, and the compound noise vector $\boldsymbol{n_c}$ as,

$$\mathbf{y_D} = \mathcal{H}\mathbf{x_s} + \mathbf{n_c} \tag{4.2}$$

where

$$\mathcal{H} = \mathbf{H_2 G H_1} \tag{4.3}$$

$$\mathbf{n_c} = \mathbf{H_2 G n_R} + \mathbf{n_D} \tag{4.4}$$

$\boldsymbol{H_1}$ is the $K \times M$ channel matrix between the source cluster and relay cluster, and $\boldsymbol{H_2}$

represents the $N \times K$ channel matrix between the relay cluster and the BS. $\boldsymbol{n_R}$ and $\boldsymbol{n_D}$ denote the additive white Gaussian noise (AWGN) at the relays and BS, respectively. The $K \times K$ diagonal matrix $\boldsymbol{G}$ contains the variable amplify gains for the AF relays, such that $g_k = \boldsymbol{G(k,k)}$.

4.2.1 Data-dependent relay gain selection

The relay operates in the AF mode in which the source's payload is amplified without any sort of signal regeneration before forwarding to the destination. In the literature, a channel-dependent, real-valued scalar gain is widely assumed; specifically, to satisfy the output power constraint [77], the amplifying gain of the kth relay, g_k, is defined as

$$g_k = \sqrt{\frac{P_k}{\sum_i |h_{k,i}|^2 P_o + \sigma_n^2}}, k = 1, \ldots, K, \tag{4.5}$$

where P_k is the scheduled transmit power of kth relay, P_0 is the transmit power of the source nodes, $h_{k,i}$ is fading channel realization between the ith user and the kth relay, and σ_n^2 is the power of the noise.

However, we found the channel-dependent relay gain is not sufficient in reality for AF. First, it is an unnecessary overhead to estimate the channel for AF relay where decoding payload is avoided. Moreover, noise could get enhanced dramatically when the AF gain is large due to the deep fading. Thus we propose to use data-dependent gain with selection defined as:

$$g_k = \sqrt{\frac{P_k}{(\sum_{i=1}^{L} |y'_{k,i}|^2)/L}}, \tag{4.6}$$

where $y'_{k,i}$ is the ith out of L time domain samples of the payload received by Relay k. Meanwhile, only the relays with gains less than a threshold are active. In this way, we avoid amplifying noise when the channel is very bad.

In joint work with other members of the Smart Antenna Research Lab at Georgia

Tech [76], Monte Carlo simulations were performed that show the effectiveness of data-dependent relay selection. We assume two users in the source cluster, two antennas on the BS ($M = N = 2$), and all relays are co-located midway between the source and BS. The results for both the fixed and dynamic variable gain strategies are shown in Fig. 4.2. As

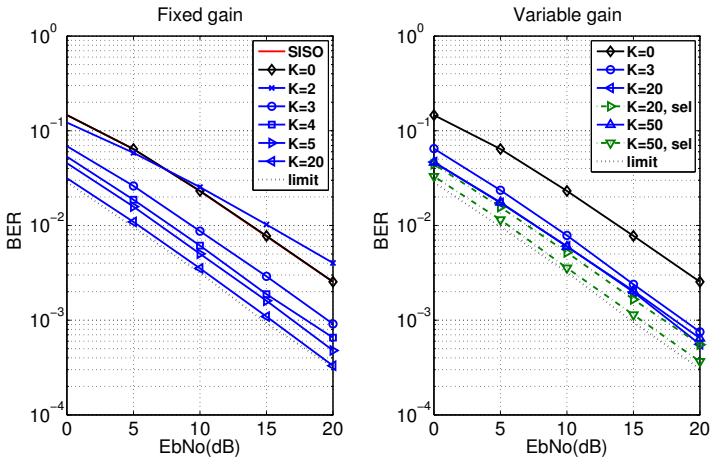

Figure 4.2: BER simulation results for muti-user MIMO ($M = N = 2$) with AF relaying under flat fading channel.

shown in Fig. 4.2, we observe $K = 20$ relays approximate the limit for the fixed gain scheme, while the performance of variable gain scheme does not reach the limit of the fixed gain scheme. Intuitively, when the instantaneous channel gain is smaller, the variable gain used by the AF relay will be large, so the noise at the relay will be amplified more compared with fixed gain. However, according to the selection selection strategy shown in Fig.4.2 with legend "sel". we observe prominent improvement for the selection strategy with $K = 50$.

4.2.2 Pre-synchronization

In a distributed system, all the nodes within the same cluster or virtual antenna array should compensate their differences in both timing offset and carrier frequency offset (CFO). Therefore, before the source cluster starts sending data, we let the BS send a trigger signal x_t directly to active users in source cluster, as a reference. All users then do pre-

synchronization in both time and frequency domains based on this trigger signal. The BS could use transmit diversity to enable the trigger signal to reach the source cluster two hops away; instead, we just increase the transmit power of the trigger signal in our experiments.

We adopt a robust time pre-synchronization algorithm for cluster transmission, similar to that in [78]. All the cooperating nodes wait to transmit for a fixed period T_{proc} after the end of the received trigger signal. So the transmiting time for ith node within the cluster is

$$T_i = T_p + t_i + T_{proc}, \tag{4.7}$$

where T_p is the deterministic duration of trigger signal, t_i represents the time the trigger waveform arrives at the antenna of the ith node in the cluster; this is also called the "start of reception" (SOR), and the processing time T_{proc} is selected so that $\alpha \times 100\%$ of transmit first-in-first-out buffer will be full when the time comes to start the transmission. α is a design parameter such that $0 \leq \alpha \leq 1$. We use $\alpha = 1$.

Another concern is the CFO caused by the difference of local oscillator. We propose that all nodes compensate the CFO to the data x_i they plan to transmit by using numerically controlled oscillator (NCO) in SDRs. The transmit signal for ith node becomes

$$x_i'(t) = x_i(t)e^{j2\pi\triangle f_i t}, \tag{4.8}$$

where $\triangle f_i$ is the estimated CFO of ith node relative to BS, which is negative of the detected CFO when the ith node decodes the trigger signal x_t.

4.3 Implementation on SDRs

4.3.1 Packet and Node Design

We design each source to use OFDM modulation, with BPSK on each subcarrier. To implement the MU-MIMO system with AF relays, we need several control parameters, such

as the payload length, number of data streams in the network, cluster ID, and payload offset. However, the AF relays do not need channel state information (CSI) for the payload because it is not decoded. To deal with this conflict, we designed a physical (PHY) layer header, which is differentially encoded with control information and therefore can be decoded by AF relay without CSI; meanwhile, the header information can be read and updated during intermediate hops. Our packet consists of a preamble and a header; each using one OFDM symbol. This is followed by a training sequence of M OFDM symbols, and finally a payload.

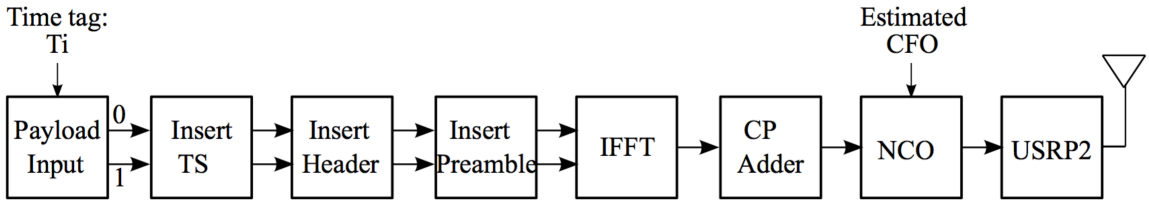

Figure 4.3: Flowgraph of source node

The C++ blocks for generating a source packet are shown in Fig. 4.3. When there are two parallel paths in the flowgraph, path 0 contains timing information, so that the source node knows the start of packet (SOP), and path 1 is the actual data stream. Otherwise, only data path is processed by the block. A time tag with scheduled transmit time based on equation (4.7) is added at SOP in the first block. The source also sets estimated CFO parameter for the *NCO* block in the end of flowgraph to do frequency pre-synchronization when a packet is generated completely.

4.3.2 AF relay transceiver

The theory of AF is simple: amplify and re-transmit the received signal. However, from an implementation point of view, AF requires some decoding. It needs some control information like packet length to coordinate the transmission. To solve this practical issue, we design the AF relay transceiver with receiver path including a DF branch and an AF branch, as shown in Fig. 4.4.

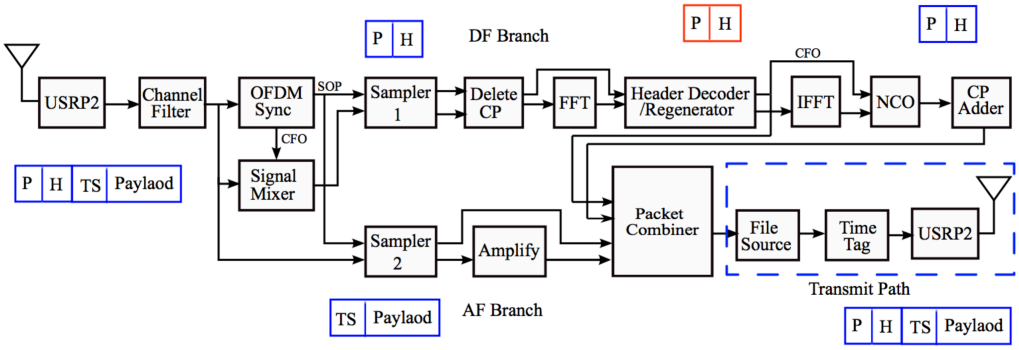

Figure 4.4: Flowgraph of designed AF relay transceiver

When a packet reaches the antenna of a relay, the *OFDM Sync* block does time and frequency recovery, and outputs SOP and CFO information. The input of the DF branch is the entire packet with CFO compensated using *Signal Mixer* block, while the input of AF branch is same but without CFO compensated. The *Sampler 1* block selects out only the preamble and header data, while the *Sampler 2* block selects out the TS and payload parts. In *Header Decoder/Regenerator* block of the DF branch, we decode the header to get all the control information, and then regenerate a new header with updated control information. Similarly as the pre-synchronization for source cluster, we use the *NCO* block to compensate the CFO in the newly generated header and preamble to keep the offsets consistent within a packet. The *Packet Combiner* block combines the new preamble and header data from DF branch and amplified payload from AF branch, and then stores them in file, which also works as the input of the transmit path of AF relay. Before the AF relay starts its transmit path, a time tag with scheduled transmit time information is added at the SOP for pre-synchronization in the time domain.

4.3.3 MIMO receiver (BS)

To build the MIMO receiver in SDRs, we synchronize multiple USRP2s using a reference clock distributor (RCD) board that we created in our lab. It provides 1 pulse per second (pps) timing reference and 10MHz frequency reference to USRP2s, so that all USRPs used

at the receiver will have same time and frequency offset. The synchronized USRP2s are connected to a single PC to set up the MIMO receiver, as shown in Fig.4.7(c).

We implement a symmetric MU-MIMO system with the antennas of MIMO receiver equal to the number of users ($M = N$). The ZF detection algorithm of VBLAST [15] is adopted as decoding algorithm for our MIMO receiver.

The receiver is implemented with the flowgraph shown in Fig. 4.5. For OFDM, the received signal is first synchronized by finding the SOP time and CFO, then the cyclic prefix (CP) is removed. After transforming the time domain signal back to the frequency domain by doing FFT, the *OFDM Frame Acquisition* block starts estimating the compound channel $\mathcal{H}$ directly based on TS, which go through the exactly same compound channel as payload. We implement the ZF algorithm in the *OFDM Block Decoder* block. The *OFDM Frame Sink* block demodulates the data using minimum distance detection, packs the decoded data, and then sends it to the higher layer.

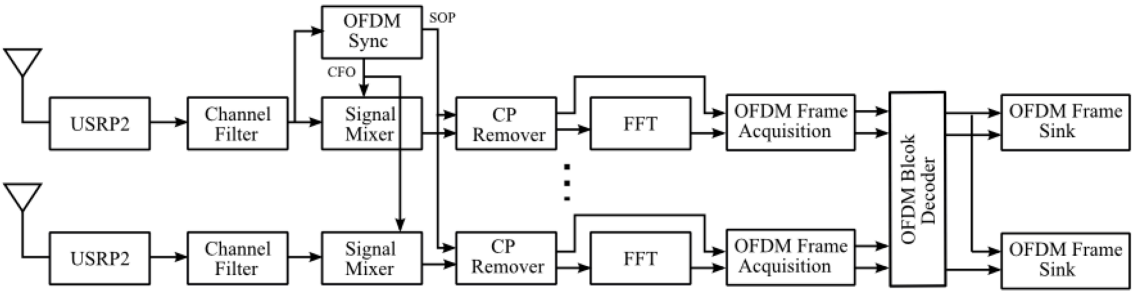

Figure 4.5: Flowgraph of MIMO receiver

4.4 Experimental Study of Two-hop MU-MIMO

We aim to show the performance improvement of MU-MIMO with AF relays, in SDRs, by observing the BER or PER of MU-MIMO with different numbers of relays. The nodes are deployed (see Fig. 4.7) with 2 users, a relay cluster (up to 6 relay nodes), and MIMO receiver with 2 antennas, in a typical academic office building as shown in Fig. 4.6. We put the relay cluster symmetrically in the middle between the sources and the receiver. When

number of relays $K \neq 0$, we let the relay node receive and re-transmit using a different carrier frequency to force the signal received by the BS go through relay cluster. The system parameters we use are shown in Table 4.1.

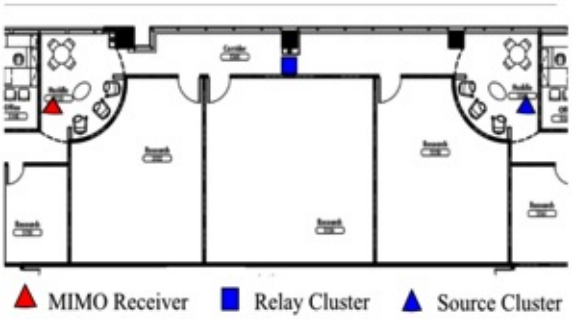

Figure 4.6: The floor plan with nodes deployment

(a) Source nodes (b) relay cluster (c) MIMO receiver

Figure 4.7: Equipment setup for MU-MIMO with AF relaying.

Table 4.1: System parameters on MU-MIMO with AF relaying experiments.

Modulation	BPSK
Sampling rate	1 MHz
FFT length	104
Occupied subcarriers	96
CP length	8

First, we compare the BER performance of MU-MIMO without relays ($K = 0$) and with 2 AF relays ($K = 2$) in fixed locations, for different transmit powers P_0 and without error correction coding (ECC). In practical radio systems, it is easier to measure packet error rate (PER) rather than BER. The CRC error check determines if the received packet is corrupted. The estimated BER (EBER) can be calculated by $EBER = 1-(1-PER)^{1/D}$ when no ECC is used, where D is the number of bits in a packet. For each transmit power, we measure PER averaged over about 2000 packets with 952 bits for every packet. The EBER curves (not shown because of space limitations) for transmit power ranging from -10dBm to -5dBm, show an approximate straight-line decrease on a semi-log graph, with the $K = 0$ and $K = 2$ cases nearly overlaying, except the $K = 2$ case performs slightly better at -10dBm. For higher power or shorter range, the advantage of the relay gains is apparently outweighed by their inserted noise for K=2.

To verify the range extension, we test the PER at the receiver. During a 5 minute period, the receiver sends a trigger signal every 0.5s, and we increase number of relays every minute, from 2 to 6. We look at transmit powers P_0=-10dBm, -8dBm, and -6dBm, indicating bad, fair, and good EbNo at the receiver, respectively, and the PER is averaged over 10 trials. In practice, self-fading is caused by relay timing error when multiple relays use the same channel resource. For the 2×2 case, we overcome this problem with half-rate convolutional ECC and interleaving. The PER results are shown in Fig.4.8.

As Fig.4.8 shows, the biggest improvement comes when we increase the number of relays from two to three, and improvements for more relays are small, which is similar to the simulation result with variable channel gain done by other member in our lab. We observe that the experimental SNR improvement of only 1 dB is smaller than in the simulation; we think this may have been caused by interference that we noticed in this band after the experiment. We also observe that the slope is higher experimentally than in simulation. We attribute this to the frequency diversity in the experiment resulting from self and real fading and the ECC plus interleaving.

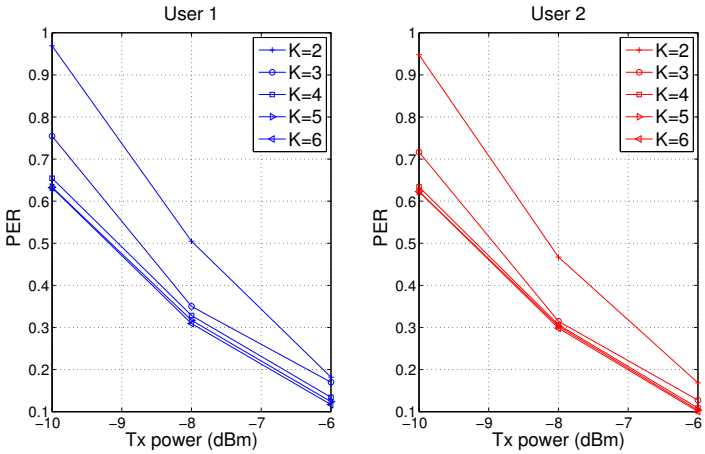

Figure 4.8: Averaged PER for MU-MIMO with different numbers of relays

4.5 Summary

In this Chapter, we implement MU-MIMO with single-antenna AF relays in SDRs by specifically designing the packet and the AF tranceiver to overcome practical issues, such as pre-synchronization for cluster transmission. The averaged error rate is evaluated by both simulation and experiments with good correspondence. In a joint work, it is proven theoretically that the effect of the growth of the number of fixed-gain relays is to bring the destination to the location of the relays. The corresponding contributions are: 1) design the PHY structure of packet and the AF transceiver; 2) an AF relay selection scheme that avoids noise enhancement; and 3) a demonstration of the packet error rate (PER) performance for MU-MIMO with AF relaying in a realistic indoor environment with a commercial software radio platform, using OFDM.

CHAPTER 5

ON-DEMAND NETWORK MIMO FOR LOW POWER WIDE AREA (LPWA) APPLICATIONS

5.1 Overview

In this Chapter, we propose a PHY layer solution for the uplink in a one-hop multi-gateway wireless packet network as illustrated in Fig.5.1. The key idea is that we combine two existing technologies, decoding with "capture and SIC" (C&S) at the gateways for some packets and decoding with "network MIMO" (NMIMO) in the cloud for other packets, for reliability, range extension, and low-cost network MIMO implementaion for low-power transmit-only (TO) sensors. Because of this packet-selective application of network MIMO with a distributed receiver array, we name our approach "On-Demand Network MIMO". In principle, the proposed technique applies to the LPWA network, which has emerged as a significant high-coverage, low-bandwidth, low-cost per connection, and years-long battery life component of the Internet of things (IoT).

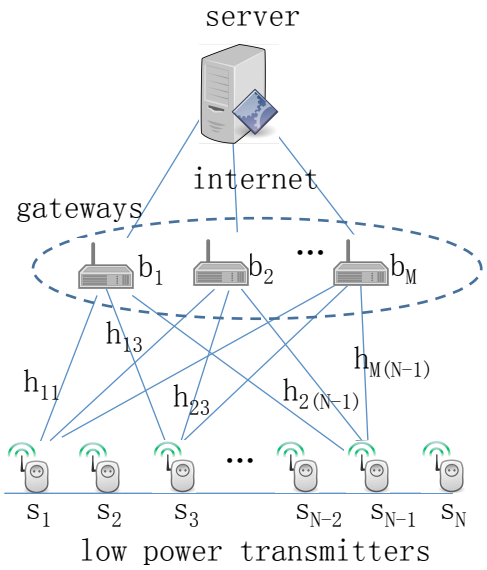

Figure 5.1: Proposed network architecture for on-demand NMIMO.

Modulation, Spreading, and Coding. We consider a transmitter system that combines turbo code forward error correction (FEC), Gold code spreading, and minimum shift keying (MSK) modulation. We adopt turbo codes because they are asymmetric, meaning that their simple encoding can be done at sensor nodes with its limited energy whereas the gateway, which is not power limited, can do the complex decoding; we adopt the phase spreading sequence (PSS) approach to spread spectrum continuous phase modulation (CPM) [79], in which non-spread bits are mapped to spreading sequences, prior to the CPM modulator, thereby maintaining the bandwidth efficiency of CPM. We selected Gold codes because they have good properties for both autocorrelation and cross-correlation. In the proposed design, we assume all users employ the same spreading sequence. The payload information bits are Turbo encoded and then spread. The resulting chips are modulated using an MSK modulator.

5.2 On-demand Network MIMO Approach

5.2.1 C&S at the GW

When a GW first successfully decodes a packet, based on passing a CRC check, it forwards that packet to the server and the other GWs through the internet. No following copies of the packet are forwarded. Each GW stores a certain number of its latest physical layer samples. When a packet has been decoded, its corresponding physical layer samples are synthesized or regenerated and subtracted from the stored samples; this is interference cancellation (IC). In other words, if IC is perfect, after subtraction, the stored samples appear as though the decoded packet had never been transmitted. The benefit of cancellation is that weaker packets may be revealed and subsequently decoded and forwarded to the server and the other GWs; Successive interference cancellation (SIC) is the repeated application of Capture and Interference Cancellation. “Local SIC” happens when a GW cancels a packet that it decoded. “Global SIC” happens when a GW cancels a packet that another GW decoded and forwarded. Global SIC is a form of GW cooperation [80].

Packet Construction 1. For capture and SIC (C&S), we assume the packet has a known preamble followed by an unknown payload. We use the preamble for packet detection, synchronization and channel estimation (DS&CE). For the purposes of this work, we assume header and control information is part of the payload.

5.2.2 NMIMO in the cloud

Only when requested, each gateway node (or listener) forwards the compressed physical layer samples of packets to a server, which decodes the packets using MIMO techniques; this functionality could be described as selective application of multi-user MIMO with a distributed receiver array. The spatial multiplexing capability of MIMO enables packets that have too much interference at the gateways to be decoded at the server, thereby supporting energy-saving transmit-only strategies.

Packet construction 2. For the NMIMO, we add a post-amble to the end of the first construction, such that the post-amble is the same as the preamble. The post-amble is useful for DS&CE for trailing packets in an offset overlapping packet scenario, when the preamble of the trailing packet is interfered by the leading packet ("offset" means that the interfering packets are not aligned in time, which is the usual case in an asynchronous network). In particular, we use the post-amble for channel estimation for MIMO processing of the overlapped parts of the interfering packets.

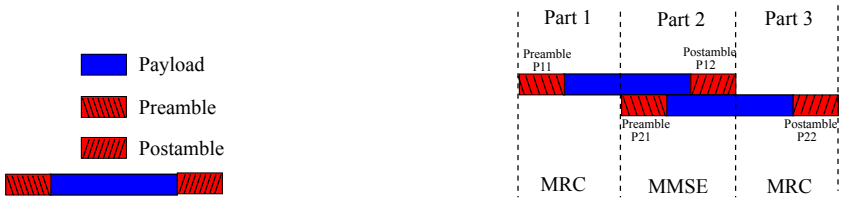

(a) Packet construction 2 (b) Overlapping scenario at GW

Figure 5.2: Illustration of NMIMO (2×2) signals at server.

When two packets overlapping at GW as illustrated in Fig.5.2, the received signal can be divided into three parts. For the best performance, it is optimal to do MRC on Part 1

and Part 3, and MMSE combining on the overlapping part in the middle. The practical challenges are identifying the overlapping part precisely, estimating the channel gains and compensating the CFOs for the two packets correctly. To deal with the practical issues, we design the packet with both preamble and postamble in the same length as illustrated in Fig. 5.2(a), so that one or the other will be interference-free and can provide optimal synchronization and channel estimation for MIMO processing.

5.2.3 Measurements on SDRs

To demonstrate On-Demand Network MIMO, we tested the feasibility of IC on GWs, and both MRC and MIMO at the server on USRP SDRs platforms over the air in an indoor environment. For the experiments, we kept the sampling rate constant and let the packet duration vary with respect to the spreading length and coding rate. The system parameters are quantified in Table 5.1.

Table 5.1: System parameters for on-demand NMIMO experiments

Payload length, information bit	48
Spreading length,	L
Code rate	R
Sample per chip, S	32
Preamble length, information bit	16
Sampling rate, F_s	$200KHz$
Carrier frequency, F_c	430MHz
Modulation	MSK

IC. Two SDRs transmit different source signals with different repetition rates, and one SDR serves as the GW. Fig.5.14(a) shows the received over-air signals with spreading length $L = 15$, code rate $R = 1$, and the TX power for two GWs are 0dBm and -5dBm respectively. As we can see, there are two types of overlapping cases. For Case 1, the back of the strong packet is overlapping with the front of the weak packet; while for Case 2 the front of the strong packet is overlapping with the back of the weak packet. The corresponding packet detection result is shown in Fig.5.14(b) with the peaks indicating

the starts of packets (SOPs). The peaks corresponding to strong packets are very sharp and clear, while the peaks corresponding weak packets are relatively lower and are not as distinct as they are when there is no interference.

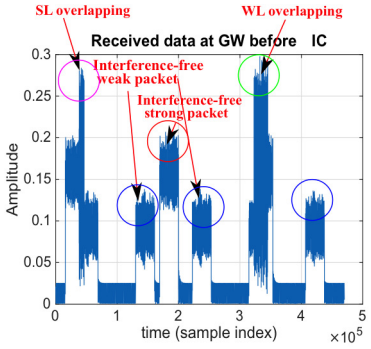

(a) Amplitude of received signal before SIC

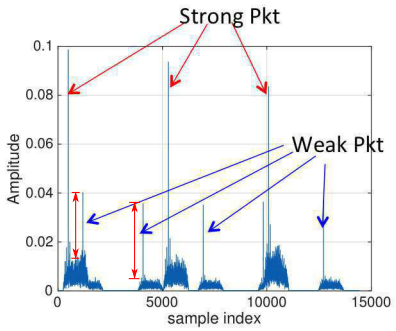

(b) Amplitude of SOP metric before SIC

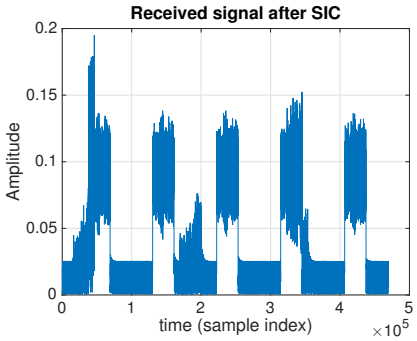

(c) Amplitude of received signal after SIC

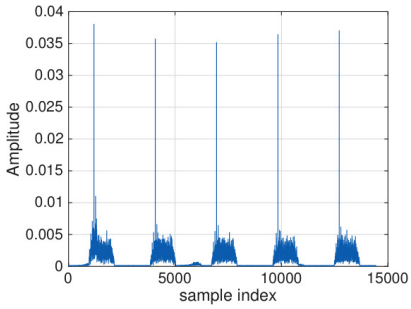

(d) Amplitude of SOP metric after SIC

Figure 5.3: The received signal at GW for SIC processing.

According to the measurements after SIC processing in Figs.5.14(c) and 5.14(d), we found the practical residual error is not constant over the packet but tends to initially worsen over time in Fig.5.14(c). We attribute this phenomenon to phase error that is accumulated in the time domain, as a result of the CFO estimation error. The error is small at the beginning because the channel estimate based on the preamble compensates for only the initial phase offset. As we can see in Fig.5.14(d), we only see clear peaks indicating the SOPs of weak packets, which demonstrates the effectiveness of the cancellation and ability of the preamble correlation inherent in SOP estimation to suppress the interference from the residual error. Meanwhile, the weak packets are decoded without error after SIC.

Maximum ratio combining (MRC). To improve the performance for the single input and

multiple output (SIMO) case, we implement MRC to achieve diversity gain at the server. The experiments are conducted with two SDRs working as GWs, and one SDR working as transmitter.

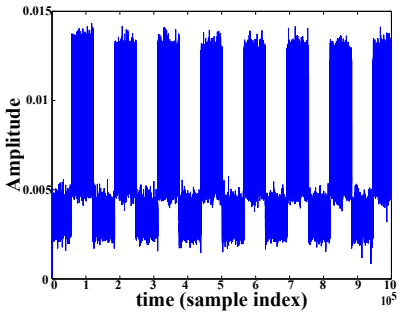

(a) Amplitude of received signal at GW1 (GW2 looks similar)

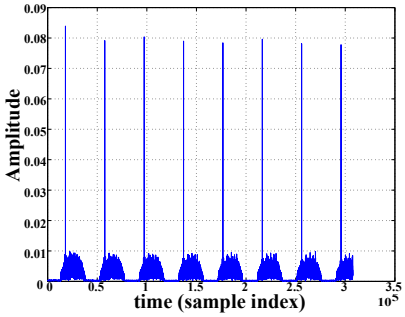

(b) Amplitude of SOP metric

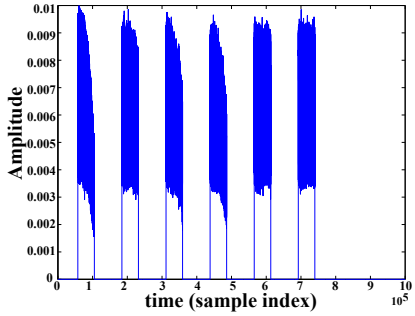

(c) Cominbed data after MRC at server

Figure 5.4: Measurements of MRC.

Table 5.2: Number of error bits result for MRC.

Pkt #	GW1	GW2	Server
1 #	0	1	0
2 #	1	0	0
3 #	0	1	0
4 #	0	2	0
5 #	0	0	0
6 #	1	0	0

The received over-air signals at GWs are shown in Fig.5.4(a) with spreading length $L = 31$, code rate $R = 0.5$, TX power$= -15dBm$. The packet detection still works fine under this low SNR as shown in Fig.5.4(b), and the two streams of weak data are combined at the server to achieve diversity gain based on MRC as shown in Fig.5.4(c). The

corresponding decoding performance is shown in Table 5.2 with transmitted payload of 48 information bits. As we can see from Table 5.2, compared to what is achieved at the GWs, MRC improves the decoding performance at the server.

MIMO. The MIMO processing includes MRC for non-overlapping parts, and MMSE weights for the overlapping interval to make the most of the MIMO benefits. Two gateways are synchronized using a reference clock distributor (RCD) board with 1ppm and 10MHz timing and frequency reference, respectively.

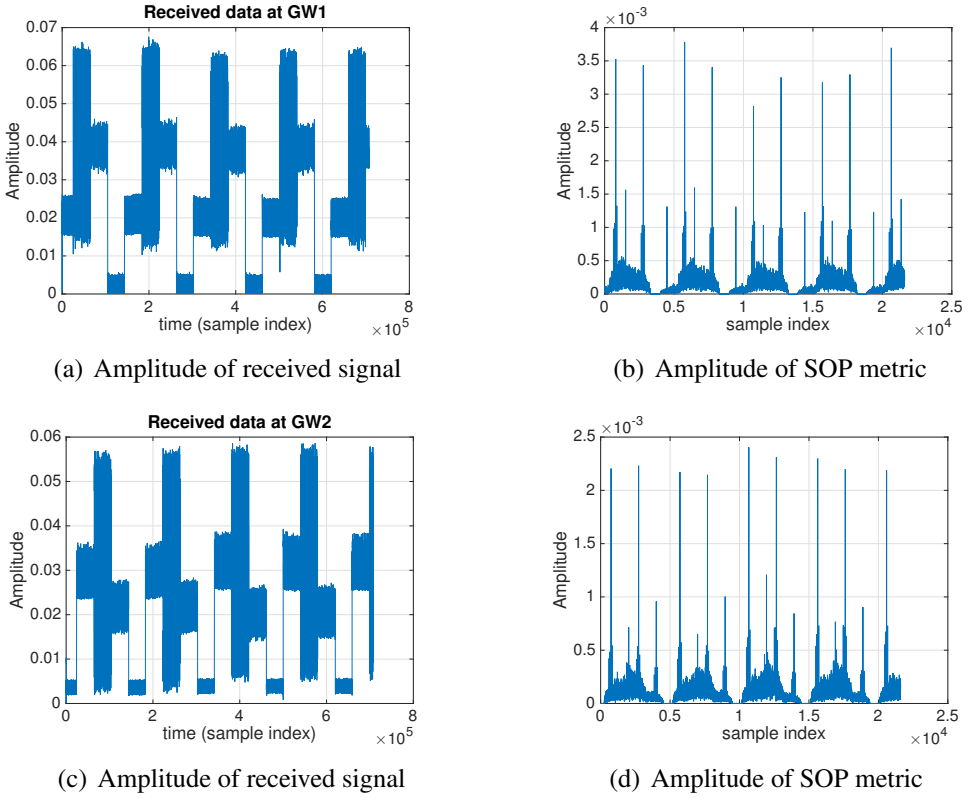

(a) Amplitude of received signal

(b) Amplitude of SOP metric

(c) Amplitude of received signal

(d) Amplitude of SOP metric

Figure 5.5: Received signal at GWs @ Tx power $= -5dBm$.

For the distributed MIMO demonstrations, the over-air signals at GWs are shown in Fig. 5.5 with spreading length $L = 31$, code rate $R = 1$. According to the corresponding SOPs estimation results in Figs. 5.5(b) and 5.5(d), the peaks with relatively larger height, indicating the start of Parts 1 and 3, are clear and reliable for synchronization and channel estimation, as we designed. Therefore, the two streams of source signal are retrieved and decoded successfully at the server.

5.3 Interference Insensitive Synchronization Scheme

Reliable synchronization and channel estimation are very crucial to leverage the benefits of SIC, MRC and MIMO in random packet overlapping scenarios with unexpected interference. We then propose a novel data-aided (DA) synchronization algorithm which applies to LPWA applications that work in high interference environments.

The whole synchronization process in terms of synchronization parameters estimation, is done in a sequential manner.

1) Frame synchronization: The first step of the synchronization process is to detect the packet and determine the start of packet by estimating the integer timing offset, $\hat{\mu}$;

2) Fine timing synchronization: Then we improve the accuracy of timing through fractional delay $\hat{\epsilon}$ estimation and compensation;

3) Carrier frequency offset estimation: Once the timing recovering is accomplished, we estimate the carrier frequency offset $\hat{\nu}$ though the proposed algorithm based on Discrete Fourier Transform (DFT).

4) Carrier phase offset estimation: Lastly, the carrier phase offset, i.e., $\hat{\theta}$, is estimated through a least-square estimator.

5.3.1 Frame synchronization

The idea of double correlation is widely adopted for frame synchronization of CPM in DA schemes [81],[82]. In the most recent work [71], Hosseini and et al. propose a packet detection criteria with a reduced-complexity double correlation metric as

$$L(n) = \sum_{d=1}^{D} \left| \sum_{k=n}^{N_p+n-d-1} r^*[k]r[k+d]s[k-n]s^*[k-n+d] \right| > \gamma_D, \tag{5.1}$$

where r and s are received and prestored preamble samples with lenght of N_p, $1 \leq D < N_p$ is a design parameter and γ_D represents the test threshold for a given D. In [71], Eq. (5.1) is only used for packet detection, and another metric is computed for SOP is estimation.

To reduce the computational complexity, we propose one normalized frame synchronization metric, M_D, which can be used to achieve packet detection and SOP estimation.

$$M_D(n) = \frac{P_n}{R_n}, \tag{5.2}$$

$$P_n(\bar{\boldsymbol{r}}_{\boldsymbol{n}}) = \sum_{d=1}^{D} \left| \sum_{k=n}^{N_p+n-d-1} \bar{r}^*[k]\bar{r}[k+d] \right|, \tag{5.3}$$

$$R_n(\bar{\boldsymbol{r}}_{\boldsymbol{n}}) = \frac{1}{2} \sum_{d=1}^{D} \sum_{k=n}^{N_p+n-d-1} \left(\left| \bar{r}[k] \right|^2 + \left| \bar{r}[k+d] \right|^2 \right), \tag{5.4}$$

where, D controls a trade-off between complexity and performance. $\bar{\boldsymbol{r}}_{\boldsymbol{n}} = \left[\bar{r}[n], \bar{r}[n+1], ..., \bar{r}[n+N_p-1] \right]$ are the received samples with length $N_p = C_p \cdot N$ after match filtering based on the pre-stored source preamble samples, $s[k], k = 0, ..., N_p - 1$ and the point-to-point multiplying operation as,

$$\bar{r}[n,k] = r[n+k]s^*[k], k = 0, ..., N_p - 1, \tag{5.5}$$

When $M_D(n)$ exceeds a threshold, a packet is declared. As the value of the threshold for packet detection is hard to be predetermined for the scenario with likely interference, we adopt the idea of CFAR[83].

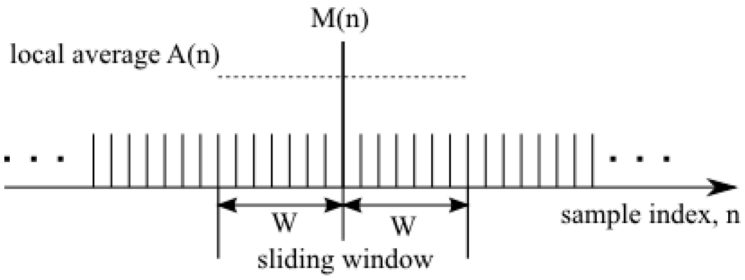

Figure 5.6: Illustration of CFAR based packet detection criteria.

The threshold is calculated dynamically by estimating the level of the noise floor around a test cell, corresponding to a particular sample index. As shown in Fig. 5.6, a sliding

window with width of 2W, centered at n, is defined for each sample index. The threshold T(n) is computed based on the local average power $A(n)$,

$$T(n) = A(n)\frac{d}{W}, \tag{5.6}$$
$$\begin{cases} A(n) = max\{A_l(n), A_r(n)\}, \\ A_l(n) = \sum_{i=0}^{W-1} M(n-i), \\ A_r(n) = \sum_{i=0}^{W-1} M(n+i) \end{cases}$$

where, $d \geq 1$ is a constant that determines probability of miss and false alarm.

The peak is selected to indicate a coming packet with the corresponding SOP or the integer timing offset estimated as

$$\hat{\mu} = n, \ s.t. \ M(n) > T(n). \tag{5.7}$$

Fig. 5.7 shows an example of the packet detection metric for three overlapping packets, with starts of packet separated by the width of the preamble. The upper two plots are the results of our metric in terms of preamble with different number of chips. With the dynamic thresholding parameter $d = 1.3$, the upper case with preamble length of 240 chip duration successfully detects the three peaks indicating the SOPs at sample index: $242, 482, 721$, while the middle case with preamble length of 112 chip duration detects 4 peaks at sample index: $113, 225, 337, 547$ with the first thee peaks indicating the SOPs. The height of each peak relative to the noise and interference floor in our metric is a function of #chips in the preamble, more chips yield lower error floor. The bottom case is the output of Hosseini's method with preamble length of 112 chip duration, and it detects 17 peaks with only one of them indicates a real SOPs. As we can see, the conventional fixed preamble structure and fixed thresholding scheme is not a good for the scenario with packet overlapping.

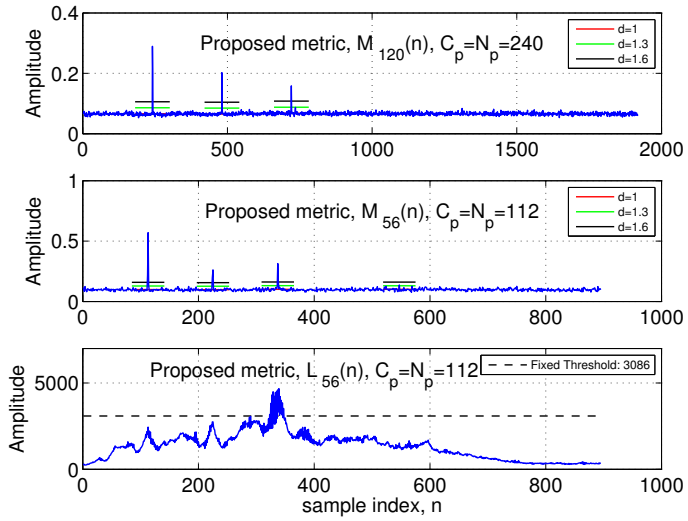

Figure 5.7: Snapshot of frame synchronization metric for three overlapped packets under AWGN channel at $Eb/No = 10dB$, when the gap between two packets is C_p .

5.3.2 Fine timing synchronization

The fundamental idea of fractional timing offset estimation is iterating possible offsets based on a oversampled sequence. To estimate the fractional time offset, ϵ, we pre-store a number of preamble sequences with non-zero offset at the receiver. These reference sequences are generated from the oversampled version of the preamble sequence, $\boldsymbol{s_n^{max}} = \{s^{max}[n], n = 0, ..., L_1 * N_{max} - 1\}$, where $s^{max}[n] = s(\frac{n}{N_{max}} T_s)$, and N_{max} is the oversampling factor.

The reference sequences with non-zero fractional delay are established by shift the oversampled sequence $\boldsymbol{s_n^{max}}$ and down-sampling as

$$\bar{\boldsymbol{s}}_k = \{\bar{s}_k[i] = s^{max}[\frac{N_{max}}{N} i - k]\}, \tag{5.8}$$
$$i = 0, ..., N_p - 1, k = 0, ..., \frac{N_{max}}{N} - 1.$$

The fine timing estimation is done based on the match filtering with pre-stored reference sequence as

$$\hat{\epsilon} = \arg\max_{k} \{ B(k) \}, \tag{5.9}$$

$$B(k) = \left| \sum_{i=0}^{\frac{N_p}{2}-1} E_k[i] E_k[N_p - 1 - i] \right|, \tag{5.10}$$

$$\boldsymbol{E}_k = \boldsymbol{r}_{\hat{\mu}} \bar{\boldsymbol{s}}_k^T = \{ E_k[i] = r[\hat{\mu} + i] \bar{s}_k^*[i] \}, i = 0, ..., N_p - 1. \tag{5.11}$$

Ideally, the match filtering result based on (Eq. (5.11)) at the right fractional offset ϵ, $\boldsymbol{E}_\epsilon$, is a constant sequence, however, because of the CFO, which cause phase continuous phase rotation in time domain, $\boldsymbol{E}_\epsilon$ is a geometrical sequences in practical system. Taking advantage of the property of geometric sequence: $E_\epsilon[i] E_\epsilon[j] = E[N_p/2 - 1]^2$ where $i + j = N_p/2$, we are able to determine the fractional delay by searching the maximum of the summation of geometric mean.

It's obvious that $\hat{\epsilon} \in [0, 1)$, and it can be normalized to $[-\frac{1}{2}, \frac{1}{2})$ for un-bias estimation purpose. Once the fractional timing offset is determined, it can be compensated by using some fractional delay filter. The received preamble $\bar{\boldsymbol{r}}'_{\hat{\mu}} = \{ \bar{r}'[\hat{\mu} + i], i = 0, ..., N_p - 1 \}$ after match filtering (Eq.(5.5)) and with fractional timing offset $\hat{\epsilon}$ compensated is then extracted for carrier offset estimation in later subsections.

5.3.3 Carrier frequency offset (CFO) estimation

The CFO estimation starts with the received preamble sequence, $\bar{\boldsymbol{r}}'_{\hat{\mu}}$, after match filtering and with timing offset compensated. Ideally, $\bar{\boldsymbol{r}}'_{\hat{\mu}}$ would be a constant sequence which has a spike at DC in frequency domain if there is no CFO. Thus, we are able to do coarse CFO estimation based on DFT operation by tracking the shift of the spike. For DFT, the resolution of minimal CFO value, f_0, which can be captured is limited by the number of bins used for DFT and the total bandwidth of the received signal. To achieve a continuous estimation range, we decompose the CFO estimation into two parts: $\nu = \alpha f_0 + \beta f_0$, where

α is an integer that represents the integer offset in terms of f_0, and $-1 < \beta < 1$ represents the fractional offset. The resolution of coarse CFO estimation, $f_0 = \frac{F_s}{N_p}$, depends on the receiver sampling frequency F_s which is limited by the bandwidth of the signal , and the DFT length N_p which is determined by the preamble length.

Coarse CFO estimation, $\hat{\alpha}$. The integer CFO is estimated as

$$\hat{\alpha} = \begin{cases} \hat{l}, & \hat{l} \leq \frac{Fs}{2} \\ -(\frac{Fs}{2} - \hat{l}), & o.w. \end{cases} \tag{5.12}$$

$$\hat{l} = \arg\max_{l}(|R(l)|),$$

$$R(l) = DFT(\bar{\boldsymbol{r}}'_{\hat{\mu}}), l = 0, ...N_p - 1$$

where, $\bar{\boldsymbol{r}}'_{\hat{\mu}} = \{\bar{r}'[\hat{\mu} + i], i = 0, ..., N_p - 1\}$ is the received filtered preamble samples with fractional delay compensated.

Fine CFO estimation, $\hat{\beta}$. The remaining fractional CFO can be derived from the angle of the autocorrelation metric in time domain with autocorrelation lag of half the preamble length,

$$\hat{\beta} = \frac{\angle \sum_{i=\hat{\mu}}^{\mu+N_p/2-1} \bar{r}'^{*}[i]\bar{r}'[i + \frac{N_p}{2}]}{\pi}, \tag{5.13}$$

The total CFO estimation result is,

$$\hat{\nu} = (\hat{\alpha} + \hat{\beta}) f_0. \tag{5.14}$$

By dividing the CFO estimation into two steps, we achieve the full CFO estimation range of $[-\frac{F_s}{2N}, \frac{F_s}{2N}] = [-\frac{f_c}{2}, \frac{f_c}{2}]$.

5.3.4 Carrier phase estimation

Carrier phase estimation is the last step in the whole synchronization process, which is needed to initialize the MSK demodulation. The preamble we used is a PN sequence, which is widely used for as training sequence for channel state information (CSI) estimation. To meet the timing and frequency synchronization requirement, the preamble as a training sequence is long enough for phase offset estimation. Therefore, we simply adopt the least-square (LS) estimator as,

$$\hat{\theta} = \angle\left(\frac{1}{N_p}\sum_{i=0}^{N_p-1}\frac{r''[\hat{\mu}+i]}{s[i]}\right) = \angle\left(\frac{1}{N_p}\sum_{i=0}^{N_p-1}\bar{r}''[\hat{\mu}+i]\right), \tag{5.15}$$

where $r''[n]$ and $\bar{r}''[n]$ are the received signal before and after match filtering with both timing and CFO compensated.

5.4 Interference Cancellation Error Modeling

In this section, we evaluate the practical residual error of IC at GWs as shown in Fig.5.1 in a flat fading environment, both theoretically and experimentally. We investigate the mean, variance, and distribution of the residual error-to-signal ratio (ESR) for the two-packets overlapping scenario based on average over the interfered part of the packet. In contrast to the conventional model, we found the ESR is a function of the signal to interference and noise ratio (SINR) on the preamble and the overlapping degree. The theoretical statistics of the residual error assume ML estimation of synchronization offsets. The theoretical residual error trends are verified through experiments using software-defined radios. Unlike the conventional residual error model, the instantaneous residual error of IC increases with time, with a magnitude determined by synchronization errors, varies for different overlapping scenarios, and primarily depends on the SINR of the stronger packet preamble.

5.4.1 Instantaneous residual error

When considering MSK, a binary continuous phase modulation (CPM), the complex baseband signal from a transmitter can be expressed as

$$x(t) = \sqrt{\frac{2E_c}{T_c}} exp\{j\phi(t;\alpha)\}, \tag{5.16}$$

where E_c is the energy per transmitted symbol with duration T_c. $\phi(t;\alpha)$ is the phase of the signal, which is represented as

$$\phi(t;\alpha) = 2\pi d \sum_{i=0}^{L-1} \alpha_i q(t - iT_c), \tag{5.17}$$

where α_i is a sequence $\{\alpha_0, \alpha_1, \ldots, \alpha_{L-1}\}$ of bits such that $\alpha_i \in \{\pm 1\}$. L is the total number of source bits for one packet, so that $L = L_1 + L_2$. The variable d is the modulation index of CPM, and $d = \frac{1}{2}$ for MSK. The waveform $q(t)$ is the phase response of MSK.

We assume the flat fading channel is modeled as $h = \gamma e^{j\theta}$, where γ is the magnitude and θ is the phase. The complex baseband representation of the received signal is

$$y(t) = e^{j(2\pi f_d t)} h x(t - \tau) + z(t), \tag{5.18}$$

where f_d is the frequency offset, τ is the timing offset, and $z(t)$ is complex baseband AWGN with zero mean and power spectral density N_0. In practice, $y(t)$ is sampled N times per symbol with sampling rate of f_s. This results in a discrete-time version of of received signal as

$$y[i] = y(\frac{iT_c}{N}) = e^{j(2\pi\omega i)} h x[i] + z[i], \tag{5.19}$$

where $\omega = f_d T_c / N$ is the normalized frequency offset with respect to the sampling frequency. $x[i] = x(\frac{iT_c}{N} - \tau)$ and $z[i]$ are the sampled versions of $x(t - \tau)$ and $z(t)$, respec-

tively.

In practical IC, the subtraction of the decoded packet is not perfect due to the imperfect synchronization and channel estimation. An interference-insensitive timing synchronization approach is available [84], therefore we assume the timing synchronization is perfect. Let ω, $\hat{\omega}$ be the real and estimated normalized carrier frequency offsets (CFOs), respectively, between the TX and GW. Let $\hat{h} = \hat{\gamma}e^{j\hat{\theta}}$ be the estimated channel. The residual IC error at sample index i for the successfully decoded packet $y[i]$ after subtracting the reconstructed signal $\hat{y}[i]$ becomes:

$$\begin{aligned} e[i] &= e^{j(2\pi\omega i)}hx[i] - e^{j(2\pi\hat{\omega}i)}\hat{h}x[i] \\ &= x[i]\bigg(\gamma e^{j(2\pi\omega i+\theta)} - \hat{\gamma}e^{j(2\pi\hat{\omega}i+\hat{\theta})}\bigg). \end{aligned} \tag{5.20}$$

Let $\beta_i = 2\pi\omega i + \theta$, $\hat{\beta}_i = 2\pi\hat{\omega}i + \hat{\theta}$, and $\Delta\beta_i = \beta_i - \hat{\beta}_i$. Then the magnitude squared of the residual error is

$$\begin{aligned} |e[i]|^2 &= e[i]e^*[i] \\ &= |x[i]|^2\bigg(\gamma^2 + \hat{\gamma}^2 - \gamma\hat{\gamma}e^{j\Delta\beta_i} - \hat{\gamma}\gamma e^{-j\Delta\beta_i}\bigg) \\ &= |x[i]|^2\bigg(\gamma^2 + \hat{\gamma}^2 - 2\gamma\hat{\gamma}cos(\Delta\beta_i)\bigg). \end{aligned} \tag{5.21}$$

Define the errors in the channel and CFO estimates to be $e_\gamma = \gamma - \hat{\gamma}$, $e_\theta = \theta - \hat{\theta}$, $e_\omega = \omega - \hat{\omega}$, respectively. The expectation of instantaneous residual error after cancellation becomes

$$E\{|e[i]|^2\} = \sigma_s^2 E\bigg\{\gamma^2 + \hat{\gamma}^2 - 2\gamma\hat{\gamma}cos(2\pi e_\omega i + e_\theta)\bigg\}, \tag{5.22}$$

where σ_s^2 is the average transmitted signal power. According to Eq.(5.22), the instantaneous residual error is not constant over the packet, and but a function of time determined by

the residual errors of channel gain, frequency and phase estimations. For larger sample index i, the residual error tends to be larger due to the larger accumulated phase offset $\Delta\beta_i = 2\pi e_\omega i + e_\theta$.

Exact Error Model, g. Based on the system model, the SINR for the weak packet after IC can be written as

$$SINR^w = \frac{P_w}{P_I + \sigma_N^s}, \tag{5.23}$$

where P_w, P_I, and σ_N^s are the average receive power of the weak packet, the residual error of the cancelled strong packet, and noise, respectively, each averaged over the weak packet interval. We may write $P_I = gP_s$, where P_s is the average received power of the strong packet, we define $g \in (0, 1)$ as the residual error factor (REF). In the conventional model widely assumed in the literature [48],[85], g is simply modeled as a constant. However, we will demenstrate that the pratical REF is a random variable (RV) conditioned on many factors, such as overlapping degree O, SINR of the strong packet preamble, etc.

5.4.2 Practical residual error model

We define an intermediate variable, the residual-error-to-signal-ratio (ESR), which is the average power of residual error over the overlapping interval, normalized by the average received power of the stronger packet over the same overlapping interval. It may be expressed as

$$ESR = \frac{E\{\sum_{I_s^s}^{I_e^s} |e_s[i]|^2 / N_{ov}\}}{E\{\sum_{I_s^s}^{I_e^s} |y_s[i]|^2 / N_{ov}\}} = \frac{E\{\sum_{i=I_s^s}^{I_e^s} |e_s[i]|^2\}}{P_s N_{ov}}, \tag{5.24}$$

where I_s^s is the starting sampling index of the overlapped portion of the stronger packet, I_e^s is the ending sampling index of the portion, N_p is the number of packet samples, $N_{ov} = I_e^s - I_s^s$ is the number of overlapping samples, and $O = \frac{N_{ov}}{N_p}$ is the overlapping degree. It

follows that

$$g = O * ESR. \tag{5.25}$$

By substituting the instantaneous residual error from Eq.(5.22), the ESR can be written as

$$\begin{aligned} ESR &= \frac{\sigma_s^2\gamma^2 N_{ov} + \sigma_s^2\hat{\gamma}^2 N_{ov} - 2\sigma_s^2\gamma\hat{\gamma}E\{\sum_{I_s^s}^{I_e^s} cos(2\pi e_\omega i + e_\theta)\}}{P_s N_{ov}}, \\ &= 1 + \xi - 2\hat{\xi}\frac{E\{\sum_{I_s^s}^{I_e^s} cos(2\pi e_\omega i + e_\theta)\}}{N_{ov}}, \end{aligned} \tag{5.26}$$

where $\xi = \frac{\sigma_s^2\hat{\gamma}^2}{P_s}$ and $\hat{\xi} = \frac{\sigma_s^2\gamma\hat{\gamma}}{P_s}$ are ratios of received signal power estimates based on estimated channel gain to the real received signal power. With enough energy on the preamble, we claim that $\xi = \hat{\xi} = 1$.

By applying the Lemma: $\sum_{k=0}^{n} cos(ak + z) = csc(\frac{a}{2})sin(\frac{1}{2}a(n+1))cos(\frac{an}{2} + z)$ [86] into Eq.(5.26), the ESR then becomes:

$$ESR = 1 + \xi - 2\hat{\xi} * K(e_\omega, e_\theta, O, I_s^s, I_e^s), \tag{5.27}$$

where

$$K(e_\omega, e_\theta, O, I_s^s, I_e^s) = \underbrace{\frac{sin(\pi e_\omega O N_p)}{sin(\pi e_\omega) O N_p}}_{C_1} * \underbrace{cos(\pi e_\omega (I_e^s + I_s^s) + \pi e_\omega + e_\theta)}_{C_2} \tag{5.28}$$

We consider two types of overlapping scenarios as illustrated in Fig.5.8: the strong leading (SL) case and the weak leading (WL) case. For the SL case, $I_e^s = N_p$ is fixed, and $I_s^s = I_e^s - ON_p = N_p(1 - O)$, while for WL case, $I_s^s = 1$ is fixed, and $I_e^s = I_s^s + ON_p = N_pO + 1$.

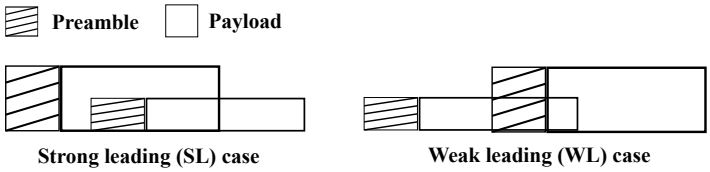

Figure 5.8: Illustration of overlapping scenarios

Therefore, the sub-term C_2 in Eq. (5.28) can be derived accordingly for SL and WL cases, and the intermediate key term K with expression of Eq.(5.28) can be re-written for different overlapping cases as

$$K^{SL} = C_1 C_2^{SL}, \tag{5.29}$$

$$K^{WL} = C_1 C_2^{WL}, \tag{5.30}$$

$$C_2^{SL} = cos\bigg(-\pi e_\omega N_p O + 2\pi e_\omega N_p + \pi e_\omega + e_\theta \bigg), \tag{5.31}$$

$$C_2^{WL} = cos\bigg(\pi e_\omega N_p O + 3\pi e_\omega + e_\theta \bigg). \tag{5.32}$$

Approximate Error Model. In the literature, there are many data-aided synchronization schemes proposed based on unbiased ML estimation algorithms. The Cramer-Rao Bound of the residual error is often studied to evaluate the performance in terms of the length of training sequence and SNR condition. We adopted the closed form of the variance for the normalized frequency and phase synchronization errors [87],[88], which are simplified at high SNR as:

$$\begin{cases} e_\omega = \frac{\hat{f}_d - f_d}{f_s} \sim N(0, \sigma_\omega^2), & \sigma_\omega^2 \simeq \frac{3}{2\pi^2 L_1^3 N^2 SINR^p} \\ e_\theta = \frac{\hat{\theta} - \theta}{\pi} \sim N(0, \sigma_\theta^2), & \sigma_\theta^2 \simeq \frac{1}{2\pi^2 L_1 SINR^p} \end{cases} \tag{5.33}$$

where L_1 is the number of bits on the preamble for synchronization, N is the sampling factor(number of samples per symbol), and $SINR^p$ is the SINR on the preamble of the strong packet.

As the number of packet samples, N_p is very large, while the normalized frequency

synchronization error, e_ω is very small, the last two terms within cosine function in both Eq.(5.31) and Eq.(5.32) are negligible, and C_1 can be approximated by the $sinc(x) = \frac{sin(\pi x)}{\pi x}$ function. Therefore the parameter K for the two overlapping cases then becomes,

$$K^{SL} = sinc(OX) \underbrace{cos(-OX + 2X)}_{C_2^{SL}}, \tag{5.34}$$

$$K^{WL} = sinc(OX) \underbrace{cos(OX)}_{C_2^{WL}}, \tag{5.35}$$

where, $X = N_p e_\omega$.

Consider the quadratic approximations of sinc and cosine functions based on the Taylor expansions[89]:

$$cos(X) = \sum_{k=0}^{\infty} \frac{(-1)^k X^{2k}}{(2k+1)!} \simeq 1 - \frac{X^2}{3!} + O(X^4) \tag{5.36}$$

$$sinc(X) = \sum_{k=0}^{\infty} \frac{(-1)^k X^{2k}}{(2k)!} \simeq 1 - \frac{X^2}{2} + O(X^4) \tag{5.37}$$

Thus, the intermediate term K used in practical residual error models can be approximated as

$$K^{SL} \simeq 1 - \frac{6 + 2O^2 - 6O}{3} X^2 - \frac{4O^2 + O^4 - 4O^3}{12} X^4 \tag{5.38}$$

$$K^{WL} \simeq 1 - \frac{2O^2}{3} X^2 + \frac{O^4}{12} X^4. \tag{5.39}$$

Define $Y = X^2$ and assume the channel gain estimates are perfect and that $\xi = \hat{\xi} = 1$. The g is then simplified as

$$g^{SL} = A_1^{SL} Y^2 + A_2^{SL} Y \tag{5.40}$$

$$g^{WL} = A_1^{WL} Y^2 + A_2^{WL} Y \tag{5.41}$$

where,

$$\begin{cases} A_1^{SL} = \frac{1}{6}(-O^4 + 4O^3 - 4O^2), \\ A_2^{SL} = \frac{2}{3}(2O^2 - 6O + 6). \end{cases} \tag{5.42}$$

$$\begin{cases} A_1^{WL} = \frac{-1}{6}O^4, \\ A_2^{WL} = \frac{4}{3}O^2. \end{cases} \tag{5.43}$$

It is straightforward to show that, $Y = X^2 \sim Gamma(\alpha, \beta)$ with α as the shape parameter and β as the rate parameter. The pdf of Y is

$$\begin{aligned} f_Y(y) &= \frac{\beta^\alpha y^{\alpha-1} e^{-\beta y}}{\Gamma(\alpha)}, \\ \alpha = \frac{1}{2}, \beta &= \frac{1}{2\sigma_X^2} = \frac{1}{2N_p^2\pi^2\sigma_\omega^2} = \frac{L\epsilon^3 SINR^p}{3}, \end{aligned} \tag{5.44}$$

where L is the total number of information bits of the packet, and $L_1 = \epsilon L$ is the number of information bits of the preamble, and $SINR^p$ is the SINR of the strong packet on the preamble.

According to the expression of ESR in Eq.(5.40), and (5.41), ESR is a function of RV, Y, with Gamma distribution. We then define the other new RV, $Z = A_1 Y^2 + A_2 Y$; it has the derived pdf, $f_Z(z)$, as

$$\begin{aligned} f_Z(z; A_1, A_2) &= \sum_{i=1}^{2} \frac{f_Y(y_i)}{|\frac{dz}{dy}|_{y=y_i}} \\ &= \sqrt{\frac{\beta}{\pi(A_2^2 + 4A_1 z)}} \left(y_1^{-\frac{1}{2}} e^{y_1\beta} + y_2^{-\frac{1}{2}} e^{-y_2\beta} \right) \end{aligned} \tag{5.45}$$

with

$$y_1 = \frac{-A_2 + \sqrt{A_2^2 + 4A_1 z}}{2A_1}, y_2 = \frac{-A_2 - \sqrt{A_2^2 + 4A_1 z}}{2A_1}. \tag{5.46}$$

Therefore, the pdf of g for the two overlapping cases are $f_{g^{SL}} = f_z(z; A_1^{SL}, A_2^{SL}), f_{g^{WL}} = f_z(z; A_1^{WL}, A_2^{WL})$ with corresponding parameters substitutions of A_1, A_2 in Eq.(5.46).

First moment statistics, $\mathbf{Mean}, \mu_Z$. Given the mean, $E[Y] = \frac{\alpha}{\beta}$ and variance, $Var[Y] = \frac{\alpha}{\beta^2}$ of gamma distribution Y, the first moment of the derived RV Z can be computed as

$$\begin{aligned}\mu_Z &= E[Z; A_1, A_2] \\ &= A_1 E[Y^2] + A_2 E[Y] \\ &= A_1(Var[Y] + E[Y]^2) + A_2 E[Y], \\ &= \frac{A_1}{\beta^2}(\alpha^2 + \alpha) + \frac{A_2\alpha}{\beta} = \frac{3A_1}{4\beta^2} + \frac{A_2}{2\beta}. \end{aligned} \tag{5.47}$$

The statistics of g, can be derived by substituting the synchronization error model in Eq.(5.33) and the parameters of A_1, A_2 into Eq.(5.47). For the mean of g for SL case is

$$\begin{aligned}&\mu_g^{SL}(SINR^p, O) = \\ &\frac{1.125O^5 - 4.5O^4 + 4.5O^3}{\epsilon^6 L^2 (SINR^p)^2} + \frac{2O^3 - 6O^2 + 6O}{\epsilon^3 L SINR^p}, \end{aligned} \tag{5.48}$$

where $\epsilon = \frac{L_1}{L}$ is the normalized preamble length.

Similarly, the mean of g for WL case can be derived as:

$$\mu_g^{WL}(SINR^p, O) = \frac{-1.125O^5}{\epsilon^6 L^2 (SINR^p)^2} + \frac{2O^3}{\epsilon^3 L SINR^p}. \tag{5.49}$$

Second moment statistics, $\mathbf{Variance}, \sigma_Z^2$. By applying the rule of expectation of Gamma distribution to the nth power, $E[Y^n] = \frac{\Gamma(\alpha+n)}{\Gamma(\alpha)\beta^n}$, the second moment of the derived RV Z

can be computed as

$$\begin{aligned}\sigma_Z^2 &= Var[Z; A_1, A_2] \\ &= E[Z^2] - E[Z]^2 \\ &= E[(A_1 Y^2 + A_2 Y)^2] - \mu_Z^2 \\ &= A_1^2 E[Y^4] + A_2^2 E[Y^2] + 2A_1 A_2 E[Y^3] - \mu_Z^2 \\ &= A_1^2 \frac{\Gamma(\alpha+4)}{\Gamma(\alpha)\beta^4} + A_2^2 \frac{\Gamma(\alpha+2)}{\Gamma(\alpha)\beta^2} + 2A_1 A_2 \frac{\Gamma(\alpha+3)}{\Gamma(\alpha)\beta^3} - \mu_Z^2. \end{aligned} \tag{5.50}$$

By substituting Eq.(5.47) and $\Gamma(n) = (n-1)!$ into Eq.(5.50), the second moment of Z then becomes

$$\sigma_Z^2(A_1, A_2) = \frac{6A_1^2}{\beta^4} + \frac{3A_1 A_2}{\beta^3} + \frac{A_2^2}{2\beta^2}. \tag{5.51}$$

Therefore, by substitution the corresponding parameters into Eq.(5.51), the variance of the error model, g is

$$\sigma_{g^{SL}}^2(\bar{A}_1^{SL}, \bar{A}_2^{SL}), \sigma_{g^{WL}}^2(\bar{A}_1^{WL}, \bar{A}_2^{WL}). \tag{5.52}$$

As we can see in Eqs.(5.47) and (5.50), the first and second moments of the proposed residual error models are determined by parameters $A_1(O), A_2(O)$ and $\beta(SINR^p)$, which are functions of overlapping degree, O, and the SINR of the strong packet preamble.

5.4.3 Simulation study on the statistics

In this section, the proposed metric REF g with/without (w/wo) approximation are simulated for the two overlapping cases versus SINR of the strong packet, where $SINR = \frac{P_s}{P_w + \sigma_n^2}$, and overlapping degree O under different $SNR = \frac{P_s}{\sigma_n^2}$ with preamble ratio, $\epsilon = 0.25$.

We evaluate the performance under three SNR values:10dB,15dB, and 20dB. The sam-

ple mean and variance of g, without approximation represented by Eqs.(5.25) and (5.26), are simulated and compared to the approximated mean as in Eqs.(5.48) and (5.49) and variance as in Eq. (5.52) using 100,000 Monte Carlo trails.

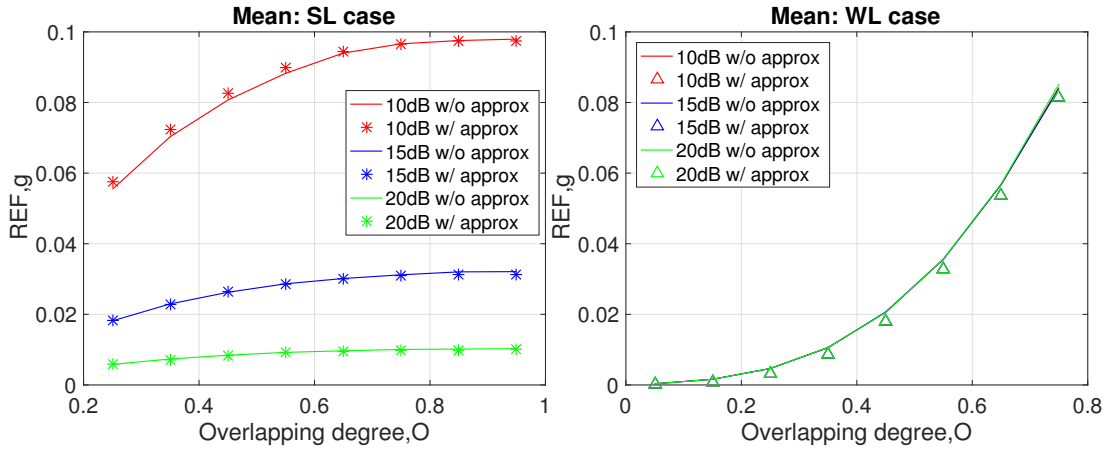

(a) Mean: SL case (b) Mean: WL case

Figure 5.9: g versus overlapping degree, O with fixed $SINR = 7dB$.

Statistics of g with respect to O

For the simulation results in Figs.5.9, all solid curves are results for the mean and variance based on the theoretical analysis in Section 5.4.2 without approximation, while all symbols represent corresponding statistics simulation based on the analysis in Section 5.4.2. As we can see, the mean and variance of proposed practical residual error model matches the approximated analysis very well, only few disagreements at the low overlapping degree O for low SNR because of the approximation of the phase error and the Taylor expansion error.

According to the simulation results in Fig.5.9, the practical g for SL case increases with the growth of the overlapping degree, O but with decreased slope, meanwhile affected by SNR of the strong packet. This is because, there is no interference on preamble for the SL case when $O > \epsilon = 0.25$. In other words, the SINR on the preamble equals the SNR of the packet, that is, $SINR^p = SNR$. As $g = ESR * O$, the slope indicates the ESR, which

determined by the averaged residual error power over the interference interval. For SL, as the highest instantaneous residual error is always captured first, the slope decreases with the overlapping degree, O.

On the other hand, the statistics of the WL case with interference on the preamble increases with the growth of the overlapping degree O but with a increased slope, and stays constant at different SNR. This happens because the SINR of the strong packet preamble matters for the WL case. And the lowest instantaneous residual error is always captured first, which makes the slope or the ESR decrease over O. Because of space limitation, we did not show the variance. The variances curves have the similar shape as the corresponding mean curves.

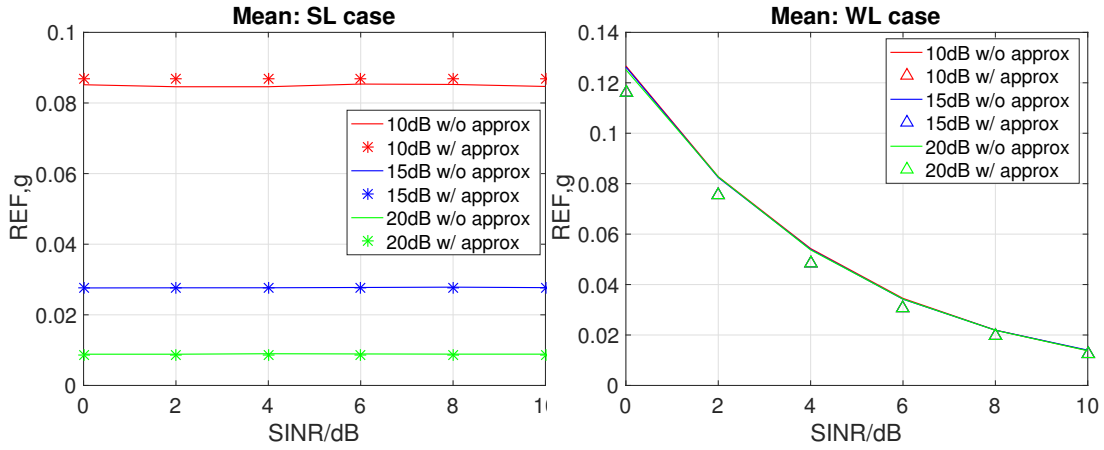

(a) Mean: SL case

(b) Mean: WL case

Figure 5.10: g versus $SINR$ with fixed overlapping degree, $O = 0.5$.

Statistics of g with respect to $SINR$

In Fig.5.10, with fixed overlapping degree, O, the statistics of the SL case are constant with respect to $SINR$ but decrease with growth of SNR, as we expected. This is because of the synchronization performance improves with the increase of the preamble SINR, which is just SNR when there is no interference. On the other hand, the statistics of g for WL case

decrease with the growth of SINR, but are same at different SNR, as expected.

The distribution of PREF, g

In this subsection, we simulate the distribution of the practical residual error factor g. The sample distribution based on the synchronization error model represented by Eq.(5.33) is compared with the theoretical analysis result in Eq.(5.45) at fixed SNR, SINR, and overlapping degree.

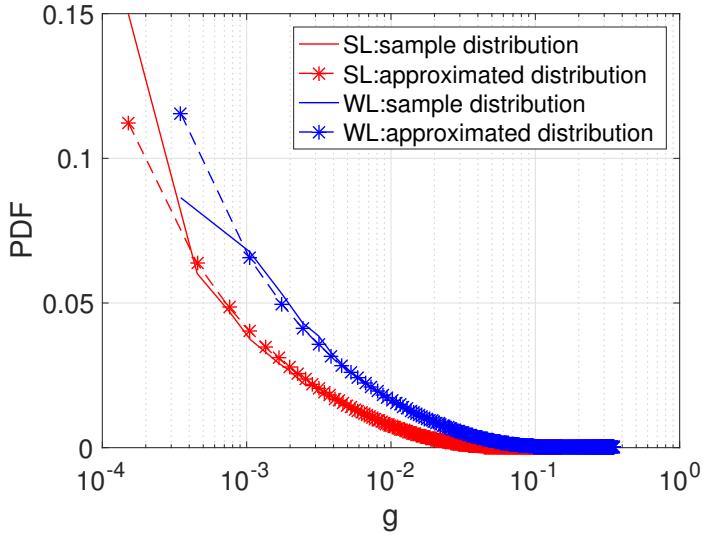

Figure 5.11: Simulation on the distribution of of $g(SINR^p, O)$ at $SNR = 20$dB, $SINR = 7$dB, overlapping degree$O = 0.5$.

According to the simulation results in Fig.5.11, the distribution of practical residual error matches our theoretical analysis.

5.4.4 Experiment design and measurements

In this subsection, we design and conduct a large number of experiments to measure the defined metric ESR, based on the successful decoding sets with BER of zero. We employ three software defined radios (SDRs), as shown in Fig.5.12, to conduct the experiment. Two of them are the transmitters, and the other one is a GW. They are connected through cable, power splitter, and attenuators to avoid the effect of unstable channel.

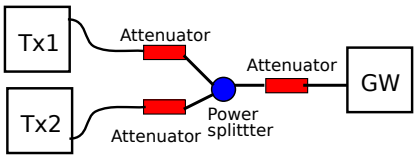

(a) The diagram of experiment setup

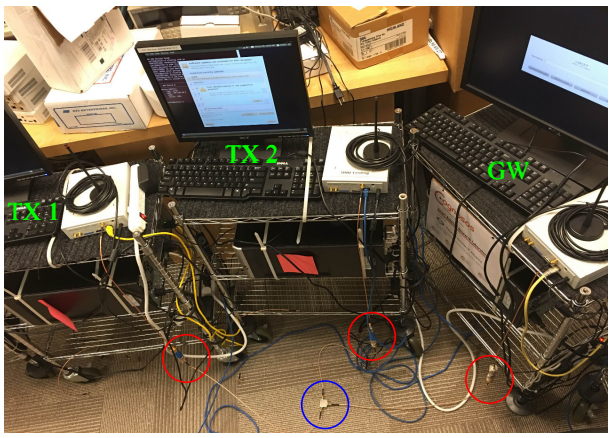

(b) The photo of experiment setup

Figure 5.12: Illustration of experiment setup. (* antenna was disabled for the experiments; red circle: attenuator; blue circle: power splitter.)

A) Experiment Design. According to the theoretical analysis in Eq.(5.22), we know the practical residual error is determined by synchronization performance, channel estimation performance, as well as signal and noise powers. Therefore, we design the experiment in terms of a set, as illustrated in Fig.5.13, to evaluate the residual error in terms of SNR, SINR, and random overlapping scenario. As shown in Fig.5.13(a), the two TXs are scheduled to transmit packets continuously at different repetition rates once activated at time $t_{0,1}$ and $t_{0,2}$, respectively. By controlling the delay between the start times $t_\Delta = |t_{0,1} - t_{0,2}|$, we are able to create different overlapping degree situations. When Tx1 with repetition rate $R_1 = \frac{1}{3}$ transmits at lower power, and TX2 with repetition rate $R_2 = \frac{1}{5}$ transmits at higher power, the designed received signal at GW is illustrated as Fig.5.13(b), which has a repetition pattern as well. Each set contains both overlapping cases SL and WL, for a particular overlapping degree, O. We also have one interference-free reference of the strong packet and three interference-free references of the weak packet for each set.

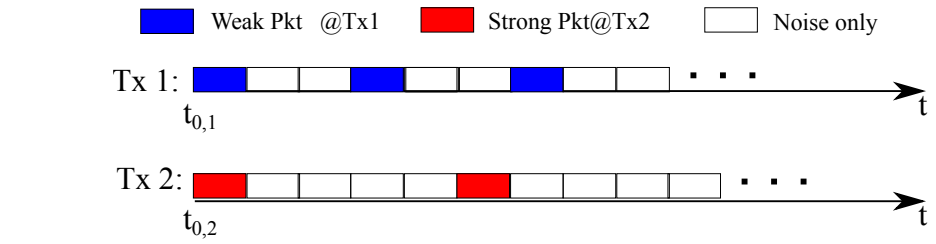

(a) Packet transmission schedule

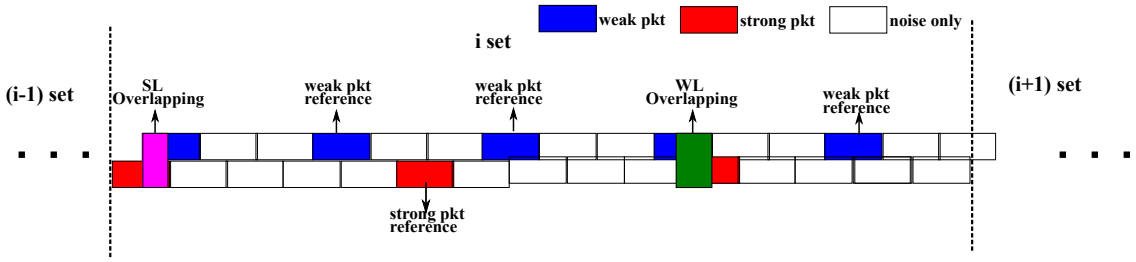

(b) Designed received signal at GW

Figure 5.13: Illustration of experiment design

In the experiment, we do not have access to instananeous residual error $e_s[i]$. Instead, we measure random outcomes of ESR, approximated as

$$ESR = \frac{|E\{|\hat{y}_w|^2\} - E\{|y_w|^2\}|}{E\{|\hat{y}_s|^2|\} - \hat{\sigma}_n^2}, \tag{5.53}$$

where $\hat{y}_w$ is a weak packet with residual error after subtracting of strong packet, y_w is an interference-free weak packet, $\hat{y}_s$ is the overlapping part of an interference-free strong packet, and $\hat{\sigma}_n^2$ is the estimated noise power.

For the experiment, we use a payload length of 48 information bits and a basic preamble length of 16 information bits. The other system parameters for the experiments are listed in the table below.

We transmit large numbers of sets at different transmitter power levels, overlapping degrees, and spreading factors. We calculate the average residual error factor ESR based only on the successfully decoded sets with BER of zero. Each average is based on 200 sets.

Fig.5.14(a) shows the experimentally received signals, which match the set definition

Table 5.3: System Parameters for Residual Error Measurements of IC

Carrier frequency	430MHz
Sampling rate	$F_s = 200KHz$
Samples per chip	$N = 32$
Spreading factor	$C = 15$
Modulation	MSK
Preamble ratio	$\epsilon = 0.25$
Packet length	$L = 64$

in Fig.5.13(b). The corresponding packet detection metric is shown in Fig.5.14(b) with the peaks indicating the starts of packets (SOPs). The peaks for the strong packets are higher than for the weak packets. The red double-ended arrows in Fig.5.14(b) indicate the difference between the peak of the metric and the "noise" level near the peak; this difference is proportional to the SINR of the preamble. Thus Fig.5.14(b) reflects that the preamble for the second weak packet, which is an interference-free reference, has a higher SINR than the preamble of the first weak packet, which has interference.

According to the measurements after IC processing in Figs.5.14(c) and 5.14(d), we find the instantaneous residual error is not constant over the packet but tends to initially worsen over time in Fig.5.14(c) as we expected based on Eq.(5.22). The error is small at the beginning because the channel estimate based on the preamble compensates for the initial phase offset. As we can see in Fig.5.14(d), we only see clear peaks indicating the SOPs of weak packets, which demonstrates the effectiveness of the cancellation and ability of the preamble correlation inherent in SOP estimation to suppress the interference from the residual error. Meanwhile, the weak packets are decoded without error after IC.

We conduct experiments to demonstrate the effects of SNR and SINR by controlling the TX powers of the overlapping packets. The scatter plots for each setting have similar results as shown in Fig.5.16.

B) Experiment results: SNR effects. We first, we fix the TX power difference, $P_\Delta = P^s - P^w = 7$dBm to control the SINR, and measure the corresponding averaged ESR over 200 sets under different TX power levels, to evaluate the residual error performance

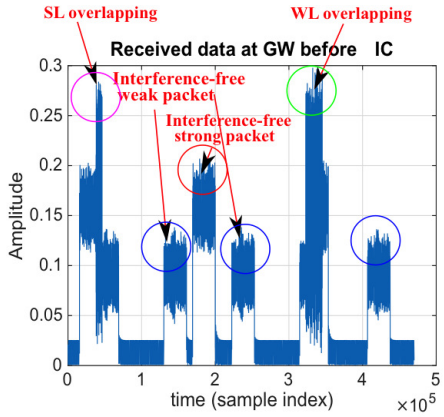

(a) Amplitude of received signal before IC

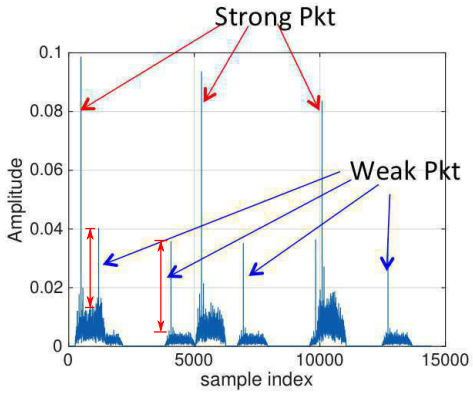

(b) Amplitude of SOP metric before IC

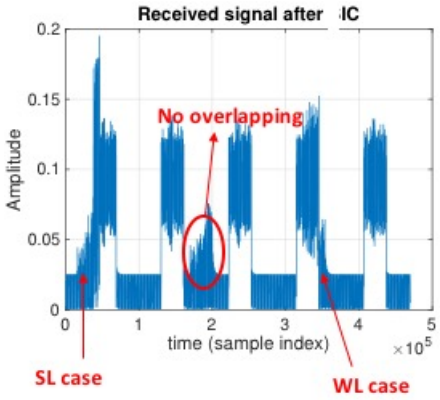

(c) Amplitude of received signal after IC

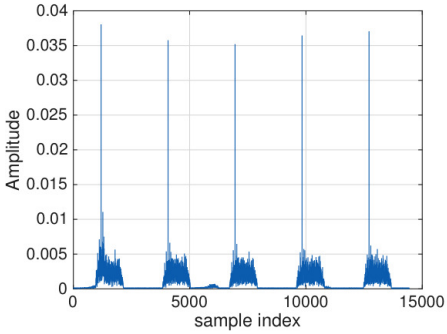

(d) Amplitude of SOP metric after IC

Figure 5.14: The received signal at GW for IC processing.

in terms of SNR.

High TX power: we first conduct the experiments at high power levels with $P^s = 0dBm$ and $P^w = -7dBm$. The corresponding residual error measurements are red curves shown in Fig.5.17 with measured SNR and SINR of the strong packet to be $18.96dB, 6.50dB$, respectively. We observe that when the overlapping degree grows, the corresponding averaged ESR decreases for the SL case (red curve with star symbols), while it increases for the WL case (red curve with circle symbols). Intuitively, this happens because the instantaneous error is increasing but the ESR is averaged only over the overlapping period. Thus, in the SL case, for small O, only the highest instantaneous error is captured in the average. On the other hand, in the WL case, for small O, only the lowest instantaneous errors are

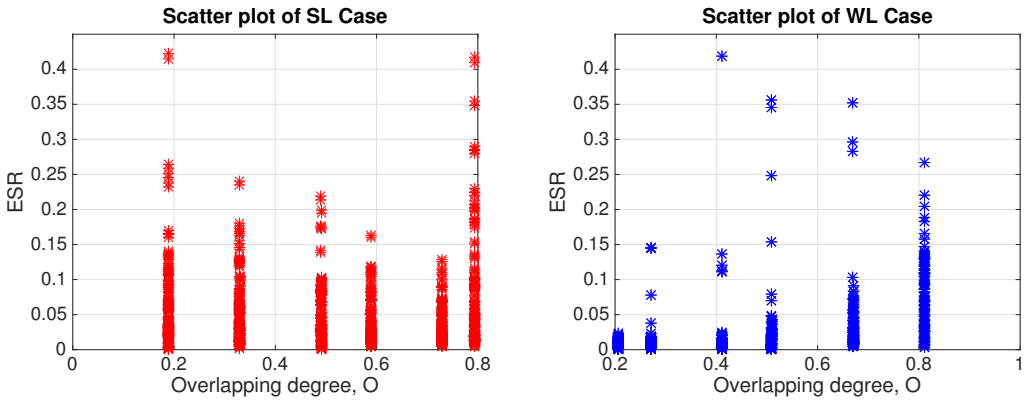

(a) SL case (b) WL case

Figure 5.15: Scatter plot of measured ESR with $SNR = 18.96dB, SINR = 6.50dB$.

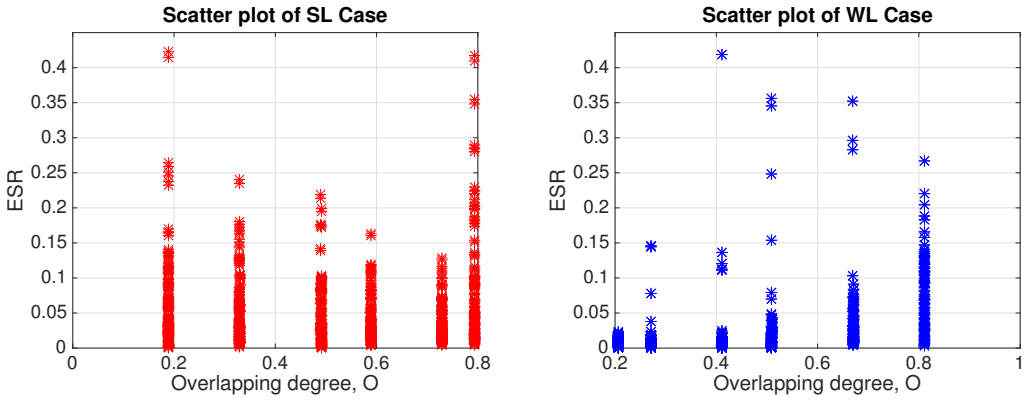

(a) SL case (b) WL case

Figure 5.16: Scatter plot of measured ESR with $SNR = 18.96dB, SINR = 6.50dB$.

captured in the average. As O grows for the SL (WL) case, smaller (larger) values of the instantaneous error are averaged in, causing the downward (upward) trends in the graph. We also observe that SL ESR goes up dramatically when $O = 0.8$. This happens because the preamble accounts for a quarter of the total packet. So when $O > 0.75$, the preamble of the strong packet for the SL case is also interfered so that synchronization and channel estimation performance are sacrificed.

Low TX power: to demonstrate the effect of the SNR, we conduct experiments at the lower TX power levels of $P^s = -7dBm$ and $P^w = -14dBm$. The corresponding residual error measurements are blue curves shown in Fig.5.17 with measured SNR and SINR of

the strong packet to be $11.98dB, 5.65dB$, respectively. We observe that when the SNR of the strong packet reduces, the corresponding ESR increases by comparing with the the blue curve with star symbols and red curve with star symbols for the SL case, while it does not change much for WL case by comparing blue and red curves with circle symbols. This happens because the synchronization and channel estimation performances are mainly affected by the SNR for the SL case as there is no interference on the preamble, and the ESR grows as the synchronization performance gets worse with lower SNR. However for the WL case, the synchronization and channel estimation performances are mainly affected by the SINR.

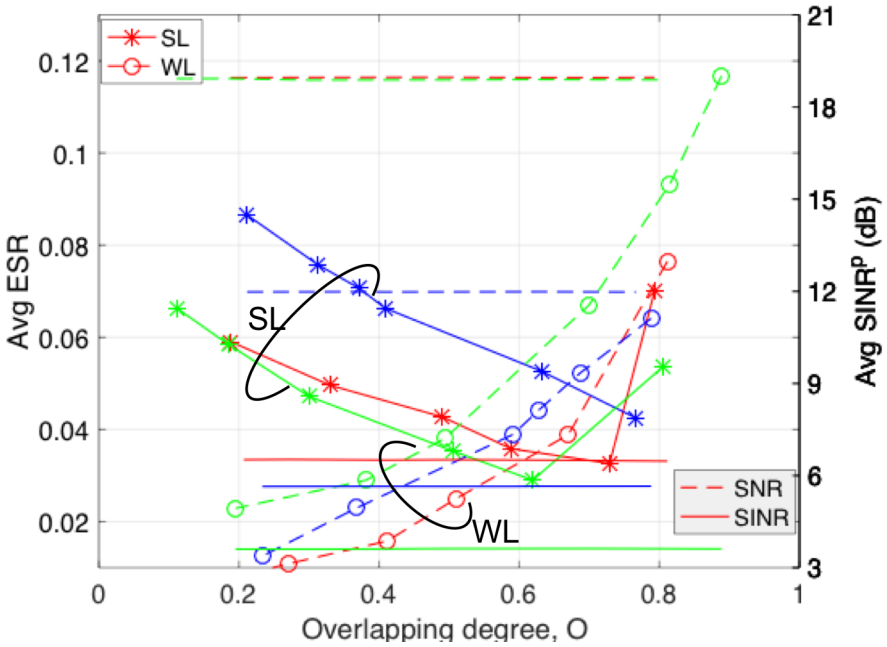

Figure 5.17: Measured average ESR.

C) Experiment results: SINR effects. In this subsection, we evaluate the effect of SINR by reducing the TX power difference from 7dBm to 4dBm. The TX powers are $P^s = 0dBm$ and $P^w = -4dBm$. The corresponding residual error measurements are green curves shown in Fig.5.17 with measured SNR and SINR of the strong packet to be $18.89dB$, $3.62dB$, respectively. By comparing the green curves and red curves, we observe that the ESR is similar to the SL case with star symbols, while it is worse for the WL case with

circle symbols. This happens because when the SNR does not change much, the synchronization and channel estimation performances are similar for SL without interference on the preamble, but sacrificed for the WL case with interference on the preamble as SINR decreases.

5.5 Summary

We propose an on-demand network MIMO scheme to support TO-sensors for LPWA sensing applications. It's an approach that combines the "capture and SIC" (C&S) and"network MIMO" (NMIMO) through the coordination among gateways.

In addition, we establish a complete data-aided (DA) synchronization algorithm for minimum-shift keying (MSK) transmission. To guarantee the efficiency of packet detection even under a packet overlapping scenario, our frame synchronization metric is based on a pseudo-random (PN) sequence preamble and keeps a constant low false alarm by dynamic thresholding based on real-time error floor level. Carrier frequency offset algorithm is proposed by taking advantage of the reliability of discrete fourier transform (DFT). Meanwhile, the preamble is also used as the training sequence for phase offset estimation based on a least-square (LS) estimator to reduce the transmit energy. We simulate the packet detection rate, false alarm rate and along with the root mean square (RMS) error of all synchronization parameters for the scenarios with and without packet overlapping.

Lastly, we evaluate the practical residual error for continuous phase modulation through analysis and experiments on SDRs. The instantaneous residual error is demonstrated to have a sinusoidal pattern over time caused by the synchronization error. The relationship between the practical residual error and the SNR, SINR of the strong packet being cancelled have been verified through both theoretical analysis and experiments in reality. It is demonstrated that, the practical residual error factor, g grows with respect to the overlapping degree, O but with an increased slope when there is interference on preamble, such as WL case, while it grows with the growth of O but with a decreased slope when the preamble

is clean, such as SL case. The slope modeled as the residual-error-to-signal-ratio (ESR), is shown through theory and experiments to have an oppsite dependence on O, and has corresponding dependence on SNR and SINR of the cancelled packet, respectively. Thus the conventional residual error model, which assumes the residual error is independent of the level and location of the interference, is proved to be unrealistic in pratice.

The corresponding contributions are: 1) an on-demand network MIMO scheme to achieve dynamic packet decoding from transmit-only sensors; 2) a data-aided (DA) synchronization algorithm for minimum-shift keying (MSK) transmission which is interference insensitive; 3) a method of the practical residual error of interference cancellation (IC) for MSK packets, considering realistic synchronization. The model is verified through the measurement on the SDR testbed.

CHAPTER 6
HYBRID METHOD OF SELECTIVE NONLINEAR PRECODING AND INTERFERENCE ALIGNMENT

6.1 Overview

Interference alignment (IA) is a well known technique to boost the system capacity over MIMO interfering broadcast channels (IBCs) by effectively aligning interferences into spatial dimensions, which are almost orthognal to the dimension occupied by the desired signals. However, the conventional IA algorithms with iterations suffer from large convergence time.

THP performs better than IA but requires stronger coordination on the TX side in terms of waveform generation and strict synchronization among local oscillators. Therefore, we explore the idea of performing THP only on selected links within a collection of links already using IA. The coordinated waveform generation can be achieved through cloud computing at a central unit, which is a promising technique for cloud radio access network (C-RAN).

In this work, we propose a hybrid nonlinear precoding and interference alignment scheme, aiming to improve the PHY layer performance among multiple MIMO IBCs. The novelties include: 1) We modify the conventional MMSE IA algorithm by minimizing the interference among selected paths but ignore the interference among the other paths, leading to faster convergence; 2) We apply the THP on top of selected IA beams with the purpose of handling the residual interference of imperfect IA; 3) we repeat the modified IA with random initializations in order to maximize the sum capacity and reduce the BER performance difference among users. Sum capacity appears to converge with number of repetitions.

6.1.1 System model

We are interested in the effective joint interference cancellation for the downlink transmission from multiple co-channel access points (APs) to the user equipments (UEs) in a dense multi-user MIMO network as illustrated in Fig.6.1. The APs and UEs are equipped with M_{AP}, M_{UE} antennas, respectively.

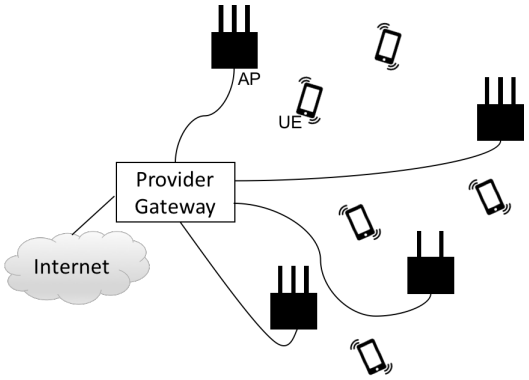

Figure 6.1: System model of multi-user MIMO network.

To support the simultaneous transmission of K MIMO links, the popular MMSE IA algorithm [50] can be considered. The MMSE IA is formulated as an optimization problem with the objective of minimizing the sum minimum mean squared error (MMSE) as:

$$\underbrace{\min}_{\{\mathbf{f_k^{IA}}\},\{\mathbf{g_k^{IA}}\}} \sum_{k=1}^{K} \epsilon_k = \sum_{k=1}^{K} E\{|s_k - \hat{s}_k|^2\} \; s.t. \; |\mathbf{f_k^{IA}}|^2 = 1, \tag{6.1}$$

where, s_k and $\hat{s}_k$ are the transmitting and receiving source signals of the kth link, while $\mathbf{f_k^{IA}}$ and $\mathbf{g_k^{IA}}$ are the corresponding precoders and decoders (i.e., transmit and receive beamformers) to be optimized.

With the transmitting signal power normalized to be one, $E\{|s_k|^2\} = 1$, the mean

squared error (MSE) for the kth link can be written as:

$$\begin{aligned}\epsilon_k &= E\{|s_k - \hat{s}_k|^2\} \\ &= |\mathbf{g_k^{IA}}^H \mathbf{H_{kk}} \mathbf{f_k^{IA}} - 1|^2 + \underbrace{\sum_{i=1, i\neq k}^{K} |\mathbf{g_k^{IA}}^H \mathbf{H_{ki}} \mathbf{f_i^{IA}}|^2}_{\text{interference}} + |\mathbf{g_k^{IA}}|^2 \sigma_\mathbf{n}^2.\end{aligned} \tag{6.2}$$

where, $\mathbf{H_{ji}}$ represents the MIMO channel between UE$_j$ and AP$_i$ with Rayleigh flat fading; σ_n^2 is the averaged power of the additive white Gaussian noise (AWGN).

Given the global channel state information (CSI) and random initialization of the precoders, the precoders and decoders are computed iteratively as [50]:

$$\mathbf{g^{IA,i}} = \left(\sum_{\mathbf{j=1}}^{\mathbf{K}} \mathbf{H_{kj}} \mathbf{f_j^{IA,i-1}} (\mathbf{f_j^{IA,i-1}})^\mathbf{H} (\mathbf{H_{kj}})^\mathbf{H} + \sigma_\mathbf{n}^\mathbf{2} \mathbf{I} \right)^{-\mathbf{1}} \mathbf{H_{kk}} \mathbf{f_k^{IA,i-1}}, \tag{6.3}$$

$$\mathbf{f^{IA,i}} = \left(\sum_{\mathbf{j=1}}^{\mathbf{K}} \mathbf{H_{jk}^H} \mathbf{g_j^{IA,i}} (\mathbf{g_j^{IA,i}})^\mathbf{H} \mathbf{H_{jk}} + \lambda^\mathbf{2} \mathbf{I} \right)^{-\mathbf{1}} \mathbf{H_{kk}^H} \mathbf{g_k^{IA,i}}, \tag{6.4}$$

where i is the iteration index; $\lambda_k \leq 0$ is the Lagrange multiplier to control $|\mathbf{f_k^{IA,i}}|^2 = 1$.

The convergence condition over the precoders is measured by the threshold variable, T, as:

$$|\mathbf{f_k^{IA,i}} - \mathbf{f_k^{IA,i-1}}| \leq T, k = 1, ..., K. \tag{6.5}$$

In the literature, it is reported in [52] that IA optimization is a non-convex and NP-hard problem. Thus, most current research efforts have been focused on finding a high quality suboptimal solution with the cost of high computational complexity. Therefore, in the next section, we propose a novel method of selective application of nonlinear preocoding of THP on top of IA beams for more efficient interference cancellation.

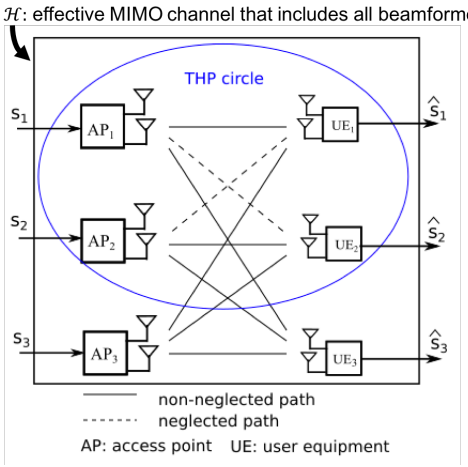

Figure 6.2: Illustration of the system model for the hybrid method among 3 2×2 MIMO IBCs.

6.2 Proposed Hybrid Method

The goal of our hybrid method is to improve the overall physical layer performance in terms of the BER and computational complexity by selectively applying NLP on top of IA beams. We arbitrarily select the first O user pairs for THP processing; by definition these pairs are contained in the THP circle, and the corresponding UEs are defined as hybrid users. As illustrated in Fig.6.2, we first select $O = 2$ AP-UE pairs out from the total $K = 3$ pairs for THP processing. On the other hand, the $O + 1, ..., K$ user pairs outside the THP circle will be IA-only user pairs. In addition, we will neglect the inter-UE interference within the THP circle, while the other interference will be aligned.

The proposed hybrid method has physical layer block diagrams shown in Fig.6.3, with $O = 2, K = 3$. The parts inside the dashed squares are related to the THP processing. As we can see, the NLP of THP is applied only on selected user pairs, and only require co-operation on transmitter side but yield independent processing on the UE side. The entire algorithm is realized in two steps: 1) generate IA beams; 2) perform nonlinear precoding layered on selected IA beams. The details of each step are shown in the following subsections.

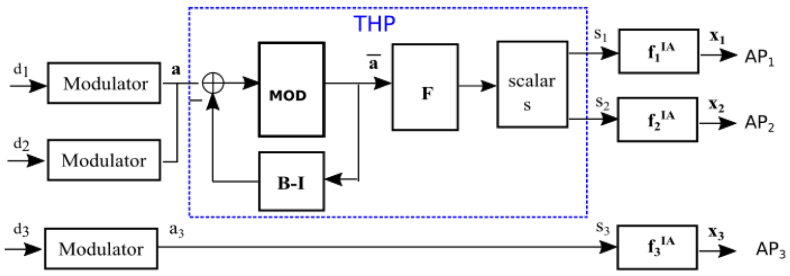

(a) TX PHY structure

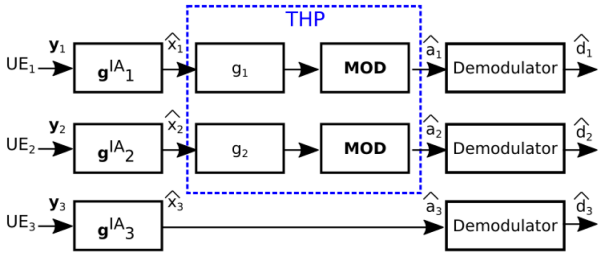

(b) RX PHY structure

Figure 6.3: Block diagrams of hybrid nonlinear precoding and IA method over 3 AP-UE pairs.

6.2.1 Step 1: Modified IA

According to the TX and RX structures as shown in Fig.6.3, the MSE of hybrid users within the THP circle, $k = 1, ..., O$, can be written as:

$$\epsilon_k = E\{|s_k - \hat{s}_k|^2\} \tag{6.6}$$
$$= |(\mathbf{g_k^{IA}})^{\mathbf{H}}\mathbf{H_{kk}}\mathbf{f_k^{IA}} - \mathbf{1}|^{\mathbf{2}} + \underbrace{\sum_{i=1, i\neq k}^{O} |(\mathbf{g_k^{IA}})^{\mathbf{H}}\mathbf{H_{ki}}\mathbf{f_i^{IA}}|^{\mathbf{2}}}_{\text{interference from within THP circle}} + \underbrace{\sum_{i=O+1}^{K} |(\mathbf{g_k^{IA}})^{\mathbf{H}}\mathbf{H_{ki}}\mathbf{f_i^{IA}}|^{\mathbf{2}}}_{\text{interference from outside THP circle}} + |\mathbf{g_k^{IA}}|^{\mathbf{2}}\sigma_{\mathbf{n}}^{\mathbf{2}},$$

which consists of two kinds of interference. On the other hand, the MSE for the IA only users outside the THP circle, where $k = O+1, ..., K$, are same as the conventional MMSE IA expressed by Eq.(6.2).

The task during this step is determining the precoders and decoders to generate the IA beams with low cost. To achieve this, we focus on canceling the interference only to and

from nodes outside the THP circle by setting the CSI over the neglected paths to be empty during the IA processing. In other words, we ignore the interference that is received within the THP circle that also originated from within the THP circle, or the first sum in Eq.(6.6). The modified MSEs of the kth link, $\bar{\epsilon}_k$, among the hybrid users becomes:

$$\begin{cases} \bar{\epsilon}_k = |\mathbf{g_k^{IA^H}} \mathbf{H_{kk}} \mathbf{f_k^{IA}} - \mathbf{1}|^2 + \underbrace{\sum_{i=O+1}^{K} |\mathbf{g_k^{IA^H}} \mathbf{H_{ki}} \mathbf{f_i^{IA}}|^2}_{\text{interference outside from THP circle}} + |\mathbf{g_k^{IA}}|^2 \sigma_\mathbf{n}^2, \quad \text{for } k = 1, ..., O \\ \bar{\epsilon}_k = \epsilon_k, \quad \text{for } k = O+1, ..., K \end{cases}, \tag{6.7}$$

Instead of minimizing the sum MSE conventionally as Eq.(6.1), we optimize the precoders and decoders by minimizing cost function of Eq (6.7), or

$$\underbrace{\min}_{\{\mathbf{f_k^{IA}}\},\{\mathbf{g_k^{IA}}\}} \sum_{k=1}^{K} \bar{\epsilon}_k \;\; s.t. \; |\mathbf{f_k^{IA}}|^2 \leq 1, k = 1, ..., K. \tag{6.8}$$

By solving $g_k^{IA} = \frac{\partial \epsilon_k | f_i^{IA}}{\partial g_k^{IA}} = 0$, and $f_k^{IA} = \frac{\partial \epsilon_k | g_i^{IA}}{\partial f_k^{IA}} = 0$, the precoders $\mathbf{f_k^{IA}}$,and decoder, $\mathbf{g_k^{IA}}$ for hybrid users, $k = 1, ..., O$, are derived as:

$$\begin{aligned} \mathbf{g_k^{IA,i}} = & \Bigg(\sum_{\mathbf{j=O+1}}^{\mathbf{K}} \mathbf{H_{kj}} \mathbf{f_j^{IA,i-1}} (\mathbf{f_j^{IA,i-1}})^\mathbf{H} (\mathbf{H_{kj}})^\mathbf{H} + \\ & \mathbf{H_{kk}} \mathbf{f_k^{IA,i-1}} (\mathbf{f_k^{IA,i-1}})^\mathbf{H} (\mathbf{H_{kk}})^\mathbf{H} + \sigma_\mathbf{n}^2 \mathbf{I} \Bigg)^{-\mathbf{1}} \mathbf{H_{kk}} \mathbf{f_k^{IA,i-1}}, \end{aligned} \tag{6.9}$$

$$\begin{aligned} \mathbf{f_k^{IA,i}} = & \Bigg(\sum_{\mathbf{j=O+1}}^{\mathbf{K}} \mathbf{H_{jk}} \mathbf{g_j^{IA,i}} (\mathbf{g^{IA,i}})^\mathbf{H} \mathbf{H_{jk}} + \\ & \mathbf{H_{kk}} \mathbf{g_k^{IA,i}} (\mathbf{g_k^{IA,i}})^\mathbf{H} \mathbf{H_{kk}} + \lambda_\mathbf{k} \mathbf{I} \Bigg)^{-\mathbf{1}} \mathbf{H_{kk}^H} \mathbf{g_k^{IA,i}}. \end{aligned} \tag{6.10}$$

Meanwhile, the precoders and decoders for the IA-only user pairs, $k = O+1, ..., K$, are same as conventional MMSE IA with closed forms as Eqs.(6.3) and (6.4). Since we don't care about some of the paths of interference, effectively having fewer constraints (the

constraints are only hard for zero forcing, which MMSE becomes if Gaussian noise goes to zero), we expect lower MSE for users outside the THP circle.

Since we don't care about some of the paths of interference, effectively having fewer constraints (the constraints are only hard for zero forcing, which MMSE becomes if the Gaussian noise goes to zero), we expect lower MSE for users outside the THP circle.

With the precoders and decoders determined, the received signal at the jth UE after IA decoding then becomes

$$\hat{s}_j = (\mathbf{g_j^{IA}})^{\mathbf{H}} \sum_{\mathbf{i=1}}^{\mathbf{K}} \mathbf{H_{ij}} \mathbf{f_i^{IA}} s_i. \tag{6.11}$$

We then can model the link between TXs and RXs using the combined effective channel $\mathcal{H}$, which is a compound K by K matrix that relates s_i to $\hat{s}_i$ as shown in Fig.6.2. The equivalent SISO link for delivering the source signal s_k between the jth UE and the ith AP, $\hbar_{ji}$, can be defined as:

$$\hbar_{ji} = (\mathbf{g_j^{IA}})^{\mathbf{H}} \mathbf{H_{ji}} \mathbf{f_i^{IA}}. \tag{6.12}$$

For the purpose of easy expression, we divide the combined channel $\mathcal{H}$, into three parts as illustrated in Fig.6.4. The $\mathcal{H}^1$ represents the effective channel within the THP circle.

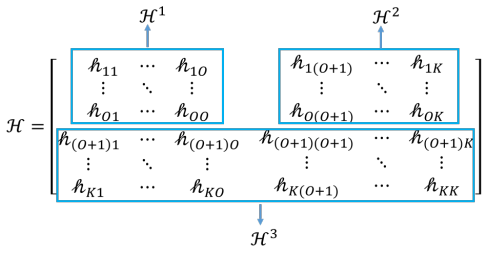

Figure 6.4: Illustration of the effective channel decomposition.

With perfect, zero forcing IA, $\mathcal{H}$ would be a diagonal matrix with 1s on the diagonal and 0s on the off-diagnals, indicating zero inter-UE interference. However the iterative-type IA algorithm is imperfect and the MSE cost function allows some interference. As shown

in Fig.6.5(a), the average $\mathcal{H}$ over 1000 channel trials, with averaged number of iterations of 46.8, has residual interference indicated by the non-zeros on the off-diagonals. On the other hand, the proposed modified IA under the same convergent threshold achieves the effective channel as shown in Fig6.5(b) with only averaged number of iterations of 8.9, while reducing the interference among all non-neglected paths dramatically as indicated by the $0s$ on the last column and the last row. We also observe the amplified interference within the THP circle in the sub-channel, $\mathcal{H}^1$, which we plan to handle in next step through nonlinear precoding.

```
0.9858    0.0026    0.0032
0.0032    0.9862    0.0029
0.0028    0.0026    0.9873
```

(a) Conventional IA

```
0.9979    3.8194    0.0000
4.0485    0.9981    0.0000
0.0000    0.0000    0.9993
```

(b) Modified IA

Figure 6.5: Averaged magnitude of channel gain of the effective compound channel $\mathcal{H}$, averaged over 1000 channel realizations at $Eb/No = 30dB$ with convergent threshold of $T = 10^{-4}$.

6.2.2 Step 2: Nonlinear precoding of THP

Given the effective channel, $\mathcal{H}$, we are able to apply the THP on top of IA beams with the equivalent system model as shown in Fig.6.2.

As shown in Fig.6.3, we apply the nonlinear precoding of THP on top of selected first $O = 2$ IA beams. The joint processing is only required at the TX side, while all the receivers are operating independently. The intermediate matrices for THP processing in Fig.6.3(a) are computed based on the sub-channel $\mathcal{H}^{\mathbf{1}}$ as [20]:

$$\text{LQ-factorization: } \mathcal{H}^{\mathbf{1}} = \mathbf{L}\mathbf{F}^H, \tag{6.13}$$

$$\mathbf{B} = \mathbf{G}\mathbf{L}, \text{with } b_{ij} = \frac{l_{ij}}{l_{ii}}; s.t, \mathbf{G} = diag\{l_{11}^{-1}, ..., l_{OO}^{-1}\}, \tag{6.14}$$

where $\mathbf{L}$ is a lower triangular matrix with l_{ij} as the element of ith row and jth colum, and $\mathbf{F}$ is a unitary matrix.

We consider M-QAM modulation with the constellation denoted as $\mathcal{A} = \{a_I + ja_Q | a_I, a_Q \in \{\pm 1, \mp 3, \ldots, \pm(\sqrt{M}-1)\}\}$, where the constellation is bounded by the square region of width $2\sqrt{M}$.

The block labeled as **MOD** is the nonlinear modulo operation defined as:

$$[p]\mathbf{mod}_L = p - \left\lfloor \frac{\Re(p) + L/2}{L} \right\rfloor L - j \left\lfloor \frac{\Im(p) + L/2}{L} \right\rfloor L, \tag{6.15}$$

where $L = 2\sqrt{M}$.

Because of the nonlinear processing of modulo, the averaged signal power, $E\{|\bar{\mathbf{a}}|^2\}$, is increased compared with $E\{|\mathbf{a}|^2\}$.

To control the averaged signal power of the IA beams, which is critical for the effectiveness of IA, a scalar block is added at the end of THP processing, where $s = \frac{E\{|\mathbf{a}|^2\}}{E\{|\bar{\mathbf{a}}|^2\}} \simeq \frac{M}{M-1}$.

The scalar used at the UE side is:

$$g_k = \frac{1}{sl_{kk}}. \tag{6.16}$$

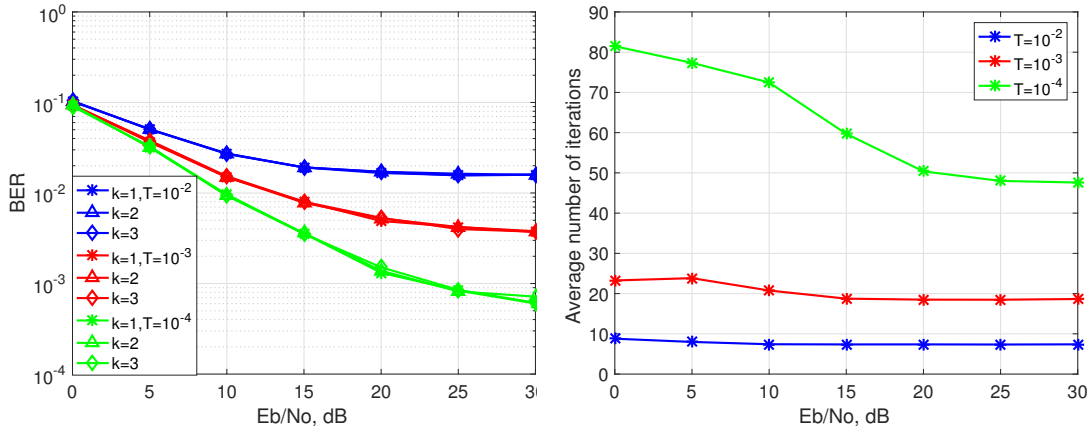

(a) Averaged BER (b) Average iteration numbers

Figure 6.6: Simulation of conventional MMSE IA over three 2×2 MIMO links under flat fading channel.

6.3 Simulation Study on BER Performance

6.3.1 IA Only

In this subsection, we present the simulations of the conventional MMSE IA case for three 2×2 MIMO links where the 6×6 MIMO matrix comprises iid complex Gaussian elements according to Rayleigh fading. The results are used as a primary reference for the proposed hybrid method. The BER performances under different convergence thresholds over 10,000 channel realizations are shown in Fig. 6.6. We observe that all users (indexed by k) have the same BER performance, which is improved with the lower convergence threshold, T, but with increased iterations. In addition, there is an error floor because of the residual interference from imperfect IA.

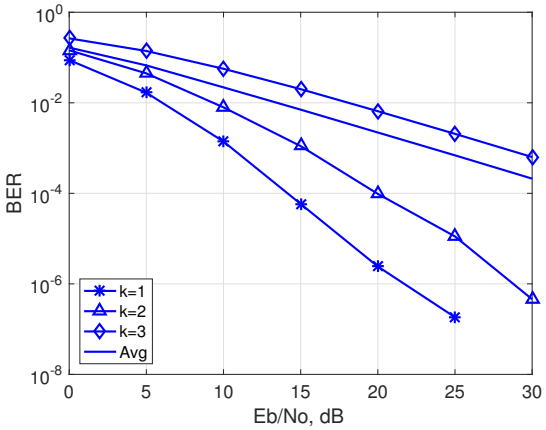

Figure 6.7: Simulation of multi-user THP over 3 SISO streams.

6.3.2 THP only

Most existing works present averaged BER over all streams. However, we desire to see how performance differs among links in order of THP processing. Therefore, we evaluate the pure THP performance per stream for reference in this subsection. The simulation is conducted over 3 source streams for the 3×3 MIMO matrix composed of i.i.d elements, same as Section 6.3.1, over 10,000 trials. According to the results in Fig. 6.7, we observe

the different diversity gains among streams. As we can tell, the earlier encoded streams with smaller k enjoy the lower BERs and higher diversity gains indicated by the steeper slopes of the BER curves. This happens because the LQ factorization during THP processing decomposes the kth row of the $K \times K$ channel metric into k orthogonal subspaces and the SNR of the received signal is determined only by its energy in just one subspace. Therefore, the signal with larger k will generally result in larger BER because its energy is distributed among more subspaces. In addition, the performance averaged over the streams is limited by the last stream ($K = 3$), as expected.

6.3.3 Hybrid method

The results for the hybrid method at different convergence thresholds where $O = 2, K = 3$ are shown in Figs. 6.8 and 6.9.

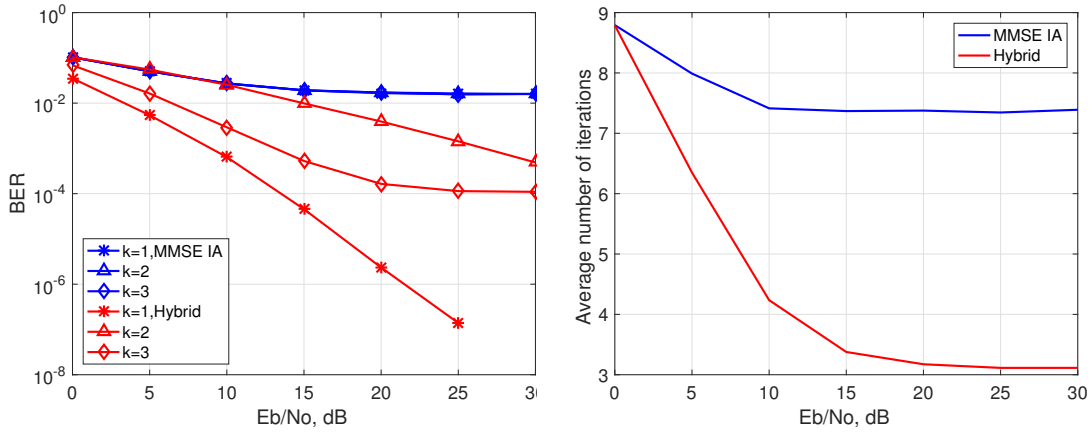

(a) BER (b) Iteration number

Figure 6.8: Simulation of hybrid method at threshold $T = 10^{-2}$.

According to the results in Fig.6.8, we observe that the hybrid scheme with modified IA has a lower BER compared with the conventional MMSE IA, especially for links $k = 1$ and $k = 3$. The error floor of the IA-only user, $k = 3$, is lower because of the additional degrees of freedom in the modified IA algorithm. Meanwhile, the interference among hybrid users, $k = 1, 2$, are pre-subtracted perfectly through NLP as evidenced by the lack of error floor.

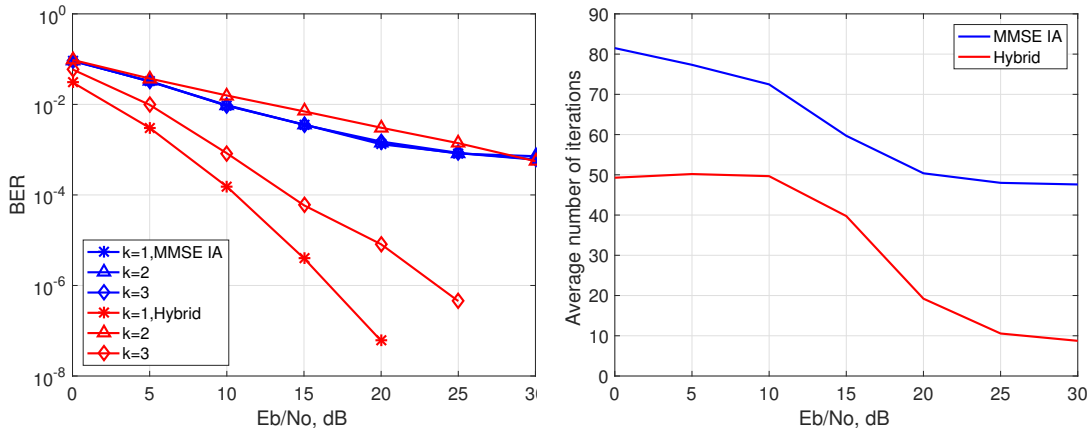

(a) BER (b) Iteration number

Figure 6.9: Simulation of hybrid method at threshold $T = 10^{-4}$.

We also observe that because of the diversity gain difference of THP, the $k = 2$ or last THP link BER diverges from the MMSE IA only because of the MMSE IA error floor at high SNR. In addition, the iteration number, which converges at high Eb/No is reduced significantly for the hybrid method.

According to the results in Fig.6.9, we observe that lowering the threshold T improves the BER, especially for the IA only user $k = 3$, but with the cost of more iterations. The worst performance for the hybrid method is still limited by the last hybrid user, $k = 2$.

6.4 Capacity Optimization

It is known in the literature that THP utilizes the entire capacity of the underlying MIMO channel [16]. The capacity of a MIMO channel, $\mathbf{H}$, when the average transmitter power is constrained to be ρ is given by [90] as $C = log_2 det(\mathbf{I} + \frac{\rho}{\sigma_n^2}\mathbf{H}\mathbf{H}^H)$, which becomes $C \approx log_2 det(\frac{\rho}{\sigma_n^2}\mathbf{H}\mathbf{H}^H)$ at high SNR. Exploiting this approximation, we propose to repeat the low-cost modified MMSE IA N times with random initializations and choose the optimal precoders and decoders with the maximal determinant factor, d, which is defined as:

$$d = det|\mathcal{H}^{\mathbf{1}}(\mathcal{H}^{\mathbf{1}})^H|. \tag{6.17}$$

The capacity for the hybrid method based on the received SNR for both IA-only users and hybrid users is derived in Appendix B, where the determinant factor, d, is shown to be the key factor for the capacity regarding the hybrid users.

Given the inputs of the global CSI, initialization of the global maximal determinant, $d_{opt} = 0$, and the repetition counter $n = 1$, the entire IA process is summarized as follows.

Modified MMSE IA

---

1) Randomly initialize the precoders, $\mathbf{f_k^{IA,0}}, k = 1, ..., K$ with normalized power of 1, such that $|\mathbf{f_k^{IA,0}}|^2 = 1$;

2) Optimize the decoders, $\{\mathbf{g_k^{IA,i}}\}$ with fixed precoders according to Eqs.(6.9) and (6.3);

3) Optimize the precoders, $\{\mathbf{f_k^{IA,i}}\}$ with fixed decoders according to Eqs.(6.10) and (6.4);

4) Repeat from 2) until $|\{\mathbf{f_k^{IA,i}}\} - \{\mathbf{f_k^{IA,i-1}}\}|^2 < T$, for $k = 1, ..., K$, to get the local optimal precoders and decoders.

5) Compute the corresponding determinant factor for the nth repeation, d_n based on the effective channel. If $d_n > d_{opt}$, update the optimal determinant factor, $d_{opt} = d_n$, and the global optimal precoders and decoders.

6) Increase the counter, $n = n + 1$. If $n = N$, exit; otherwise go to Step 1).

6.4.1 Simulation of variable repetitions, N

The BER results for the proposed hybrid method at different IA repetitions, N, with fixed convergence threshold are shown in Fig. 6.10. We observe that there is significant improvement on the worst link, $k = 2$, when we increase the repetitions of the modified IA, while the performance of the other two are guaranteed with small change. In addition, the improvements in performance for $k = 2$ decrease with the growth of N, which will converge eventually. The biggest single-step improvement happens at $N = 2$.

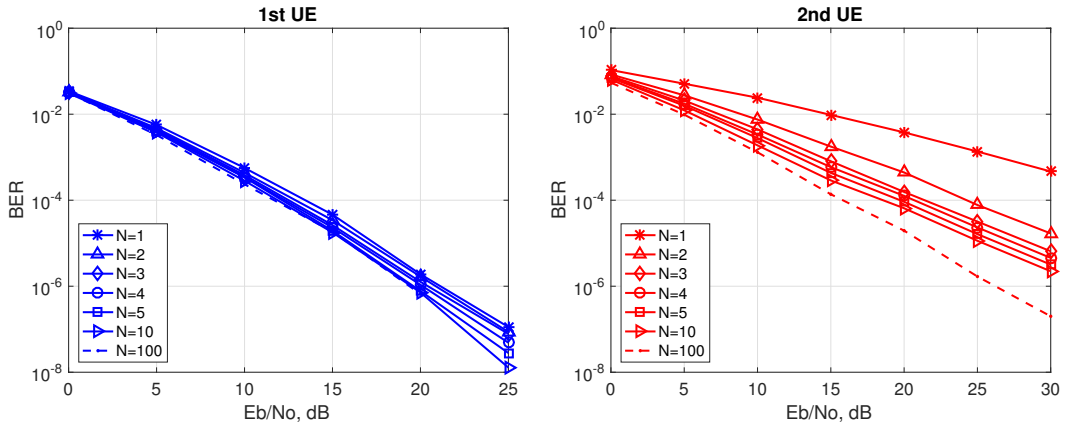

(a) $k = 1$

(b) $k = 2$

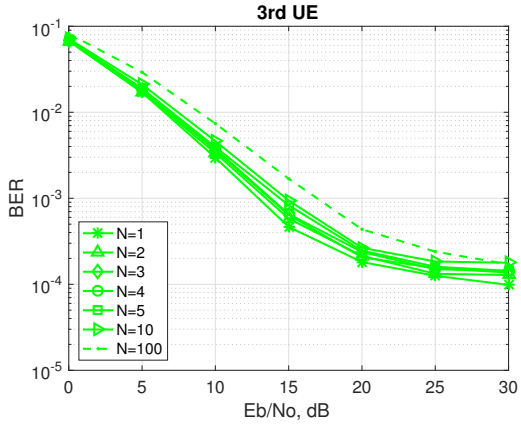

(c) $k = 2$

Figure 6.10: Simulation on the BER of the hybrid method over variable IA repeatitions, N at convergent threshold $T = 10^{-2}$.

The corresponding iterations results are shown in Fig.6.11. The number of iterations increases linearly with respect to N. For $N = 2$ with the biggest BER gain in Fig. 6.10, the number required iterations of about 6 is still very attractive compared with conventional MMSE IA.

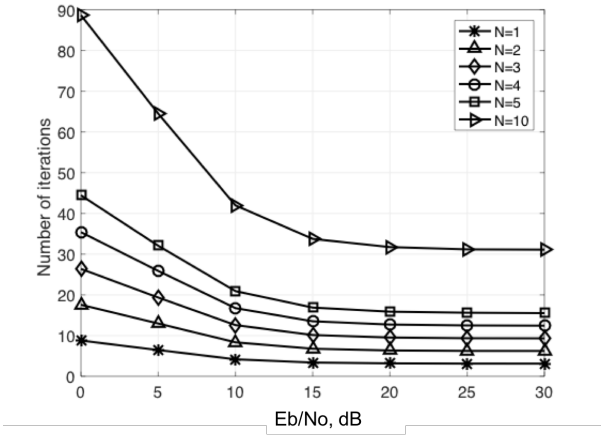

Figure 6.11: Simulation on the iteration numbers of the hybrid method over variable IA repeatitions, N at convergent threshold $T = 10^{-2}$.

6.5 Scalability

In this section, we evaluate the scalability of the proposed hybrid method for a larger network size. We repeat the simulation for five $3 * 3$ MIMO links, and select the first three links, $k = 1, 2, 3$, as hybrid users, while the other two, $k = 4, k = 5$, as IA only users. The simulation results averaged over 10,000 i.i.d channel realizations are shown in Fig. (6.12).

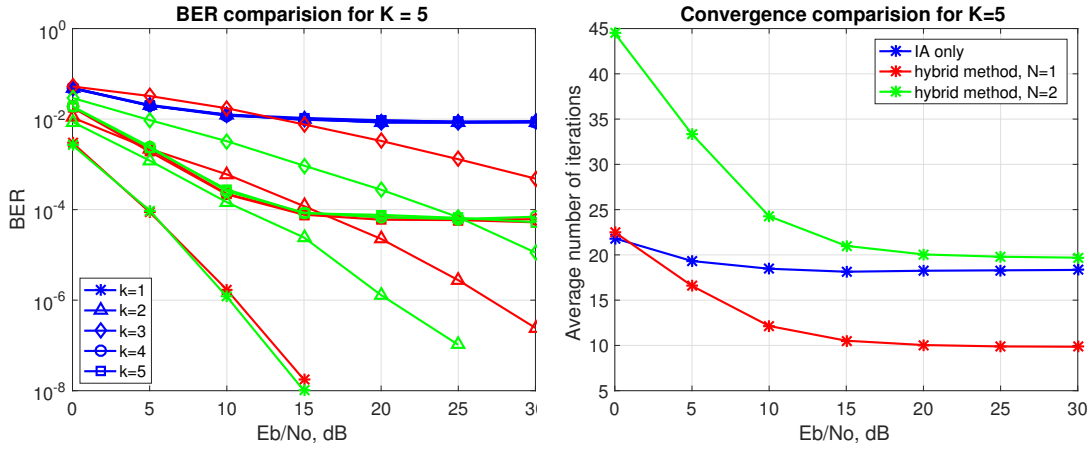

(a) BER (b) Iteration number

*(*Blue: MMSE IA; Red: hybrid method, N=1; Green: hybrid method, N=2)*

Figure 6.12: Simulation results for five $3 * 3$ MIMO links at convergence threshold $T = 10^{-2}$.

According to the simulation results shown in Fig$6.12(a)$, the BER performance for all

links are improved dramatically for the hybrid method compared with conventional IA. We see similar trends for hybrid method as for the smaller network size. For the hybrid users, $k \leq 3$, there are diversity gain differences; when we repeat the modified IA twice $N = 2$, the performance for the 2nd and 3rd users are improved significantly. For the IA-only users, the BER performances are the same, but error floors occur because of the high convergence threshold. However the error floor for the hybrid method is reduced by half compared with conventional IA. On the other hand, according to the result in Fig.6.12(b), the average number of iterations for conventional IA converges to 18.34 at high Eb/No, while it converges to 9.85 for hybrid method at $N = 1$, and 19.7 for $N = 2$. There is a tradeoff for the hybrid method between capacity and computational complexity.

6.6 Experimental Study

6.6.1 Linear and nonlinear precoding (LP & NLP)

As shown in Fig.6.13, we implement the LP and NLP for a single MIMO link. The MIMO terminal with 2 antennas is shown in Fig. 6.14. Because of the hardware limitation, we only focus on the realization of a 2*2 MIMO link. For the sake of easy and quick CSI feedback, we let our TX & RX radios connect to a central server through the internet. The central server runs a TCP/IP socket program to collect and forward real-time CSI between the RX and TX.

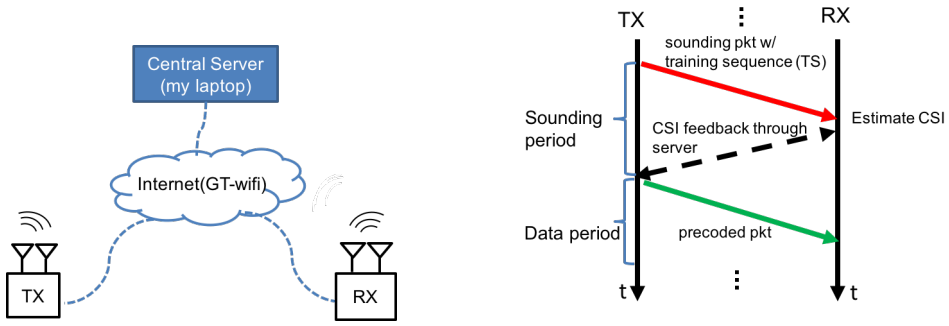

(a) Nodes setup (b) Timeline of transmission cycle

Figure 6.13: System model for the implementation of LP and NLP on SDR.

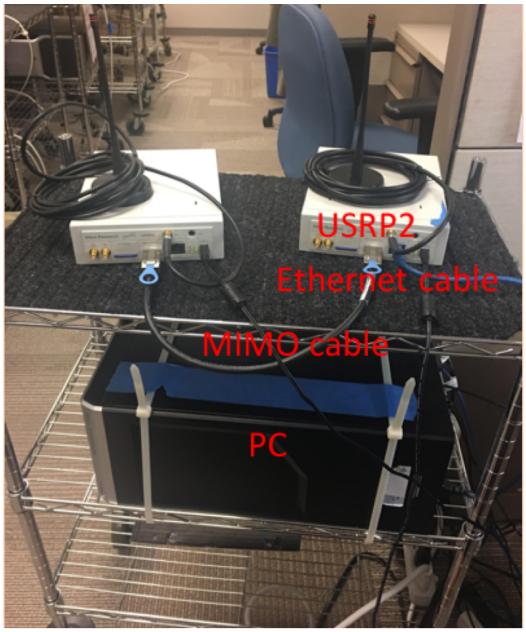

Figure 6.14: SDR of MIMO terminal (2 TX/RX antenna).

Fig.6.13(b) illustrates the timeline of a transmission cycle for every precoded packet. The complete transmission cycle consists of two periods: sounding period and data period. First, the TX sends a sounding packet with orthogonal TSs over the air. Then, once the RX detects the packet, the RX does least square estimation of the channel and feeds the estimates back to the TX through the server. With the CSI available at TX side, then the TX is able to start the data period by computing the precoder and sending the precoded data over the air.

Packet structure

(a) Sounding packet (b) Data packet

Figure 6.15: Packet structure for OFDM based LP/NLP.

The sounding packets and data packets are designed specifically as shown in Fig.6.15. We consider the wideband system with OFDM transmission. The two kinds of packets start with the same preamble, which consists of two OFDM symbols as proposed in refer-

ence [60]; the preamble is used for packet synchronization. Then, there is a physical layer header after the preamble. The header is one OFDM symbol long and it carries 5 bytes of information, containing information such as the MIMO scheme adopted, number of training sequences (TS). It is differentially encoded so that it can be decoded non-coherently without known CSI. After the header, there are some training sequences (TSs), which are PN sequences used for channel estimation. Each TS is one OFDM-length with pilot tones on all the subcarriers. For the sounding packet, the TSs are in orthogonal time slots across antenna streams. For the data packet, the TSs are overlapped to deal with practical synchronization error. Lastly, arbitrary number of OFDM symbols of payload can be added. We use BPSK modulation; there are 4 bytes of CRC bits at the end of the payload, which is used to check whether the packet is decoded successfully or not.

The system parameters used for the experiments on LP/NLP are shown in Table 6.1.

Table 6.1: System parameters for LP/NLP experiments

Signal bandwidth	1MHz
FFT length	128
Subcarrier spacing	7.8125KHz
CP length	8
OFDM symbol duration	136us
Packet duration	1ms

TX/RX structures.

The block diagrams of TX/RX for NLP and LP implemented on SDRs are illustrated in Figs. 6.16 and 6.17, respectively. We consider ZF with precoder, $\mathbf{P} = \mathbf{H^H}(\mathbf{H^H H})^{-1}$. To make sure that the TX signal does not saturate the power amplifier, we normalize the signal by the Frobenious norm, so the final precoder of ZF as shown in Fig.6.17(a) is $\mathbf{F} = \frac{\mathbf{P}}{|\mathbf{P}|_\mathbf{F}^2}$.

Effects of phase error. In practice, we perform synchronization at the RX, as there is residual CFO error on each packet. The CFO error difference between sounding packet and data packet will cause a phase error on the effective channel between the sounding packet, $\mathbf{H}_s$, and data packet, $\mathbf{H}_d$, which can be modeled as $\mathbf{H}_d = \mathbf{H}_s e^{j\theta}$.

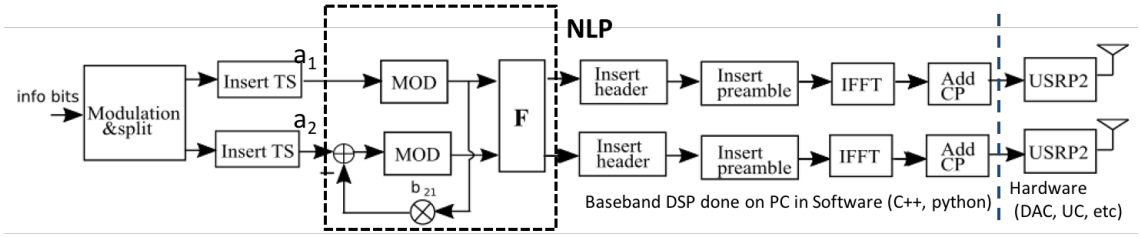

(a) TX structure

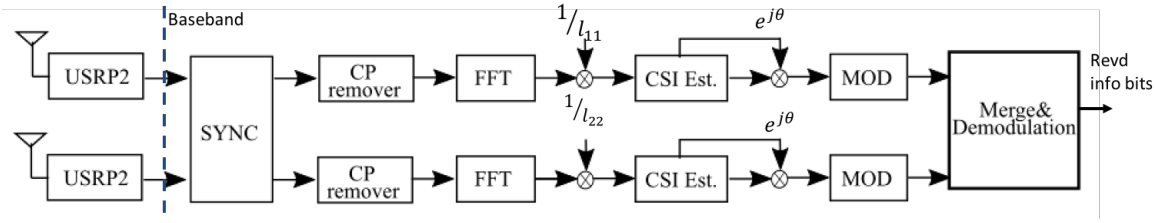

(b) RX structure

Figure 6.16: Block diagram of the implementaion of NLP on SDRs

The received signal in the frequency domain can be modeled as:

$$y_1 = e^{j\theta} l_{ii} x_1 = e^{j\theta} l_{11}(a_1 + k_1\sqrt{M}) \tag{6.18}$$

$$\begin{aligned} y_2 &= e^{j\theta} l_{21} x_1 + e^{j\theta} l_{22} x_2 \\ &= e^{j\theta} l_{21} x_1 + e^{j\theta} l_{22}(a_2 - \frac{l_{21}}{l_2 2} x_1 + k_2\sqrt{M}) \\ &= e^{j\theta} l_{22}(a_2 + k_2\sqrt{M}), \end{aligned} \tag{6.19}$$

where a_i is the modulated symbol for the source stream i, k_i is an integer because of the modulo operation, and M is the modulation index. l_{ii} is the diagonal element of the matrix $\mathbf{L}$ in the LQ factorization for THP.

Therefore, we estimate the phase error as conventional CSI estimation given the information about l_{ii} and k_i:

$$e^{j\hat{\theta}_1} = y_1/(l_{11} * (a_1 + k_1 2\sqrt{M}) \tag{6.20}$$

$$e^{j\hat{\theta}_2} = y_2/(l_{22} * (a_2 + k_1 2\sqrt{M})), \tag{6.21}$$

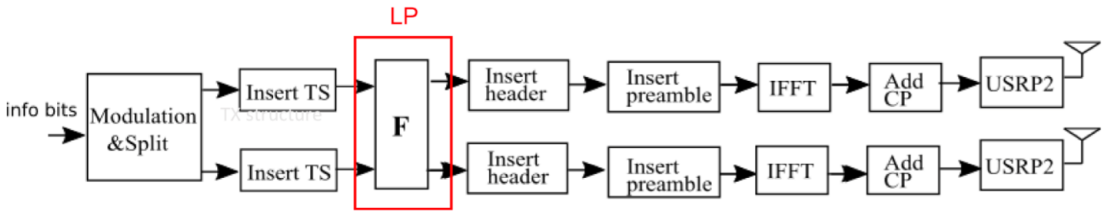

(a) TX structure

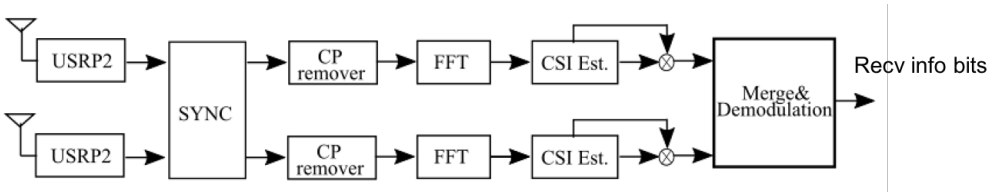

(b) RX structure

Figure 6.17: Block diagram of the implementaion of ZF LP on SDRs

To achieve selective diversity, we use the estimated result from the optimal link with larger $|l_{ii}|^2$ for the phase error compensation for both streams.

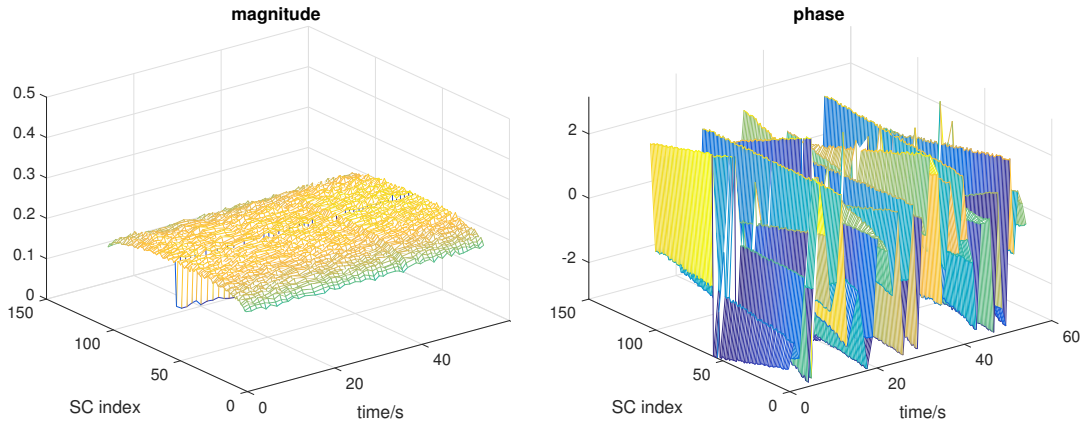

(a) Magnitude (b) Phase

Figure 6.18: Mean CSI for one path out from the 2*2 H at CF of 900MHz in the lab (1 sounding pkt/s)

Experimental results: CSI collection. As shown in Fig.6.18(a), we observe that the magnitude is constant over the time/frequency domain, which indicates a long and large coherence time/bandwidth. For the indoor environment, the coherence bandwidth is quite large and the channel is static for over 60s when there are no people moving around. How-

ever, we observe that the phase rotates continuously over the subcarriers and has random initial values across packets in the time domain. This happens because of the fractional time offset and the CFO estimation differences across packets.

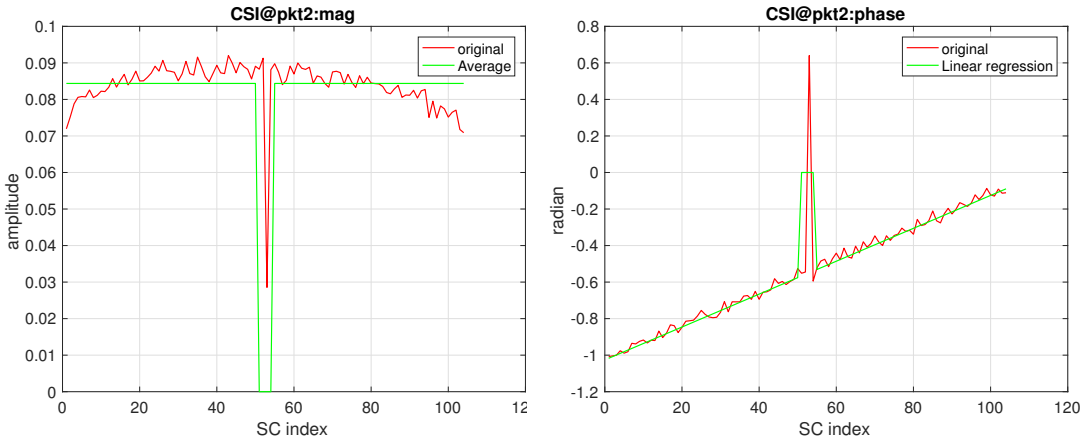

(a) Magnitude (b) Phase

Figure 6.19: Measured CSI for one link at fixed time for h_{11} out from $\mathbf{H}$ from 2nd sounding packet

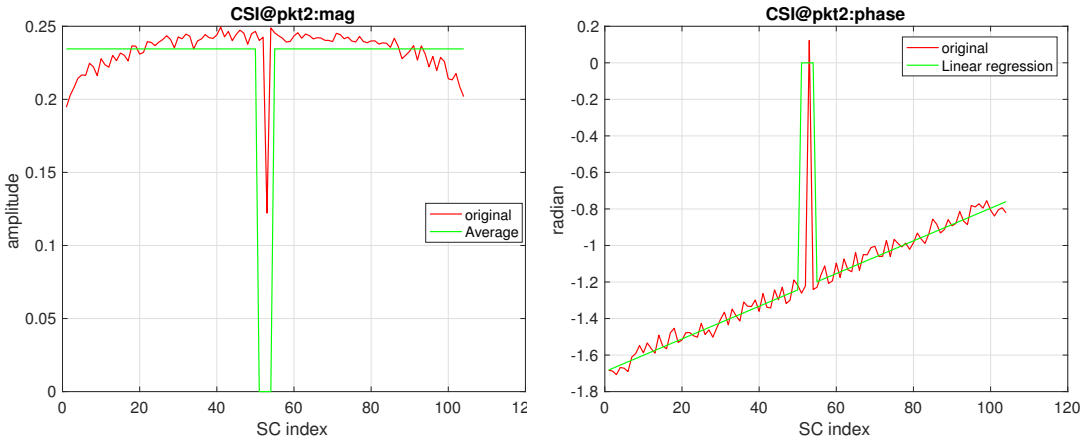

(a) Magnitude (b) Phase

Figure 6.20: Measured CSI for one link at fixed time for h_{21} out from $\mathbf{H}$ from 2nd sounding packet

According to Figs. 6.19 and 6.20, we observe that the slope for continuous phase rotation over frequency domain is same over the element of the channel matrix, $\mathbf{H}$, between a TX and RX node. The phase rotation over the frequency domain is caused by fractional time offset, which is determined by the local oscillator differences. Therefore, the channel

at different subcarrier i, and j, can also be modeled as:

$$\mathbf{H_i} = \mathbf{H_j} e^{j\theta}. \tag{6.22}$$

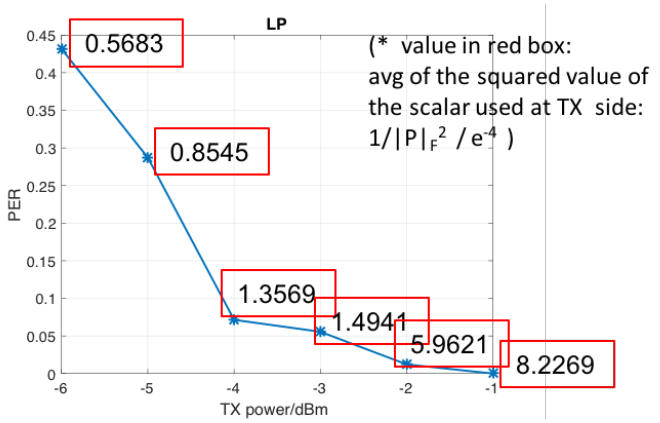

(a) LP

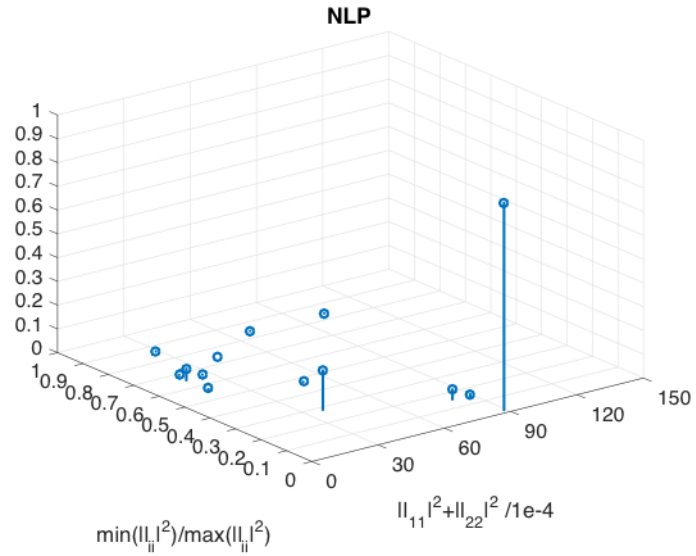

(b) NLP

Figure 6.21: Averaged PER over 100 packets (transmission gap of 1s)

Experimental results: PER measurements. We conduct experiment in our lab where transmitter and receiver blocked by the cubicle wall with non-line-of-sight link. For the LP in Fig.6.21(a), we change TX power with fixed TX/RX locations, and compute the PER averaged over ~ 100 packets in $\sim 100s$. As shown in Fig.6.21(a), we observe that the PER

of LP decreases with the growth of TX power. Because the received SNR is proportional to $\frac{1}{|P|_F^2}$, and are same over data streams.

For the NLP, the PER is measured as a average over ~ 100 packets in $\sim 100s$. We conduct experiments over variable TX power in the range from $-10dBmto-2dBm$ and variable locations. We found the PER is not directly determined by the TX power, therefore we display the results in 3D plot as shown in Fig.6.21(b). We observe, the PER of NLP decreases with the growth of $\sum |l_{ii}|^2$, and the ratio of min and max of $|l_{ii}|^2$. This happens because the SNR of the received signal of NLP is proportional to $|l_{ii}|^2$, and has different diversity over the spatial source streams, and the PER is limited by the worst source stream.

6.7 Summary

A hybrid method of selective application of NLP on top of IA beams over multi-user, multi-access point MIMO networks has been proposed for the purpose of more efficient interference cancellation. We first determine the IA precoders and decoders by ignoring the selected interference paths, which results in fast convergence and better interference cancellation among the other paths. Then, we apply NLP on top of the beams with interference to pre-subtract the ignored interference. It is shown through simulations that the proposed method achieves better BER performance with fewer IA iterations compared with the conventional MMSE IA scheme. In addition, the BER performance can be improved further by repeating the modified IA with random initializations to maximize the system capacity. In addition, the BER peformance can be improved further by repeating the modifed IA with random initialization to maximize the system capacity.

The corresponding contributions are: 1) a hybrid method combing nonlinear precoding (NLP) and interference alignment (IA), which selectively applies NLP on top of IA beams to achieve lower computation complexity and better BER performance compared with the IA-only scheme. 2) demonstrate the NLP in a realistic indoor environment.

CHAPTER 7

CONCLUSIONS AND SUGGESTED FUTURE WORKS

Distributed arrays (DAs) are a collection of distinct radios or devices that collaborate in the physical layer or waveform domain in terms of synchronization and modulation. The distributed spatial gains can be used to enhance reliability and date rate, similarly as classic arrays. The advantages of DAs over classic arrays are network flexibility and lower per device hardware cost. However, the cost is network overhead to organize and provide various levels of synchronization.

In this dissertation, we focus on developing distributed array approaches for a variety of wireless networks. To be specific, we target OFDM-based wideband transmission in ad-hoc networks and wireless LAN, and MSK-based narrowband transmission for low power wide area (LPWA) applications in sensor networks.

One major contribution of this dissertation is developing novel synchronization algorithms for DAs. The first one is an OFDM-based method, that enables, to the best of our knowledge, for the first time, synchronization with diversity gain for the time-division cooperative transmission (TDCT). Therefore, it supports range extension without requiring more energy on the preamble. In addition, a novel data-aided synchronization algorithm is proposed for MSK-based narrowband transmission. That algirithm is interference insensitive so it can support transmit-only sensors for LPWA applications.

The dissertation also addresses decoding schemes for DAs. First, an on-demand network MIMO scheme is proposed to achieve MIMO decoding in the cloud for only selected packets for the uplink in a one-hop multi-gateway sensor networks. Second, a hybrid method combining nonlinear precoding (NLP) and interference alignment (IA) is established to boost the system capacity over MIMO interfering broadcast channels (IBCs). By selectively applying NLP on top of IA beams, the hybrid method achieves lower computa-

tion complexity and better BER performance compared with the IA-only scheme.

Moreover, we perform an analysis of the practical residual error of interference cancellation (IC) for MSK packets, considering realistic synchronization. The distribution, the mean, and the variance of the IC residual error factor are derived. These statistics are shown to depend strongly on the packet overlap degree and the signal to interference and noise ratio (SINR) of the preamble of the packet being canceled, which contrasts with the popular constant model of residual error factor. The proposed practical residual error model is verified through the measurement on the software-defined radio (SDR) testbed.

Lastly, another contribution is the testbed. As TDCT and AF relaying are not supported by any existing standard or off-the-shelf radios, most existing works focus on theoretical capacity analysis. In this dissertation, we design the packet and nodes structure of TDCT and AF relaying. We demonstrate the packet error rate (PER) performance for TDCT, MU-MIMO with AF, and nonlinear precoding in a realistic indoor environment with a commercial software radio platform, using OFDM. In addition, a central server based on socket programing is built to collect the channel state information (CSI) from SDRs wirelessly.

The following is a list of possible directions for future research.

1. The statistical IC interference model can be used for network analysis of ALOHA and transmit only packet networks. With a specified network setup, such as a transmission pattern and path loss model, the statistics of the proposed residual error model can be used to evaluate the system level performance. In addition, the proposed residual error model can also be explored to guide the system design, such as, packet structure (e.g. duration and placement of preamble), in order to maximize the network throughput.

2. In this dissertation, we focus on the interference cancellation over MIMO IBCs within a cluster. One possible future work is to use THP to deal the inter-cluster interference cancellation for the edges users between IA clusters.

3. With the SDR testbed implemented in our lab, the global channel state information

(CSI) over multiuser MIMO interfering broadcast channel (IBC) can be measured and collected in a central server through the telemetry network. One possible future direction is to collect large amount of global CSI in different wireless environments, and evaluate the performance gain loss of any TX side beamforming scheme in terms of CSI aging. Moreover, as the size of global CSI grows with respect to the network size, effective CSI compression or interpretation schemes can be considered in the future to reduce the network traffic and the latency of CSI feedback.

Appendices

APPENDIX A

EXPERIMENTAL EQUIPMENT

For our implementation, a wireless node consists of USRP2 [91], and GNU Radio [92] running on a personal computer (PC). The USRP2 has ADC/DAC and FPGA to digitize the analog waveform and create the baseband sampled data stream, which is sent to the PC through a gigabit ethernet cable. The PC does all the baseband signal processing based on the flowgraph we designed. All the blocks in the flowgraph are implemented in C++ and integrated with Python scripts.

Single-antenna SDR: Each single-antenna SDR adopted in this thesis is built by connecting the USRP2 with a PC through the Ethernet cable.

1) *USRP2* works as the RF front-end of a SDR. It sends the digitalized samples to the PC through Gigabit Ethernet interface. USRP2 comes with only motherboard of FPGA. And we assemble it with the daughter board of WBX for up-conversion-conversion, analog to digital conversion (ADC), and digital to analog conversion (ADC). WBX supports carrier frequencies of 50MHz to 2.2GHz, variable analog bandwidth (200kHz-40MHz), and TX Power up to 20dBM;

2) *PC with Linux OS (Ubuntu)* has the software toolkit (GNU Radio) installed, which serves as the integrated development environment (IDE) for baseband signal processing using C++/Python.

MIMO transceiver: We connect multiple USRP2s to a single PC in order to build a MIMO terminal. In additions to the equipments listed for single-antenna SDR, the following hardwares are also needed.

1) *MIMO Cable* can be used to build a SDR of two antennas/USRPs. It provide the sharing of the ethernet connection to the single PC. Meanwhile, it syncs the local oscillator of one USRP2 board to the other.

2) *Reference Clock Distributor (RCD)* is designed and implemented by one former member of our lab to deal with the local oscillator discrepancies among different devices. It provides sync signals of 10MHz for frequency reference and 1PPS for timing reference, so that it could support a MIMO transceiver with up to 4 antennas.

3) *Gigabit Ethernet Switch* is used to connect multiple USRPs within the same subnetwork.

Telemetry system: We established a WiFi-based telemetry system that enables one person to configure experiments and visualize the real-time performance of the SDR network from virtually anywhere that has an Internet connection. The telemetry system is built based on socket programing using Matlab and Python.

APPENDIX B

CAPACITY DERIVATION OF HYBRID METHOD OF IA AND NLP

The total network sum capacity can be divided into two parts as expressed in Eq. (B.1): hybrid users, C^{hybrid}, which refer the selected users with both THP and modified IA processing; and the IA only users, $C^{\text{IA only}}$, which only perform the modified IA scheme.

$$\begin{aligned} C &= C^{\text{hybrid}} + C^{\text{IA only}} \\ &= \sum_{k=1}^{O} C_k + \sum_{k=O+1}^{K} C_k, \end{aligned} \tag{B.1}$$

where, C_k is the capacity of kth user.

We then analyze the capacity for hybrid users and IA only users separately in the following subsections.

Hybrid Users. In this subsection, we derive the capacity for those links ($k = 1, ..., O$) that adopt both THP and IA schemes.

According to the transmitter and receiver structures as illustrated in Fig.6.3, the source signal at kth AP within THP circle after **MOD** block becomes:

$$\bar{a}_k = [a_k - \sum_{i=1}^{k-1} b_{ki}\bar{a}_i] \text{ MOD}_L. \tag{B.2}$$

The final input signals for IA processing are:

$$\hat{\mathbf{a}} = \mathbf{F}\bar{\mathbf{a}}, \tag{B.3}$$

$$\bar{\mathbf{x}} = s\hat{\mathbf{a}} = s\mathbf{F}\bar{\mathbf{a}}, \tag{B.4}$$

Given the combined effective channel $\mathcal{H}$, the received IA beams within the THP

circle are:

$$\begin{aligned}\bar{\mathbf{y}} &= \mathcal{H}^{\mathbf{1}}\bar{\mathbf{x}} + \mathcal{H}^{\mathbf{2}}\bar{\mathbf{x}} + \bar{\mathbf{n}} \\ &= s\mathcal{H}^{\mathbf{1}}\mathbf{F}\bar{\mathbf{a}} + \mathcal{H}^{\mathbf{2}}\bar{\mathbf{x}} + \bar{\mathbf{n}} \\ &= s\mathbf{L}\mathbf{F}^{\mathbf{H}}\mathbf{F}\bar{\mathbf{a}} + \mathcal{H}^{\mathbf{2}}\bar{\mathbf{x}} + \bar{\mathbf{n}} \\ &= s\mathbf{L}\bar{\mathbf{a}} + \mathcal{H}^{\mathbf{2}}\bar{\mathbf{x}} + \bar{\mathbf{n}}\end{aligned} \tag{B.5}$$

$$\begin{aligned}\text{s.t, } \bar{y}_k = &\sum_{i=1}^{k} l_{ki}\bar{a}_i + \sum_{i=O+1}^{K} \hbar_{ki}\bar{x}_i + \bar{n}_k \\ = &\underbrace{s l_{kk}\bar{a}_k}_{\text{ideal data}} + \underbrace{s\sum_{i=1}^{k-1} l_{ki}\bar{a}_i}_{\text{Interference within THP circle}} \\ + &\underbrace{\sum_{i=O+1}^{K} \hbar_{ki}\bar{x}_i}_{\text{interference outside THP circle}} + \bar{n}_k,\end{aligned} \tag{B.6}$$

where $\bar{n}_k = (\mathbf{g_k^{IA}})^{\mathbf{H}}\mathbf{n_k}$ with averaged power of $\sigma_{\bar{n}}^2 = E|\mathbf{g}_k^{IA}|^2\sigma_n^2$, as σ_n^2 is the average power of the AWGN, $\mathbf{n_k}$.

Because of the pre-subtraction indicated by Eq (B.2), the received kth hybrid IA beam can be further derived as:

$$\bar{y}_k = s l_{kk}([a_k - \sum_{i=1}^{k-1} b_{ki}\bar{a}_i]\ \mathbf{MOD}_L) + s\sum_{i=1}^{k-1} l_{ki}\bar{a}_i + \sum_{i=O+1}^{K} \hbar_{ki}\bar{x}_i + \bar{n}_k. \tag{B.7}$$

By substituting $b_{ij} = \frac{l_{ij}}{ii}$, Eq.(B.7) becomes

$$\begin{aligned}\bar{y}_k &= s l_{kk}[a_k - \sum_{i=1}^{k-1} \frac{l_{ki}}{l_{kk}}\bar{a}_i]\mathbf{MOD}_L + s\sum_{i=1}^{k-1} l_{ki}\bar{a}_i + \sum_{i=O+1}^{K} \hbar_{ki}\bar{x}_i + \bar{n}_k \\ &= s l_{kk}[a_k]\mathbf{MOD}_L + \sum_{i=O+1}^{K} \hbar_{ki}\bar{x}_i + \bar{n}_k.\end{aligned} \tag{B.8}$$

By multiplying $g_k = \frac{1}{sl_{kk}}$, we then get

$$\hat{y}_k = g_k \bar{y}_k = [a_k]\mathbf{MOD}_L + g_k(\sum_{i=O+1}^{K} \hbar_{ki} a_i + \bar{n}_k). \tag{B.9}$$

As we can see, the received hybrid IA beam consists of only the ideal souce and interference outside the THP circle and the noise. The received SINR of the hybrid IA beam is:

$$\begin{aligned} \text{SINR}_k^{\text{hybrid}} =& \frac{\sigma_a^2}{|g_k|^2(\sigma_a^2 \sum_{i=O+1}^{K} |\hbar_{ki}|^2 + \sigma_{\bar{n}}^2)}, \\ =& \frac{s^2 l_{kk}^2}{(\sum_{i=O+1}^{K} |\hbar_{ki}|^2 + 1/\gamma)}, \end{aligned} \tag{B.10}$$

where, $\sigma_a^2 = E\{|a_k|^2\}$ is the averaged signal power of the modulated symbols, and $\gamma = \frac{\sigma_a^2}{\sigma_{\bar{n}}^2}$ is the equivalent TX side SNR.

The capacity for the THP circle are:

$$C^{\text{hybrid}} = \sum_{k=1}^{O} \log_2(1 + \text{SINR}_k^{\text{hybrid}}) \tag{B.11}$$

$$\simeq \sum_{k=1}^{O} \log_2(\text{SINR}_k^{\text{hybrid}}) \tag{B.12}$$

$$= \sum_{k=1}^{O} \log_2(\frac{s^2 l_{kk}^2}{\sum_{i=O+1}^{K} |\hbar_{ki}|^2 + 1/\gamma}) \tag{B.13}$$

$$\simeq \sum_{k=1}^{O} \log_2(\gamma s^2 l_{kk}^2) \tag{B.14}$$

$$= \log_2(\prod_{k=1}^{O} s^2 l_{kk}^2 \gamma) \tag{B.15}$$

$$= O\log_2(s^2\gamma) + \log_2(\prod_{k=1}^{O} l_{kk}^2). \tag{B.16}$$

Since $\mathcal{H}^{\mathbf{1}}(\mathcal{H}^{\mathbf{1}})^H = \mathbf{L}\mathbf{F}^{\mathbf{H}}\mathbf{F}\mathbf{L}^{\mathbf{H}} = \mathbf{L}\mathbf{L}^{\mathbf{H}}$, and L is lower triangular matrix, we see that $\prod_{k=1}^{O} l_{kk}^2$ is just the determinant, $|\mathcal{H}^{\mathbf{1}}(\mathcal{H}^{\mathbf{1}})^H| = |\mathbf{L}\mathbf{L}^{\mathbf{H}}|$.

Therefore, the capacity among the link within THP circle is bounded by the determinant related to the combined sub-channel $\mathcal{H}^1$ as:

$$C^{\text{hybrid}} = O\log_2(s^2 R\gamma) + \log_2(|\mathcal{H}^{\mathbf{1}}(\mathcal{H}^{\mathbf{1}})^H|). \tag{B.17}$$

According to Eq.(B.17), the capacity of hybrid users is limited by the transmitter side SNR and the determinant reference related to the combined channel after IA. Therefore, maximizing the determinant reference, $|\mathcal{H}^{\mathbf{1}}(\mathcal{H}^{\mathbf{1}})^H|$, during the IA processing helps maximizing the capacity within the THP circle.

IA only Users. In this subsection we evaluate the capacity for those users only adopt the modified IA algorithm.

For $k = O+1, ..., K$, the intput signal for IA only beam at the AP outside the THP circle is simply the modulated symbol $\bar{x}_k = a_k$ as shown in Fig.6.3. The received IA only beam is

$$\bar{y}_k = \hbar_{kk}\bar{x}_k + \sum_{i=1, i\neq k}^{K} \hbar_{ki}\bar{x}_i + \bar{n}_k, k = O+1, ..., K. \tag{B.18}$$

where, $\bar{n}_k = \mathbf{g}_k^{IA}\mathbf{n}$ is the equivalent noise with averaged power of $\sigma_{\bar{n}}^2$.

Therefore, the SINR becomes:

$$\text{SINR}_k^{\text{IA}} = \frac{|\hbar_{kk}|^2\sigma_a^2}{\sum_{i=1, i\neq k}^{K}|\hbar_{ki}|^2\sigma_a^2 + \sigma_{\bar{n}}^2} \tag{B.19}$$

The capacity of the IA only beams are:

$$C^{\text{IA}} = \sum_{k=O+1}^{K} \log_2(1 + \text{SINR}_k^{IA}) \tag{B.20}$$

$$\simeq \sum_{k=O+1}^{K} \log_2(\text{SINR}_k^{IA}) \tag{B.21}$$

$$= \sum_{k=O+1}^{K} \log_2\left(\frac{|\hbar_{kk}|^2\sigma_a^2}{\sum_{i=1,i\neq k}^{K}|\hbar_{ki}|^2\sigma_a^2+\sigma_{\bar{n}}^2}\right) \tag{B.22}$$

$$\simeq \sum_{k=O+1}^{K} \log_2\left(\frac{|\hbar_{kk}|^2\sigma_a^2}{\sigma_{\bar{n}}^2}\right) \tag{B.23}$$

$$= (K-O)\log_2(\bar{\gamma}) \tag{B.24}$$

where, $\bar{\gamma} = \frac{E\{|\hbar_{kk}|^2\}\sigma_a^2}{\sigma_{\bar{n}}^2}$ is the equivalent received SNR.

According to the Eq. (B.24), the capacity of IA only users is limited by the receiver side SNR with perfect interference alignment. The proposed method by ignoring the interference among insignificant paths improves the interference cancellation performance among the significant paths, thus helps reaching the maximal capacity.

REFERENCES

[1] H. Lipfert, "MIMO OFDM space time coding–spatial multiplexing, increasing performance and spectral efficiency in wireless systems, part i technical basis (technical report)," *Institut für Rundfunktechnik*, 2007.

[2] R. Van Nee, V. Jones, G. Awater, A. Van Zelst, J. Gardner, and G. Steele, "The 802.11 n MIMO-OFDM standard for wireless LAN and beyond," *Wireless Personal Communications*, vol. 37, no. 3-4, pp. 445–453, 2006.

[3] A. Lozano and N. Jindal, "Transmit diversity vs. spatial multiplexing in modern MIMO systems," *Wireless Communications, IEEE Transactions on*, vol. 9, no. 1, pp. 186–197, 2010.

[4] C. So-In, R. Jain, and A.-K. Tamimi, "Scheduling in IEEE 802.16 e mobile WiMAX networks: key issues and a survey," *IEEE Journal on selected areas in communications*, vol. 27, no. 2, pp. 156–171, 2009.

[5] G. Caire and S. Shamai, "On the achievable throughput of a multiantenna gaussian broadcast channel," *IEEE Transactions on Information Theory*, vol. 49, no. 7, pp. 1691–1706, 2003.

[6] K. B. Letaief and Y. J. Zhang, "Dynamic multiuser resource allocation and adaptation for wireless systems," *IEEE Wireless Communications*, vol. 13, no. 4, pp. 38–47, 2006.

[7] T. Usländer, "The trend towards the internet of things: what does it help in disaster and risk management?" *Planet@ Risk*, vol. 3, no. 1, 2015.

[8] P. MIKULECKY, "Intelligent environments approaches applied in water management," *op Pro ernatio ent En*, p. 27, 2015.

[9] "Internet of Things: the complete reimaginative force," TCS Global Trend Study, TATA Consultancy Services, 2015.

[10] S. M. Alamouti, "A simple transmit diversity technique for wireless communications," *IEEE Journal on selected areas in communications*, vol. 16, no. 8, pp. 1451–1458, 1998.

[11] D. N. C. Tse, P. Viswanath, and L. Zheng, "Diversity-multiplexing tradeoff in multiple-access channels," *IEEE Transactions on Information Theory*, vol. 50, no. 9, pp. 1859–1874, 2004.

[12] A. J. Paulraj, D. Gore, R. U. Nabar, H. Bölcskei, *et al.*, "An overview of MIMO communications-a key to gigabit wireless," *Proceedings of the IEEE*, vol. 92, no. 2, pp. 198–218, 2004.

[13] Y. Jiang, M. K. Varanasi, and J. Li, "Performance analysis of ZF and MMSE equalizers for MIMO systems: an in-depth study of the high SNR regime," *IEEE Transactions on Information Theory*, vol. 57, no. 4, pp. 2008–2026, 2011.

[14] Q. H. Spencer, A. L. Swindlehurst, and M. Haardt, "Zero-forcing methods for downlink spatial multiplexing in multiuser MIMO channels," *IEEE Transactions on Signal Processing*, vol. 52, no. 2, pp. 461–471, 2004.

[15] P. W. Wolniansky, G. J. Foschini, G. Golden, R Valenzuela, *et al.*, "V-BLAST: an architecture for realizing very high data rates over the rich-scattering wireless channel," in *Signals, Systems, and Electronics, 1998. ISSSE 98. 1998 URSI International Symposium on*, IEEE, 1998, pp. 295–300.

[16] C. Windpassinger, R. F. Fischer, T. Vencel, and J. B. Huber, "Precoding in multiantenna and multiuser communications," *IEEE Transactions on Wireless Communications*, vol. 3, no. 4, pp. 1305–1316, 2004.

[17] C. Masouros and E. Alsusa, "Dynamic linear precoding for the exploitation of known interference in mimo broadcast systems," *IEEE Transactions on Wireless Communications*, vol. 8, no. 3, pp. 1396–1404, 2009.

[18] C. Masouros and et al., "Computationally efficient vector perturbation precoding using thresholded optimization," *IEEE Transactions on Communications*, vol. 61, no. 5, pp. 1880–1890, 2013.

[19] C. Masouros, M. Sellathurai, and T. Ratnarajah, "Vector perturbation based on symbol scaling for limited feedback MISO downlinks," *IEEE Transactions on Signal Processing*, vol. 62, no. 3, pp. 562–571, 2014.

[20] R. F. Fischer, C. Windpassinger, A. Lampe, and J. B. Huber, "Space-time transmission using tomlinson-harashima precoding," *ITG FACHBERICHT*, pp. 139–148, 2002.

[21] A. Garcia-Rodriguez and C. Masouros, "Power-efficient tomlinson-harashima precoding for the downlink of multi-user MISO systems," *IEEE Transactions on Communications*, vol. 62, no. 6, pp. 1884–1896, 2014.

[22] C. Masouros, M. Sellathurai, and T. Ratnarajah, "Interference optimization for transmit power reduction in tomlinson-harashima precoded mimo downlinks," *IEEE Transactions on Signal Processing*, vol. 60, no. 5, pp. 2470–2481, 2012.

[23] R. F. Fischer, C. Stierstorfer, and C. Windpassinger, "Precoding and signal shaping for transmission over MIMO channels," in *Proc. 2003 Canadian Workshop on Information Theory*, 2003, pp. 83–87.

[24] V. Tarokh, H. Jafarkhani, and A. R. Calderbank, "Space-time block codes from orthogonal designs," *IEEE Transactions on Information theory*, vol. 45, no. 5, pp. 1456–1467, 1999.

[25] B. Lu and X. Wang, "Space-time code design in ofdm systems," in *Global Telecommunications Conference, 2000. GLOBECOM'00. IEEE*, IEEE, vol. 2, 2000, pp. 1000–1004.

[26] J. Lin, H. Jung, Y. J. Chang, J. W. Jung, and M. A. Weitnauer, "On cooperative transmission range extension in multi-hop wireless ad-hoc and sensor networks: a review," *Ad Hoc Networks*, vol. 29, pp. 117 –134, 2015.

[27] P. Murphy and A. Sabharwal, "Design, implementation, and characterization of a cooperative communications system," *IEEE Transactions on Vehicular Technology*, vol. 60, no. 6, pp. 2534–2544, 2011.

[28] J. N. Laneman, "Cooperative communications in mobile ad hoc networks," *IEEE Signal Processing Magazine*, vol. 1053, no. 5888/06, 2006.

[29] H. Jung and et al., "Experimental range extension of concurrent cooperative transmission in indoor environments at 2.4 ghz," in *Military Communications Conference*, IEEE, 2010, pp. 148–153.

[30] R. Mudumbai, D. R. B. Iii, U. Madhow, and H. V. Poor, "Distributed transmit beamforming: challenges and recent progress," *IEEE Communications Magazine*, vol. 47, no. 2, pp. 102–110, 2009.

[31] Y. J. Chang, "Design of concurrent cooperative transmission systems on software-defined radios," *PhD Dissertation, School of Electrical and Computer Engineering, Georgia Institute of Technology*, 2013.

[32] A. Bletsas, A. Khisti, D. P. Reed, and A. Lippman, "A simple cooperative diversity method based on network path selection," *Selected Areas in Communications, IEEE Journal on*, vol. 24, no. 3, pp. 659–672, 2006.

[33] C. Lim, T. Yoo, B. Clerckx, B. Lee, and B. Shim, "Recent trend of multiuser MIMO in LTE-advanced," *IEEE Communications Magazine*, vol. 51, no. 3, pp. 127–135, 2013.

[34] D. Lee, H. Seo, B. Clerckx, E. Hardouin, D. Mazzarese, S. Nagata, and K. Sayana, "Coordinated multipoint transmission and reception in lte-advanced: deployment scenarios and operational challenges," *IEEE Communications Magazine*, vol. 50, no. 2, pp. 148–155, 2012.

[35] K Chen and R Duan, "C-RAN–the road towards green RAN," *whitepaper of China Mobile Research Institute*, 2011.

[36] J. Liu, S. Zhou, J. Gong, Z. Niu, and S. Xu, "On the statistical multiplexing gain of virtual base station pools," in *Global Communications Conference (GLOBECOM), 2014 IEEE*, IEEE, 2014, pp. 2283–2288.

[37] I Chih-Lin, J. Huang, R. Duan, C. Cui, J. X. Jiang, and L. Li, "Recent progress on C-RAN centralization and cloudification," *Access, IEEE*, vol. 2, pp. 1030–1039, 2014.

[38] S.-H. Park, O. Simeone, O. Sahin, and S. Shamai, "Robust and efficient distributed compression for cloud radio access networks," *Vehicular Technology, IEEE Transactions on*, vol. 62, no. 2, pp. 692–703, 2013.

[39] L. Zhou and W. Yu, "Uplink multicell processing with limited backhaul via per-base-station successive interference cancellation," *Selected Areas in Communications, IEEE Journal on*, vol. 31, no. 10, pp. 1981–1993, 2013.

[40] M. Peng, C. Wang, V. Lau, and H. V. Poor, "Fronthaul-constrained cloud radio access networks: insights and challenges," *Wireless Communications, IEEE*, vol. 22, no. 2, pp. 152–160, 2015.

[41] M. K. Varanasi and B. Aazhang, "Multistage detection in asynchronous code-division multiple-access communications," *Communications, IEEE Transactions on*, vol. 38, no. 4, pp. 509–519, 1990.

[42] A. Duel-Hallen, "Decorrelating decision-feedback multiuser detector for synchronous code-division multiple-access channel," *Communications, IEEE Transactions on*, vol. 41, no. 2, pp. 285–290, 1993.

[43] P. Patel and J. Holtzman, "Analysis of a simple successive interference cancellation scheme in a DS/CDMA system," *Selected Areas in Communications, IEEE Journal on*, vol. 12, no. 5, pp. 796–807, 1994.

[44] J. G. Andrews, "Interference cancellation for cellular systems: a contemporary overview," *Wireless Communications, IEEE*, vol. 12, no. 2, pp. 19–29, 2005.

[45] C. Stefanovic, P. Popovski, and D. Vukobratovic, "Frameless aloha protocol for wireless networks," *IEEE Communications Letters*, vol. 16, no. 12, pp. 2087–2090, 2012.

[46] O. del Rio Herrero and R. De Gaudenzi, "Generalized analytical framework for the performance assessment of slotted random access protocols," *Wireless Communications, IEEE Transactions on*, vol. 13, no. 2, pp. 809–821, 2014.

[47] A. Zanella, A. Biral, and M. Zorzi, "Asymptotic throughput analysis of massive m2m access," in *Information Theory and Applications Workshop (ITA), 2015*, IEEE, 2015, pp. 64–69.

[48] J. G. Andrews and T. H. Meng, "Optimum power control for successive interference cancellation with imperfect channel estimation," *Wireless Communications, IEEE Transactions on*, vol. 2, no. 2, pp. 375–383, 2003.

[49] V. R. Cadambe and S. A. Jafar, "Interference alignment and degrees of freedom of the-user interference channel," *IEEE Transactions on Information Theory*, vol. 54, no. 8, pp. 3425–3441, 2008.

[50] D. A. Schmidt, C. Shi, R. A. Berry, M. L. Honig, and W. Utschick, "Minimum mean squared error interference alignment," in *2009 Conference Record of the Forty-Third Asilomar Conference on Signals, Systems and Computers*, IEEE, 2009, pp. 1106–1110.

[51] F. Negro, S. P. Shenoy, I. Ghauri, and D. T. Slock, "On the MIMO interference channel," in *Information Theory and Applications Workshop (ITA), 2010*, IEEE, 2010, pp. 1–9.

[52] Q. Shi, M. Razaviyayn, Z.-Q. Luo, and C. He, "An iteratively weighted mmse approach to distributed sum-utility maximization for a mimo interfering broadcast channel," *IEEE Transactions on Signal Processing*, vol. 59, no. 9, pp. 4331–4340, 2011.

[53] Z.-Q. Luo and S. Zhang, "Dynamic spectrum management: complexity and duality," *IEEE Journal of Selected Topics in Signal Processing*, vol. 2, no. 1, pp. 57–73, 2008.

[54] T. M. Schmidl and D. C. Cox, "Robust frequency and timing synchronization for OFDM," *Communications, IEEE Transactions on*, vol. 45, no. 12, pp. 1613–1621, 1997.

[55] B. Park and et al., "A novel timing estimation method for OFDM systems," *Communications Letters, IEEE*, vol. 7, no. 5, 2003.

[56] G. Ren, Y. Chang, H. Zhang, and H. Zhang, "Synchronization method based on a new constant envelop preamble for OFDM systems," *Broadcasting, IEEE Transactions on*, vol. 51, no. 1, pp. 139–143, 2005.

[57] H. Wang and et al., "A novel synchronization algorithm for OFDM systems with weighted CAZAC sequence," *J. Comput. Inf. Syst*, vol. 8, no. 6, pp. 2275–2283, 2012.

[58] J. Meng and G. Kang, "A novel OFDM synchronization algorithm based on CAZAC sequence," in *Computer Application and System Modeling, 2010 International Conference on*, IEEE, vol. 14, pp. V14–634.

[59] A. A. Nasir and et al., "Transceiver design for distributed STBC based AF cooperative networks in the presence of timing and frequency offsets," *Signal Processing, IEEE Transactions on*, vol. 61, no. 12, pp. 3143–3158, 2013.

[60] Y. J. Chang, Q. Lin, and M. A. Weitnauer, "Synchronization for multi-hop distributed MIMO-OFDM," ICC'15- Wireless Communications Symposium, IEEE International Conference on Communications, 2015.

[61] X. Xiong, K. Zheng, R. Xu, W. Xiang, and P. Chatzimisios, "Low power wide area machine-to-machine networks: key techniques and prototype," *Communications Magazine, IEEE*, vol. 53, no. 9, pp. 64–71, 2015.

[62] J. Gubbi, R. Buyya, S. Marusic, and M. Palaniswami, "Internet of things (IoT): a vision, architectural elements, and future directions," *Future Generation Computer Systems*, vol. 29, no. 7, pp. 1645–1660, 2013.

[63] *CC1101*, `http://www.ti.com/product/cc1101`.

[64] *ADF7023*, `http://www.analog.com/media/en/technical-documentation/data-sheets/{ADF}7023.pdf`.

[65] *NRF905*, `http://www.nordicsemi.com/eng/Products/Sub-1-GHz-RF/nRF905`.

[66] W. Gao, *Energy and Bandwidth-Efficient Wireless Transmission*. Springer, Cham, 2017.

[67] L. W. Couch, *Digital and Analog Communication Systems*. Prentice Hall, 2001.

[68] M. Morelli and G. M. Vitetta, "Feedforward joint phase and timing estimation for MSK type signals," *European transactions on telecommunications*, vol. 12, no. 4, pp. 327–336, 2001.

[69] U. Mengali, *Synchronization techniques for digital receivers*. Springer Science & Business Media, 2013.

[70] Q. Zhao and G. L. Stuber, "Robust time and phase synchronization for continuous phase modulation," *Communications, IEEE Transactions on*, vol. 54, no. 10, pp. 1857–1869, 2006.

[71] E. Hosseini and E. Perrins, "Timing, carrier, and frame synchronization of burst-mode CPM," *Communications, IEEE Transactions on*, vol. 61, no. 12, pp. 5125–5138, 2013.

[72] Y. J. Chang and M. A. Ingram, "Convergence property of transmit time pre-synchronization for concurrent cooperative communication," in *Global Telecommunications Conference, 2010 IEEE*, 2010.

[73] Z. Gao, Y. J. Chang, and M. A. Ingram, "Synchronization for cascaded distributed MIMO communications," in *Military Communications Conference*, IEEE, 2010, pp. 387–392.

[74] D. Chu, "Polyphase codes with good periodic correlation properties," *Information Theory, IEEE Transactions on*, vol. 18, no. 4, 1972.

[75] Y. S. Cho and et al., *MIMO-OFDM wireless communications with MATLAB*. John Wiley, 2010.

[76] Q. Lin, Y. J. Chang, F. Wang, and M. A. Weitnauer, "Implementation and analysis of multi-user mimo with amplify-and-forward relaying," in *Communications Workshops (ICC), 2014 IEEE International Conference on*, IEEE, 2014, pp. 32–37.

[77] J. N. Laneman and G. W. Wornell, "Energy-efficient antenna sharing and relaying for wireless networks," in *Wireless Communications and Networking Confernce, 2000. WCNC. 2000 IEEE*, IEEE, vol. 1, 2000, pp. 7–12.

[78] Y. J. Chang, M. A. Ingram, and R. S. Frazier, "Cluster transmission time synchronization for cooperative transmission using software-defined radio," in *Communications Workshops (ICC), 2010 IEEE International Conference on*, IEEE, 2010, pp. 1–5.

[79] F. Xiong, *Digital modulation techniques*. Artech House, 2006.

[80] D. Jakovetic, D. Bajovic, D. Vukobratovic, and V. Crnojevic, "Cooperative slotted ALOHA for multi-base station systems," *Communications, IEEE Transactions on*, vol. 63, no. 4, pp. 1443–1456, 2015.

[81] Z. Y. Choi and Y. H. Lee, "Frame synchronization in the presence of frequency offset," *Communications, IEEE Transactions on*, vol. 50, no. 7, pp. 1062–1065, 2002.

[82] E. Hosseini and E. Perrins, "The Cramer-Rao bound for training sequence design for burst-mode CPM," *Communications, IEEE Transactions on*, vol. 61, no. 6, pp. 2396–2407, 2013.

[83] L. S. Addison, *Statistical signal processing: detection, estimation and time series analysis*. Addison-Wesley, 1991.

[84] Q. Lin and M. A. Weitnauer, "Interference-insensitive synchronization scheme of MSK for transmit-only wireless sensor networks," in *ICC'16- Wireless Communications Symposium, IEEE International Conference on Communications*, 2016.

[85] A. Zanella and M. Zorzi, "Theoretical analysis of the capture probability in wireless systems with multiple packet reception capabilities," *Communications, IEEE Transactions on*, vol. 60, no. 4, pp. 1058–1071, 2012.

[86] A. Zygmund, *Trigonometric Series*. Cambridge University Press, 2002, vol. 1.

[87] A. Barbieri and G. Colavolpe, "On the Cramer-Rao bound for carrier frequency estimation in the presence of phase noise," *IEEE transactions on wireless communications*, vol. 6, no. 2, pp. 575–582, 2007.

[88] N. Noels, H. Steendam, M. Moeneclaey, and H. Bruneel, "Carrier phase and frequency estimation for pilot-symbol assisted transmission: bounds and algorithms," *IEEE Transactions on Signal Processing*, vol. 53, no. 12, pp. 4578–4587, 2005.

[89] F. B. Hildebrand, *Advanced calculus for applications*. Prentice-Hall Englewood Cliffs, NJ, 1962, vol. 63.

[90] G. J. Foschini, "Layered space-time architecture for wireless communication in a fading environment when using multi-element antennas," *Bell labs technical journal*, vol. 1, no. 2, pp. 41–59, 1996.

[91] *USRP2*, `http://gnuradio.org/redmine/projects/gnuradio/wiki/USRP2`.

[92] *GNU radio*, `http://gnuradio.org/`.